

Universidad de Santiago de Compostela
Facultad de Física
Departamento de Física de Partículas



**NEW ADVANCES AND DEVELOPMENTS ON
THE RPC TOF WALL OF THE HADES
EXPERIMENT AT GSI**

Georgy Kornakov Van
Santiago de Compostela
Septiembre de 2012

Universidad de Santiago de Compostela
Facultad de Física
Departamento de Física de Partículas



**NEW ADVANCES AND DEVELOPMENTS ON
THE RPC TOF WALL OF THE HADES
EXPERIMENT AT GSI**

Georgy Kornakov Van
Santiago de Compostela
Septiembre de 2012

D. Juan A. Garzón Heydt
Profesor del área de Física Atómica, Molecular y Nuclear
e la Univ. de Santiago de Compostela

CERTIFICA:

que la tesis titulada:

NEW ADVANCES AND DEVELOPMENTS ON THE
RPC TOF WALL OF THE HADES EXPERIMENT AT
GSI

ha sido realizada por D. Georgy Kornakov Van en el Laboratorio Carmen Fernández (LabCAF) del Departamento de Física de Partículas de esta universidad, bajo su dirección, y constituye la tesis que presenta para conseguir el título de Doctor en Física.

Santiago de Compostela, 30 de septiembre de 2012

Juan A. Garzón

To my friends and family

Contents

Introduction	1
1 HADES past-present-future	5
1.1 HADES spectrometer	6
1.1.1 Tracking system	7
1.1.1.1 Magnet	7
1.1.1.2 Multiwire Drift Chambers	9
1.1.2 RICH	11
1.1.3 Time of Flight detectors: TOF and RPC walls	14
1.1.3.1 TOF	14
1.1.3.2 RPC	15
1.1.4 The Pre-Shower detector	16
1.1.4.1 Electromagnetic Calorimeter	17
1.1.5 The beam detectors: START and VETO	18
1.1.6 The Forward Hodoscope Wall	20
1.1.7 Target	20
1.1.8 Acquisition	21
1.2 Analysis and simulation framework	22
1.2.1 HYDRA	23
1.2.2 Simulation in HADES: PLUTO+GEANT	24
1.2.3 Tracking and Particle Identification	25
1.2.3.1 From fired MDC cell to track candidate	25
1.2.3.2 Matching with RICH and META detectors	27
1.2.3.3 Momentum determination	27
1.2.3.4 Particle Identification	30
2 Gaseous Ionisation Detectors	31
2.1 Interaction of radiation with matter	32
2.1.1 Heavy charged particle interaction	32
2.1.2 Electron and photon interaction	35

2.1.3	Energy losses in thin absorbers	37
2.2	Physics and Measurements in Gaseous Ionisation Detectors	38
2.2.1	Physics of the avalanche	40
2.3	Historical approach to Resistive Plate Chambers	46
3	HADES RPC-ToF Wall	51
3.1	RPC TOF wall goals	51
3.2	Design, geometry, FEE and acquisition of the RPC TOF wall	52
3.2.1	RPC software design	58
3.2.2	The state of art of time of flight RPC based detectors	59
3.3	General purpose RPC digitiser	64
3.3.1	The empirical approach	64
3.3.2	The macroscopic simulation approach	65
4	Performance of the HADES RPC-ToF Wall	71
4.1	Calibration	72
4.1.1	Position calibration	72
4.1.2	Width to Charge calibration	74
4.1.3	Time of Flight calibration	74
4.1.3.1	Offsets with tracking: protons and pions . .	75
4.1.3.2	Slewing correction	78
4.1.3.3	Position - Time dependence correction . . .	79
4.2	Efficiency and position resolution	81
4.2.1	Position resolution	81
4.2.2	System time resolution: START time from tracking+RPC	83
4.2.3	Efficiency	85
4.3	Extended charge study	88
4.3.1	Methods	89
4.3.2	Efficiency determination through the charge spectra	92
4.3.3	Time resolution - charge correlation	93
4.3.4	Streamers probability and correlations with momentum	95
4.3.5	Dependence of efficiency and median charge with particle incidence angle	97
4.3.6	Charge-time dependence	98

4.3.7	Efficiency, median charge, resolution and streamer probability for electrons	99
4.4	Double hit recovery	99
4.4.1	Results of double hits recovery method	102
4.5	Conclusions	104
5	Tracking with Timing: TimTrack	107
5.1	Take advantage of timing detector for tracking	108
5.2	The χ^2 fitting in the parameter space	111
5.2.1	Non Linear TimTrack	113
5.2.2	Constrained TimTrack	115
5.3	TimTrack in a real spectrometer	118
5.3.1	Model	119
5.3.2	Method	125
5.3.3	Results	126
5.3.3.1	Simulation	126
5.3.3.2	Real data	128
5.3.4	Performance	133
5.4	Conclusions	133
6	RPC-ToF wall as a cosmic ray detector	137
6.1	Introduction	138
6.1.1	Influence of the atmosphere in cosmic rays	140
6.1.2	The time and density microstructure of cosmic ray air showers	142
6.2	Signatures from cosmic rays air showers from simulation	144
6.3	Performance of the HADES RPC-TOF wall as a CR detector	145
6.3.1	Special calibration and synchronisation and arrival plane reconstruction methods	145
6.3.1.1	Incidence angle reconstruction	148
6.4	Measured signatures for an advanced study of CR events	150
6.4.1	Front parameters	151
6.4.1.1	Particle multiplicity, mean charge and arrival time distribution	151
6.4.1.2	Front incidence angle comparison with traditional plane fitting	154
6.4.2	Flux of particles	155

6.4.3	Row measured primary energy flux	158
6.5	Conclusions	159

7 Conclusions and Main results 163

8 Resumen 165

8.1	Capítulo 1	166
8.2	Capítulo 2	166
8.3	Capítulo 3	169
8.4	Capítulo 4	170
8.5	Capítulo 5	172
8.6	Capítulo 6	174
8.7	Conclusiones	175

List of Figures

1.1	Schematic layout of the HADES detector	8
1.2	Schematic view of the Magnet; Magnetic field map at midplane between planes; Picture of the magnet during its installation	10
1.3	Layout of the Multiwire Drift Chamber detector	11
1.4	Schematic view of the six sense wire frames inside a MDC; MDC drift cell geometry	12
1.5	Schematic layout of the RICH; RICH photon detector MWPC with CsI cathode	13
1.6	TOF detector	15
1.7	RPC TOF wall	16
1.8	Pre-Shower detector schematic cross section and front views	18
1.9	Front schematic view of the future HADES ECAL	19
1.10	Picture of the START and VETO detectors	19
1.11	Foward Wall scheme	20
1.12	Scheme of the HADES heavy ion Target	21
1.13	TRBv2 (Trigger and Read out Board) picture	22
1.14	Tracks in a Au+Au collision	25
1.15	MDC cluster and track finder	26
1.16	Momentum reconstruction strategies	28
2.1	Energy loss of a μ in Copper	34
2.2	Mean energy loss for several mediums; Ionising penetration range	35
2.3	Fractional energy loss in lead for e^+ and e^-	36
2.4	Photon mean free path in several materials	37
2.5	Energy deposit probability in a thin detector	38
2.6	A positron track photographed in a cloud chamber by C.D. Anderson	39

2.7	Gas filled detectors regions of operation as a function of the applied electrical field	41
2.8	Schematic set up for measurement of induced currents in gases	43
2.9	Representation of electron and ion drift in two geometries	44
2.10	Electron and ion drift and multiplication in a MDC cell	45
2.11	Schematic cross section of the first built RPC detector in two configurations	47
2.12	Schematic cross section of the multigap RPC	48
3.1	The HADES RPC cell cross section picture	53
3.2	Geometric acceptance at the RPC and dimensions of one RPC sector	54
3.3	A RPC sector showing its inner structure and coordinate system	54
3.4	The overlapped structure of the RPC detector	55
3.5	The HADES RPC Front End electronics: DBO and MBO	55
3.6	Representation of several contributions to the measured time by a RPC cell	57
3.7	ALICE RPCs schematic cross section	59
3.8	FOPI RPCs schematic cross section	61
3.9	HARP RPCs schematic cross section	62
3.10	STAR RPCs schematic cross section	63
3.11	Simulated position of the closest primary cluster to cathode in a 4-gap RPC	67
3.12	Avalanche evolution simplified model	68
3.13	Simulated vs measured charge spectra of a 4 gap 0.3 mm RPC	68
3.14	Comparison between measured efficiency of several RPCs and its simulated value	69
3.15	Comparison between measured time resolution of several RPCs and its simulated value	69
4.1	$\Delta T/2$ position calibration distribution	73
4.2	ΔT measured-expected as a function of momentum	77
4.3	Time of flight spectra for proton and pion hypothesis	77

4.4	Synchronisation of the RPC cells after time of flight calibration	78
4.5	Slewing correction of an RPC cell	79
4.6	Correction matrix for one layer of one sector of the RPC for the position-time correlation.	80
4.7	Improvement in time of flight resolution after correcting the time-position dependence	80
4.8	Longitudinal position resolution for RPC cells	82
4.9	Correction momentum matrices for both, positive and negative pions	84
4.10	Recalculated start time from traced particles in the RPC and START detector resolution	84
4.11	System resolution of the time of flight for positive pions	85
4.12	RPC efficiency as a function of the transversal y-coordinate	87
4.13	RPC efficiency modulation as a function of the transversal y-coordinate	88
4.14	Selected particles used in the charge analysis	89
4.15	Efficiency and streamer fraction determination from the charge spectra	91
4.16	RPC efficiency estimated as a function of β and $\beta\gamma$ for pions, protons, deuterium/helium and tritium	93
4.17	Median charge and time resolution as a function of the velocity for pions, protons, deuterium and tritium	94
4.18	Median charge and time resolution as a function of the normalised to mass momentum for pions, protons, deuterium and tritium	95
4.19	Streamer formation probability as a function of velocity β and normalised momentum $\beta\gamma$ for pions, protons, deuterium and tritium	96
4.20	Streamer formation probability as a function of momentum for pions, protons, deuterium and tritium	96
4.21	Efficiency and median charge as a function incidence angle at RPC for protons	97
4.22	Median and resolution behaviour of the Δt distribution as a function of momentum for low charge hits	98
4.23	Median, resolution, efficiency and streamer probability for $e^{\pm 100}$	
4.24	Double hit event in a RPC cell	101

4.25	β vs momentum \times polarity distribution for recovered double hits	103
4.26	Recovered double hits particles in two momenta range . . .	103
4.27	Matching efficiency with double hits recovery algorithm compared with the matching efficiency without the algorithm	104
5.1	Example of 5 ideal planes able to measure both the position and the time	108
5.2	Measured hit positions and times in an ideal detector	109
5.3	General scheme of the TimTrack algorithm	110
5.4	Scheme of the modelling of the matrices needed in the TimTrack algorithm	118
5.5	Schematic representation of multiple saetas reconstruction .	120
5.6	Multi wire drift chamber model for TimTrack	121
5.7	Parametrisation of the drift time in a HADES MDC cell as a function of the impact angle α and distance d	123
5.8	Measurement in a HADES RPC cell	124
5.9	Momentum parametrisation for the Tim Track algorithm . .	124
5.10	Spatial resolution provided by the TimTrack method in the second MDC plane	127
5.11	Time resolution provided by the TimTrack method in the second MDC plane	127
5.12	Momentum resolution for simulated leptons and protons . .	129
5.13	Difference of the TimTrack and Runge-Kutta particle's path	130
5.14	χ^2 vs momentum distribution for simulated data	130
5.15	Distribution of measured-expected times in the four MDC planes	131
5.16	Differences between Runge-Kutta and TimTrack methods reconstructing the path and momentum	132
5.17	Differences between Runge-Kutta and TimTrack methods reconstructing the particles mass	132
5.18	Comparative between distributions of β vs momentum for Tim-Track and Runge-Kutta	133
6.1	Cosmic ray energy spectrum	138

6.3	Comparison between time profile and density of two showers, one originated by a high energy primary cosmic ray and the second by a low energy one.	142
6.4	Lateral distributions of the particle density according to the NKG parametrisations	143
6.5	Characteristic signatures of secondary particles in a simulated cosmic ray shower	146
6.6	Detector and scheme	147
6.7	Time synchronisation and hit distribution for the cosmic ray events	148
6.8	Example of the arrival profile of a high multiplicity shower after calibration and synchronisation	149
6.9	Measured multiplicity and mean charge	151
6.10	Scatter plot of multiplicity vs the standard deviation of arrival times	152
6.11	Arrival time of all the hits within a shower	153
6.12	Azimuth difference analysis $\Delta\varphi$ between the plane fitting algorithm and the track direction method.	155
6.13	Zenith difference analysis $\Delta\theta$ between the plane fitting algorithm and the track direction method.	156
6.14	Flux of events with only one particle and two and tree particles along the five day period	158
6.15	Isoenergetic primary cosmic ray regions super-imposed to the measured σ_t - density distribution	159
6.16	ROW flux of primary particles as a function of the energy of the primary	160
8.1	Esquema del espectrómetro HADES	167
8.2	Sección transversal de las celdas que conforman el muro de tiempo de vuelo de RPCs de HADES	169
8.3	Estructura interna de un plano de RPC y distribución de partículas tomadas con haz de oro sobre oro	170
8.4	Comapración entre un espectro de carga medido y otro simulado para una RPC de 4 planos de 0.3 mm	171
8.5	La mediana de la carga medida y la resolución temporal en función de la velocidad	172

8.6	Reconstrucción de un evento de alta multiplicidad con dos sectores del muro de tiempo de vuelo de RPCs de HADES .	175
8.7	Espectro de flujo de energías de cósmicos primarios obtenido a partir del análisis de los datos tomados durante la puesta a punto con radiación cósmica en HADES	176

List of Tables

1.1	Characteristic properties of light vector mesons ρ, ω, ϕ . . .	6
1.2	MDC detector geometry	12
1.3	MDC detector operational voltage and wires main characteristic	13
1.4	Comparative table of the TRB evolution	23
2.1	Classification of particles according their interaction	32
4.1	Variables accessible in the RPC charge study	90

Introduction

Advances in nuclear and particle physics from the XX century until present, cannot be explained without the development of gaseous detectors. Since Hans Geiger invented his gaseous counter for alpha particles detection in 1908, the story of great discoveries is closely connected to improvements and specialisation of this kind of detectors.

Investigations of the alpha radiation done by Ernest Rutherford, Hans Geiger and Ernest Marsden lead to the discovery of the first nuclear model, which was an important breakthrough in understanding the matter structure and how the radiation interacts with it.

Nowadays, a wide range of gaseous detectors are present in different experiments. We can find configurations that perform several tasks such as triggering, tracking and timing. Limits are set by our imagination. When a charged particle go trough a detector, some variables can be measured by its interaction with the gas within the detector. Even neutral particles can interact with matter by producing secondary particles as photons, leptons or hadrons, which can be detected.

In the first part of this thesis we will introduce the HADES experiment and the physics it is addressed to. A brief description of its subsystems and a general overview of the data acquisition and software is done in Chapter 1. The theory underneath gaseous ionisation detectors such as the Resistive Plate Chambers, RPC, and an historical introduction of these detectors is done in Chapter 2. The design goals, geometry and general building aspects of the HADES RPC TOF wall is reviewed in Chapter 3. Concluding on the background aspects, a simulation of the RPC response code is shown in the same Chapter.

Heavy ions collisions offer to the study of the performance of the RPC detector a wide range of particles. In 2011, HADES took test data for the first time with a gold beam on gold target at 1.24 GeV. One year later, the system was ready to have a full beam time with Au+Au. The data acquired during the both beam times, offer a outstanding opportunity to perform a deep analysis of the RPCs behaviour, performance and

properties. The information coming from the others subsystems of the spectrometer allows us to evaluate the behaviour of the detector under heavy radiation environment, mostly protons, pions, leptons and heavier systems as helium, deuterium or tritium. The efficiency, time resolution and charge observables for each particle is examined in depth in order to provide a better understanding of the detector response in Chapter 4.

In the past few decades, some remarkable advances in electronics and computing bring to light a new set of detectors which can measure, with high accuracy time, position, energy or several of them together at the same time. In Chapter 5 we try to tame tracking with timing. A new minimum chi square method called TimTrack, developed by our group, is proposed, analysed and implemented within the HADES tracking software. The main difference of the proposed method for particle reconstruction is the direct use of time information measured by the timing detectors instead of doing some pre-transformations with the possible loss of valuable information. The output of the algorithm returns the properties of a particle as the position, direction, time and velocity in a vector of parameters which we call SAETA (SmAllest sEt of daTA). Here, we present a matrix based development for the sake of clarity. In the first part of the chapter the tracking with timing is analytically studied, showing the algebraic core for linear and non-linear models. However, the reality is always more complex than a theoretical model. It is thus essential to show its performance in real life, like the HADES spectrometer.

Before installing the RPC wall at the spectrometer, all the sextants were verified in a test under cosmic ray radiation during two months. The test was performed by stacking pairs of detectors horizontally. Despite the acquired data was thought to be only for calibration and intrinsic analysis, it offered the possibility of performing complementary analysis. Those data are analysed in Chapter 6 from the point of view of cosmic ray physics. Besides the necessary specific strategies followed to calibrate and synchronise all the cells, we show the measured signatures of cosmic ray events seen by a high granularity and a high time resolution detector. The analysis of the signatures of the showers micro-structure is accompanied by a Monte Carlo simulation of cosmic ray showers. A special part is dedicated to different rate and other time-dependent measurements that may be very interesting from the point of view of the climate, atmospheric or low-energy cosmic ray physics. To conclude this chapter, a discussion of

the physics and perspectives of small installations with high performances both in time and track reconstruction is done.

Finally, in the Chapter 7, we summarise the main results concerning the response of the RPC detector.

1 HADES past-present-future

The study of hadron properties inside the nuclear matter medium is of fundamental interest within the realm of Nuclear Physics. Theoretical models based on non-perturbative Quantum Chromodynamics predict a modification of some hadron properties such the mass or the resonance width when they are produced embedded in nuclear matter [1]. These investigations may shed light on how processes happened at the very beginning of our universe or those which take place in the latter stage of stars evolution as neutron stars.

The High-Acceptance DiElectron Spectrometer, HADES¹ has been designed to measure in medium modifications of the properties of the light vector mesons ρ , ω , ϕ [2]. The electromagnetic decay branch of these vector mesons into e^+e^- pairs make them suitable to study strong interacting matter regarding two main reasons: the first one is that produced leptons can zip through and abandon the strong interacting medium undistorted, providing a clean signal of the matter phase. The latter is the short life time of vector mesons which is comparable to the life and size of the compression phase of relativistic heavy-ion reactions in the 1-2 A·GeV regime. However, the e^+e^- branching ratio of the vector mesons decay is very small (around 10^{-5} of all decays; see Table 1.1 for the main characteristic of the light vector mesons), setting a strong constraint to the design features of the spectrometer and detectors. For that reason, high acceptance and resolution of detectors are required.

Other experiments have already analysed several aspects of the phase transition between the hot and dense matter and the normal matter. The NA49 experiment [3] at CERN was designed for the study of the production of charged hadrons and neutral strange particles in Pb+Pb collisions up to 158 AGeV. This experiment has shown some evidences of anomalies, respect the ones predicted by the lattice QCD as possible signals of the deconfinement phase. The CERES/NA45 experiment [4], also at CERN,

¹Greek God of the Underworld

has analysed the e^+e^- production in relativistic nuclear collisions. It has observed that the yield of low mass dilepton pairs produced in Pb-Au collisions in the mass region 0.2-0.7 GeV, exceeds by a significative factor the expected values. The result is consistent with the expectation that the properties of vector mesons change when they are produced in dense matter.

Of special interest is the DLS (Dilepton Spectrometer)[5], at Bevalac, that studied the e^+e^- production at comparable energies that HADES although at a slightly different phase space region. DLS reported a dilepton enhancement at the η region that HADES has confirmed as being produced essentially by the pn-Bremsstrahlung and the Dalitz decay of the Δ resonance.

The HADES spectrometer has also shown a very good capability for analysing strangeness particle production: among other studies, the double strange decay of the ϕ meson has been observed in agreement with the so called statistical models but these fail describing the Ξ and η states.

Meson	Mass, (MeV/c ²)	Decay Width, (MeV/c ²)	Lifetime (fm/c)	Branching ratio e^+e^-
ρ	769	146	1.3	$4.72 \cdot 10^{-5}$
ω	782	8.49	23.4	$7.28 \cdot 10^{-5}$
ϕ	1020	4.26	44.4	$2.96 \cdot 10^{-4}$

Table 1.1: Characteristic properties of light vector mesons ρ , ω , ϕ . Values are weighted average of reported measurements by several experiments. Data has been taken from [6]

1.1 HADES spectrometer

Barely, the HADES spectrometer is composed by six identical sectors covering polar angles between $\theta = 18^\circ$ and $\theta = 85^\circ$ with 85% of azimuthal acceptance. Momentum reconstruction and tracking relies on a system composed of a toroidal magnetic field produced by superconducting coils and four planes of Multiwire Drift Chambers (MDC) located before and after the magnetic field region. Electron identification is performed with the hadron-blind gas Ring Imaging Cherenkov detector (RICH) together with the Multiplicity and Electron Trigger Array (META) detector composed of three elements i.e. a time-of-flight scintillator wall (TOF), a timing RPC

wall (RPC TOF) and an electromagnetic shower (Pre-Shower). Also there are two beam detectors: START and VETO. A schematic view of the spectrometer is shown in the Fig.1.1. The spectrometer was substantially upgraded in the 2007-2010 period to accomplish its scientific program in heavy ion collisions. The aforementioned scheme was not the initial one, and since 2009, several subsystems such as the low angle time of flight scintillator detector (TOFINO) or the trigger and acquisition were gradually replaced by new developments. Also, in 2007, an hodoscope (FORWARD HODOSCOPE WALL) was installed to measure the impact parameter and the reaction plane and it is expected to replace the Pre-Shower detector by a Electromagnetic calorimeter in the future. A overview of all the subsystems and the analysis and simulation framework can be found below.

The HADES spectrometer is placed at the GSI (Gesellschaft für Schwerionenforschung) in Darmstadt, Germany. The accelerator SIS18 provide beam energies of 1-2 AGeV.

1.1.1 Tracking system

1.1.1.1 Magnet

The momentum reconstruction is obtained in HADES by measuring the trajectory bending within a magnetic field. The main constraints on the design of the magnet are:

- Provide a transverse kick to charged particles in order to obtain their momenta with resolution of the order of $\sigma_p/p < 2\%$ for electrons together with the tracking detectors².
- Compact construction and a low loss of solid angle caused by the coils.
- A field free region around the target and inside the RICH active volume.

²This condition set two additional constraints, on tracking detector as it requires a position resolution of the order of $150\mu\text{m}$ and a low multiple scattering probability in the high field region, i.e. free detector region.

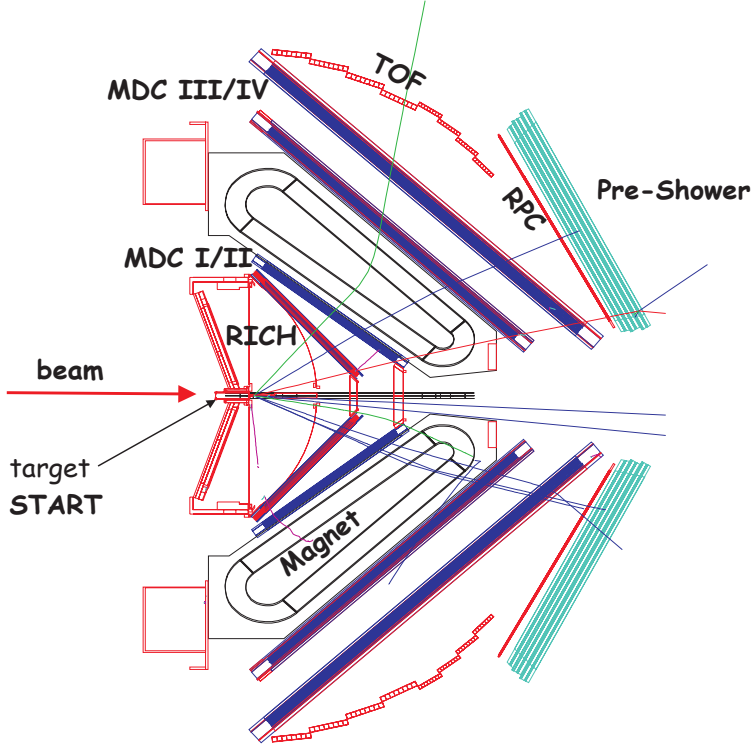


Figure 1.1: Schematic layout of the HADES spectrometer. Two of six sectors are shown. Starting from left to right we can find the beam detector START responsible of providing the starting time to all the detectors, the interaction target, the hadron-blind gas Ring Imaging Cherenkov detector (RICH), a couple of Multiwire Drift Chambers (MDC) before the superconducting coils and a couple of them after responsible of tracking and momentum reconstruction, the META detectors: a scintillator time of flight wall (TOF), a resistive plate chambers time of flight wall (RPC) and a electromagnetic shower detector (Pre-Shower). At the right side and separated several meters is emplaced the Froward Wall detector whose main purpose is to detect the spectator particles and the event plane in Au+Au collisions[2].

- Use of light materials in order to reduce the production of secondary particles.

These constraints require a Iron-Less Super conductive Electromagnet (ILSE) [7], consisting in 6 coils surrounding beam axis which generate a field with toroidal geometry. Each coil is contained in an isolated vacuum chamber refrigerated with Nitrogen and Helium³. It is made of 140 turns and operates at a maximum current of 3464 A, giving a magnetomotive force of 485000 Ampere-turn. The maximum magnetic field created amount to 3.6 T inside the coil and of 0.7 T between coils. After installation, the field was mapped with Hall probes and corrected for the Earth magnetic field. This map is used to calculate particle deflection angles. A side view of the magnet, the field map and a picture from its installation is shown in Fig. 1.2.

1.1.1.2 Multiwire Drift Chambers

Tracking in HADES relies on the Multiwire Drift Chamber detector. This detector provides position, direction, energy loss and momentum, through the trajectory bending in the magnetic field created by the superconductor coils. It was designed to meet the requirements of the experiment [8][9], which are:

- Intrinsic spatial cell resolution below 150 μm .
- Low multiple scattering probability.
- High efficiency and large acceptance.
- Efficient track reconstruction in high multiplicity environments⁴.

The detector layout is shown in the Fig. 1.3. Technically, each MDC plane is composed of 7 cathode planes and 6 sense/field layers in six different stereo angles⁵. This geometry improves resolution in the magnetic kick direction (polar). Besides, within each module we can find about 1100

³Nitrogen refrigerates the shielding to 85 K and Helium the current leads at 4.7 K.

⁴30% of cell occupancy for Au+Au at 1 AGeV.

⁵The wires are oriented at 40°,20°,0°,0°,-20°,-40° in the module coordinate system. The central layers at 0°, are shifted one in relation to the other half cell width in order to have an unambiguous measurement of the position.

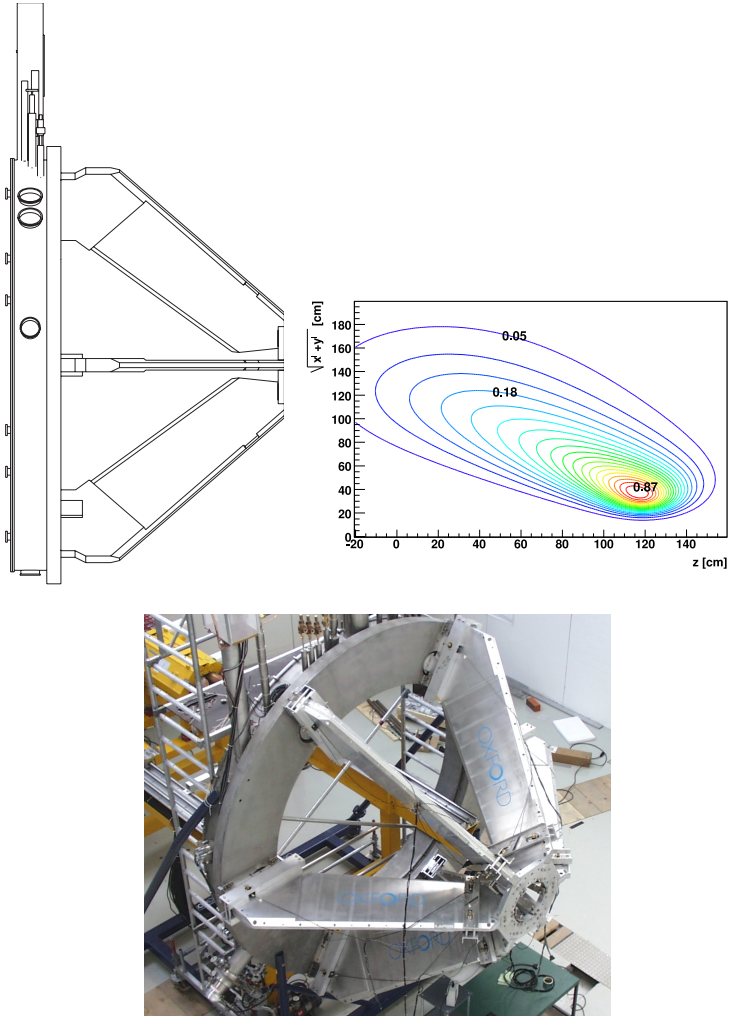


Figure 1.2: Top-Left, schematic layout of the Magnet;Top-right, magnetic field map at midplane between planes; Bottom, picture of the magnet during its installation in the HADES cave[2].

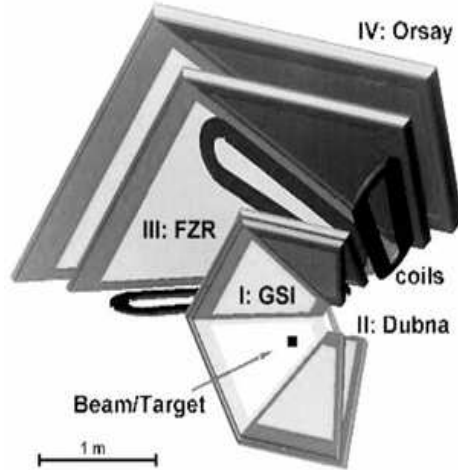


Figure 1.3: Layout of the Multiwire Drift Chamber (MDC) detector. The identical six sectors, with 4 planes with variable size to provide a wide polar coverage (18° - 85°) are shown. Notice the magnet coils embedded between MDC plane II and III[2].

drift cells, with increasing size; from $5 \times 5 \text{ mm}^2$ in the innermost plane to $14 \times 10 \text{ mm}^2$ in the outermost one. To compensate the different cell sizes and keep the performance, the voltage applied to the cathode and field wires varies from -1375 V to -1700 V . Wire length also played a role in order to select an optimum diameter and material. The gas mixture is made by Argon (Ar) and Isobutane (C_4H_{10}) in a ratio 84/16⁶. A summarised description of all chambers from geometry to operational voltage and wire information is given in the tables 1.2 and 1.3. The drift cell schematic view and the 6 layer layout are shown in the Fig. 1.4.

1.1.2 RICH

The threshold Ring Imaging Cherenkov (RICH) detector is designed to identify relativistic e^\pm with momenta $0.1 \text{ GeV}/c \leq p \leq 1.5 \text{ GeV}/c$ in the

⁶MDC plane I was rebuilt in 2009 replacing Al wires by Cu/Be and the gas mixture by an ArCO₂ at 70/30 in 2011. Therefore the voltage was increased to compensate the loose in gain to -1750 V .

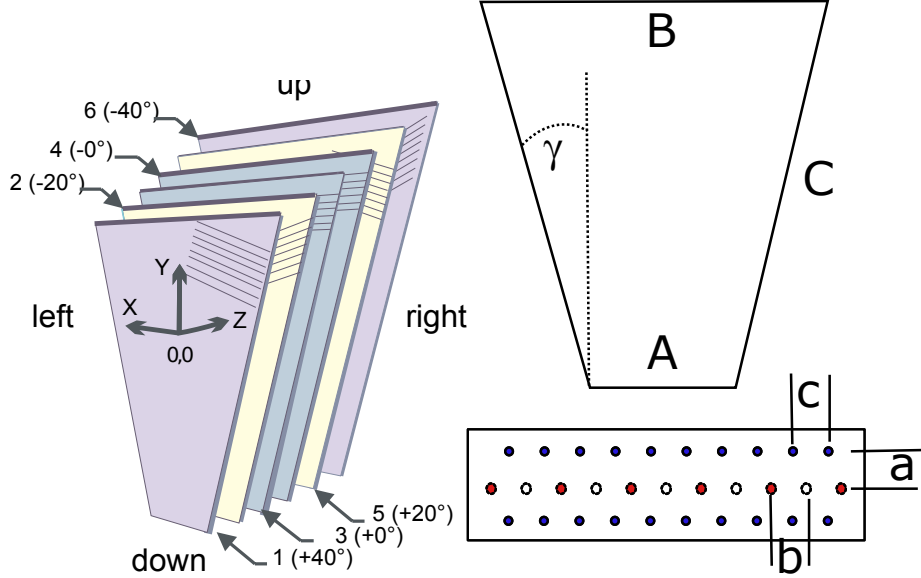


Figure 1.4: Left: Schematic view of the HADES MDC six sense wire frames with its characteristic angles and the main geometrical parameters which define the MDC[2]. Right: Geometry definitions of the MDC chambers and schematic view of the drift cell geometry. The distances between the sense wires (white), field wires (red) and cathode (blue) are shown.

Plane	A (mm)	B (mm)	C (mm)	α (°)	a (mm)	b (mm)	c (mm)
MDC Plane I	139,21	767,38	839,19	21,98	2,5	2,5	2,0
MDC Plane II	205,00	905,00	1049,27	19,49	3,0	2,6	2,0
MDC Plane III	310,43	1804,80	2139,05	20,44	6,0	4,0	3,0
MDC Plane IV	345,46	2224,05	2689,04	20,44	7,0	5,0	4,0

Table 1.2: MDC detector geometry

Plane	Operational Voltage (-kV)	Wires					
		Cathode		Field		Sense	
		Material	$\phi(\mu\text{m})$	Material	$\phi(\mu\text{m})$	Material	$\phi(\mu\text{m})$
MDC Plane I	1.4	a.b. Al	80	a.b. Al	80	g.p. W	20
MDC Plane II	1.4	a.b. Al	80	a.b. Al	80	g.p. W	20
MDC Plane III	1.5	a.b. Al	80	a.b. Al	100	g.p. W	20
MDC Plane IV	1.7	g.p. Al	100	g.p. Al	100	g.p. W	30

Table 1.3: MDC detector operational voltage ⁶ and main wires characteristics. The field values correspond to a gas mixture of Ar+Isob 84/16. Abbreviations: (a.b. Al) annealed bare aluminium; (g.p. Al) gold plated aluminium; (g.p. W) gold plated wolfram

environment of up to 200 charged particles per event[10]. It consists on a gaseous radiator (C_4F_{10}), a spherical vacuum ultra violet (VUV) carbon shell mirror and a fast gaseous photon detector with a CsI photon converter cathode. The layout is shown in the Fig. 1.5a.

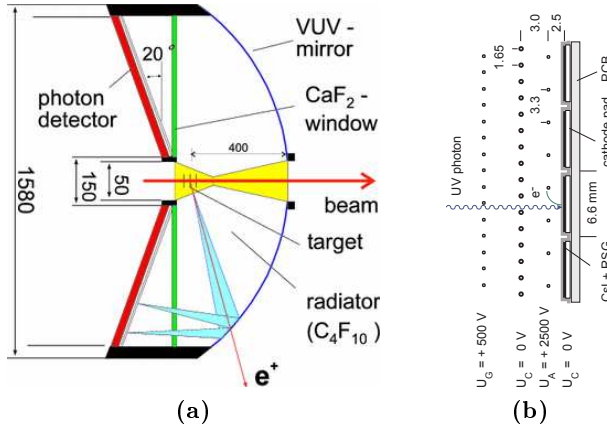


Figure 1.5: a) Schematic view of Ring Imaging Cherenov (RICH) detector. b) Detail of the multi wire proportional chamber (MWPC) detector with CsI cathode which convert the UV photons of Cherenkov light[2].

The RICH constitutes the innermost part of the spectrometer. For that reason, the photon detector is placed upstream of the target to minimise the impact of strongly ionising charged particles emerging from the reac-

tion zone. The radiator offers an adequate transmission coefficient down to 145 nm and a Cherenkov threshold (Lorentz factor $\gamma = 18$) which makes it blind for hadrons and heavier leptons in the HADES energy regime. The Cherenkov light rings produced in the radiator is reflected by the mirror towards the photon detector. There, the ultra violet photon is converted in an electron in the CsI cathode of the multi wire proportional chamber (MWPC), filled with Methane (CH_4), where is accelerated by an electrical field of 2450-2500 V, providing a gain of $3\cdot 9\cdot 10^4$ [11].

1.1.3 Time of Flight detectors: TOF and RPC walls

The HADES system for measuring the time of flight of the particles, and hence its identification together with information provided by the tracking detector, is composed by two detectors with different technologies. At high polar angles, $44^\circ < \theta < 88^\circ$, a scintillator TOF array performs the time measurements. At low polar angles, $12^\circ < \theta < 45^\circ$, time measurement relies on the RPC based detector. Initially, at low polar angles, also a low granularity scintillator array called TOFino was installed but, as a part of the HADES upgrade program, it was substituted by the RPC wall in order to facilitate measurements with heavy systems as Au+Au. Both detectors are placed behind the outer tracking detectors upstream the beam line.

1.1.3.1 TOF

The relatively small particle flight path from the target to the Time of Flight wall requires a time resolution better than 150 ps in order to provide the necessary particle identification [12]. For that purpose, at high polar angles it was decided to build a detector with scintillator rods covering the six sectors of the spectrometer, using BC408 from Bicron⁷ as scintillating material. The rod cross section range from $20 \times 20 \text{ mm}^2$ to $30 \times 30 \text{ mm}^2$ and the lengths range from 1475 to 2365 mm. The rods are coupled on both ends to fast photomultipliers EMI 9133B, each of them provide a time t and a signal amplitude a . With that information, combining measurements at both sides can be extracted:

$$t_{tof} = \frac{1}{2} (t_{right} + t_{left} - l/v_g) , \quad (1.1)$$

⁷BICRON, 12345 Kinsman Road, Newbury, OH 44065, USA

$$x_{tof} = \frac{v_g}{2} (t_{left} - t_{right}) , \quad (1.2)$$

$$y_{tof} = y_{rod}, \quad (1.3)$$

$$\Delta E = k \sqrt{a_{left} \cdot a_{right}} e^{L/\lambda_{at}} , \quad (1.4)$$

where *left* and *right* subindexes refers to the left and right scintillator rod end, L is the rod length, v_g is the group velocity, λ_{at} is the light attenuation length of the rod and k is a constant[13]. The TOF detector is shown in the Fig.1.6.



Figure 1.6: Picture of the TOF wall detector during its installations on the HADES mechanical support frame. All the six sectors are visible. The two opposite detectors, which are in the center of the picture, are two sectors of the Pre-Shower detector.

1.1.3.2 RPC

The Resistive Plate Chambers Time of Flight wall was designed [15] to replace the low granularity scintillator array at low polar angles, TOFino. Its schematic layout is shown in the Fig.1.7. The experiment required a time resolution below 100 ps and a high granularity in order to be capable

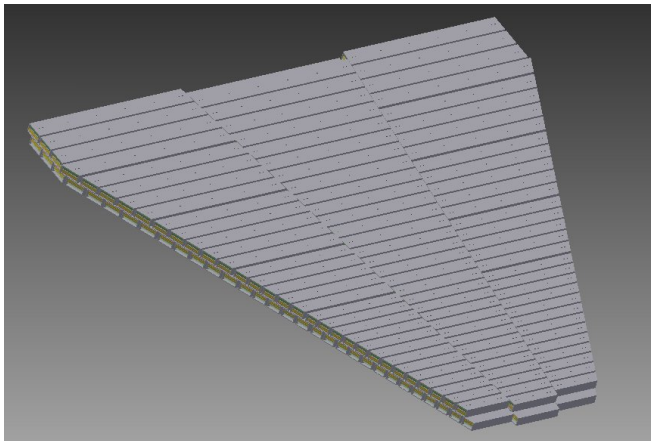


Figure 1.7: Cell layout of the Resistive Plate Chambers Time of Flight detector. Its internal structure consists on electrically shielded RPC cells, read-out at both sides, distributed in rows, columns and two layers[14].

of performing its functions in central heavy ion collisions and the foreseen energies at SIS100.

As this work is related with the RPC wall development a detailed overview of the RPC detector will be given in Chapter 3 and 4.

1.1.4 The Pre-Shower detector

The main aim of the Pre-Shower detector is to identify e^\pm by means of electromagnetic shower detection at forward angles. It is located downstream, behind the RPC TOF wall and fixed to it. As other HADES subsystems, it is composed by six identical sectors of trapezoidal shape. The electromagnetic shower is produced in two Lead converters of $2X_0$ and $1.5X_0$, where $X_0 = 0.56$ cm is the Lead radiation length. Showers evolution is measured by three wire chambers: pre-chamber, post-chamber and post2-chamber. The pre-chamber is located before the Lead converters and its aim is to provide a hit reference position and a value to compare to the other two chambers, located after the converters. These chambers are filled with an isobutane-based gas mixture and operate in the self-quenching streamer mode, in order to minimise influence of non-MIPS particles as protons,

which can release larger energies after passing through Lead plates.

Each wire chamber is arranged into 942 pads to allow individual read-out. They are distributed in 32 rows and 32 columns[16], as it is shown in the Fig. 1.8. The charge measurement is performed as follows: first a local maximum is found in the pre-chamber and then, the charge of the 8 neighbours surrounding the local maximum is integrated in all the three chambers. These three values: \sum_{pre} , \sum_{post1} , \sum_{post2} are used to identify electrons because these values and the ratios among them evolve as a function of momentum and do allow to discriminate the hadron background. The two usual algorithms are:

$$\frac{\sum_{post1}}{\sum_{pre}} \geq T_{S1}(p) \quad \text{or} \quad \frac{\sum_{post2}}{\sum_{pre}} \geq T_{S2}(p), \quad (1.5)$$

$$\sum_{post1} + \sum_{post2} - \sum_{pre} \geq T_{SD}(p), \quad (1.6)$$

where $T_{S1}(p)$, $T_{S2}(p)$ and $T_{SD}(p)$ are threshold values as a function of particle momentum.

To improve the particle identification and include photon detection, it is foreseen to replace soon the Pre-Shower detector by an Electromagnetic Calorimeter, which is described below.

1.1.4.1 Electromagnetic Calorimeter

One of the steps toward the HADES upgrade in order to continue its scientific program at FAIR energies is to replace the Pre-Shower detector by an Electromagnetic Calorimeter ECAL. This one will allow a better lepton identification in collisions at energies up to 8 AGeV. Furthermore, photon measurement would be of large interest for the HADES strangeness program. The design and simulation study of the new detector is widely discussed in its Technical Design Report (TDR) in [17].

Barely, the new detector will cover the same forward angles as the Pre-Shower. Also, the RPC TOF wall will be coupled at the new frame of the calorimeter, setting a constraint on the design. Each sector is composed by 163 modules distributed in 15 layers, as it is shown in the Fig. 1.9.

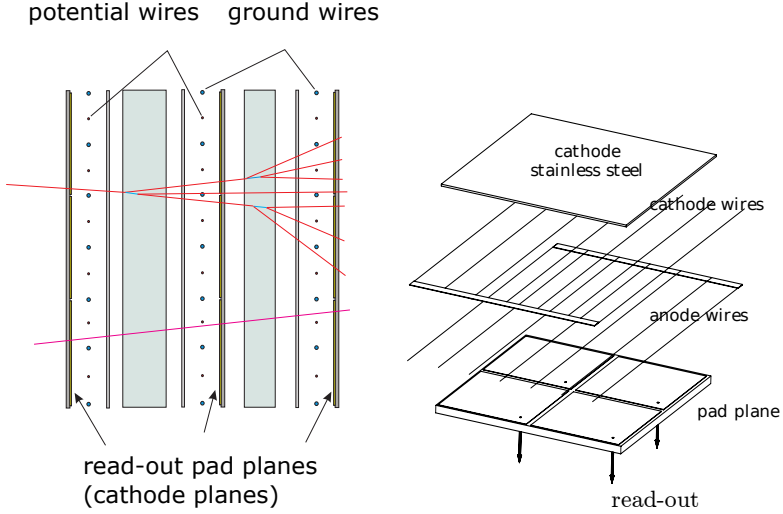


Figure 1.8: Left: Pre-Shower schematic cut. The two Lead converters between the three wire chambers and the different response to different particles are shown. Right: Schematic drawing of a wire chamber with the read out pads is shown[2].

1.1.5 The beam detectors: START and VETO

The beam detector START is used to provide a high resolution start time of the collision to other subsystems especially to timing detectors, i.e. TOF and RPC. To achieve this goal, a CVD (Chemical Vapour Deposition) diamond detector was designed and build [18][19].

The main properties of the detector are the high efficiency charge collection and the fast signal collection time, together with a low interaction with beam ions achieved reducing the thickness to $50 \mu\text{m}$. The metallisation of the START detector consist of a 50 nm Cr layer and a 150 nm Au layer arranged in 16 stripes of $200 \mu\text{m}$ at each side of the diamond providing x-y position measurement. The VETO detector, located 70 cm downstream the target, is made of $100 \mu\text{m}$ polycrystalline material and is aligned within the beam line axis, with the START and the target.

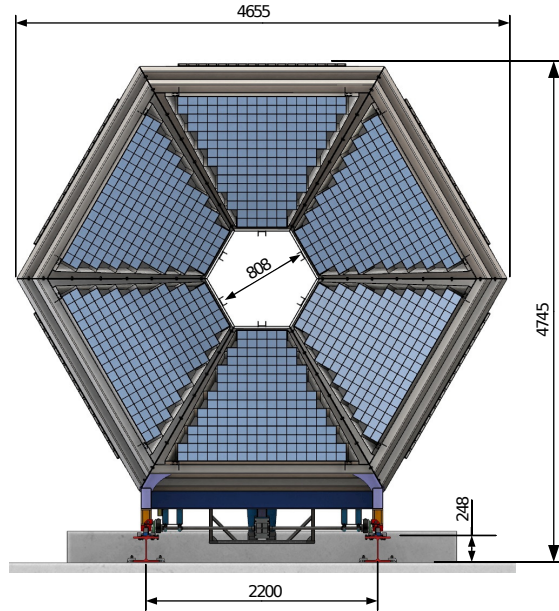


Figure 1.9: Front schematic view of the future HADES Electromagnetic Calorimeter. The picture has been taken from [17]

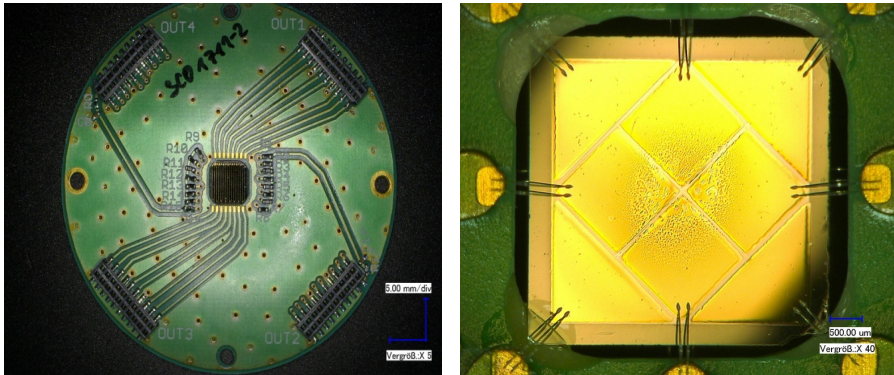


Figure 1.10: Left: Picture of the START detector used in the April 2012 experiment. Right: Picture of the START detector used in August 2011 after the experiment. Notice the beam spot at the center of the detector. This configuration was used as VETO detector in April 2012 experiment. Pictures taken from [18].

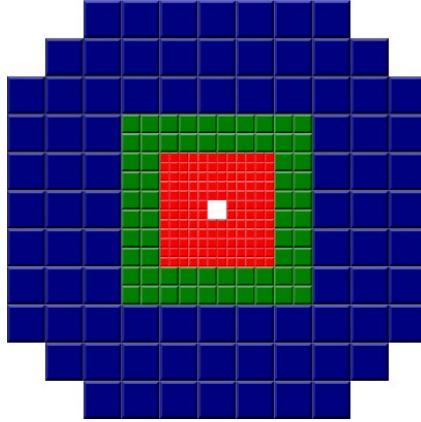


Figure 1.11: Scheme view of the scintillators of the Forward Wall. The three cell size regions are highlighted with red ($40 \times 40 \text{ mm}^2$), green ($80 \times 80 \text{ mm}^2$) and blue ($160 \times 160 \text{ mm}^2$) colors.

1.1.6 The Forward Hodoscope Wall

The goal of the Forward Wall detector is to measure the spectator particles at low angles: $0.33^\circ < \theta < 7.1^\circ$. This angular region is not covered by any other sub-system in the HADES spectrometer. The wall is placed 7 m behind the target. The arrangement consists of 287 cells composed of three different size scintillators coupled to photomultipliers. Scintillator cells have sizes of $4 \times 4 \text{ cm}^2$, $8 \times 8 \text{ cm}^2$ and $16 \times 16 \text{ cm}^2$. The cells are placed in the following way: the smallest ones are placed at the center at the lowest polar angles, the largest cover the outer part of the wall and the medium ones cover the intermediate angles. Placed in this way, the position resolution keeps at a reasonable value. The momentum resolution for protons is about 11%, estimate wall time resolution is about 0.5 ns.

1.1.7 Target

The HADES experiment requires various targets. In case of elementary reactions, as p+p or d+p, a liquid hydrogen target is used. This target was developed at IPN Orsay and consists of a vessel built out of Mylar foils containing liquid hydrogen at atmospheric pressure and kept at a temperature of 20 K.

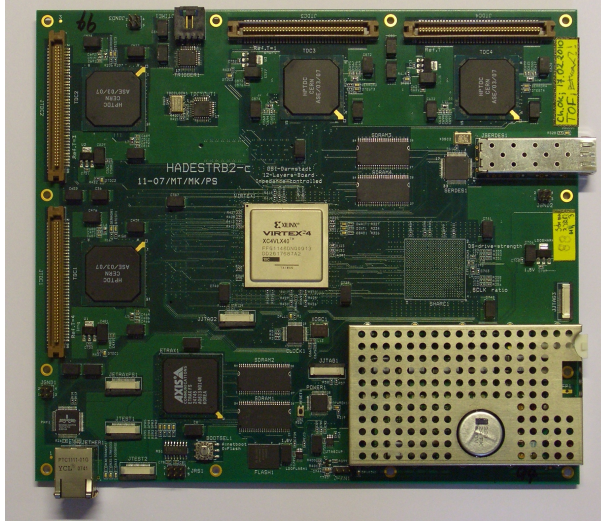


Figure 1.13: Picture of the TRBv2 used for acquisition in the HADES experiment.

price per channel.

Besides its characteristics, the TRB board allows to extend its functionality or accommodate the read out for several designs through add-ons, as implemented for several HADES sub-systems[27][28][29].

The main aim of the upgrade of the acquisitions and trigger scheme was the increase of the event rate capabilities to reach 20 kHz in heavy ion collisions and 100 kHz in light systems. The readout of the detectors for that purpose is performed via optical communications.

1.2 Analysis and simulation framework

The HADES data analysis is performed within the HYDRA⁸ framework, based on ROOT⁹ [30]. Furthermore, for simulation studies is used GEANT3¹⁰

⁸Hades sYstem for Data Reduction and Analysis.

⁹Data analysis framework, written in C++, developed at CERN for nuclear and particle physics.

¹⁰GEometry ANd Tracking

Version	TRBv1	TRBv2	TRBv3
Nchan	128	128	256
σ_t	25-780 ps	25-780 ps	<10 -14 ps
TDC	4 HPTDC	4 HPTDC	4 FPGA
ReadOut	100MBit/s	2Gbit/s	8xSFP trans ¹ .
Processor	ETRAX	ETRAX-FS+FPGA	FPGA

Table 1.4: Comparative table of the Trigger and Readout Bord (TRB) from versions v1 to v3. ¹ These connections can be configured as GbE-links or as optical links >2Gbit/s.

[31] package and as an event generator for simulation studies and as an input source for GEANT, a ROOT-based code called PLUTO++ [32].

Within the aforementioned software packages particle tracking and identification is performed. The available number of read-out channels, the compact design of the spectrometer, the particle density and the required quality of the fitted track parameters sets strong constraints on the used algorithms.

Below in this section a short introduction to the framework and the stages needed to transport information measured by the detectors to a identified particle are explained.

1.2.1 HYDRA

The main goal of the HYDRA framework is the processing of events recorded in the HADES spectrometer. For such a purpose, object oriented programming allows modularity and polymorphism holding that the key to further extensions. A framework is a concept much wider than a class library, as it has its own internal logic and structure. Besides, interaction can be done in several levels depending on the final user and on its programming knowledge and, of course, it will depend on the thread. The ROOT class package underlies the HYDRA framework and provides a broad and comprehensive environment which, in fact, became a standard in nuclear and particle physics. ROOTs user interface allows interact dynamically with the data through interpreted macros, compiled macros, full programs based on its classes and even provide an intuitive graphical

interface (GUI).

The framework classes are distributed in modules in the following way:

- The fundamental class HADES which encapsulates and coordinates the whole reconstruction.
- The classes which store data both real and simulated, from detectors or from several analysis levels e.g. raw, cal or hit data from detectors or track candidates after reconstruction algorithms.
- The classes which manage O/I.
- The classes which manage parameters.
- The classes which manage algorithms.

The data output relies on the TTree and the TClonesArray ROOT classes[33], allowing fast and simple manage of huge amount of data. Parameters needed to manage and transform the data can be stored and introduced in several ways: through an Oracle¹¹ data base, plain text or ROOT files. Details of the HYDRA class design is given in [34].

1.2.2 Simulation in HADES: PLUTO+GEANT

For simulation studies, an event generator was developed within HADES, suitable for the study of hadronic interactions at SIS and FAIR energies. It is not completely fair call PLUTO++ an event generator as it is more than this: it is a framework to generate events. Its modular structure and its extension possibility allows to implement and to control almost all kinematic variables and exchange the physics models which have to be compared to measured data.

As HYDRA, PLUTO++ uses an object-oriented structure and it is launched interactively within the ROOT environment. The produced output can be analysed itself or can be used as input for a further analysis, which includes the performance of the detectors and the whole geometrical environment of the experiment. The simulation of the trajectories of the particles zipping through the spectrometer from the interaction zone, generated with PLUTO, is done with the Monte-Carlo GEANT. Details of the PLUTO class design, its methods and models is given in [32].

¹¹Oracle Corporation, 500 Oracle Parkway, Redwood Shores, CA 94065, USA

1.2.3 Tracking and Particle Identification

Tracking and particle identification are very important steps in any Nuclear or High Energy Physics experiment. Without an accurate, robust and fast reconstruction tools would be complicated, or even impossible, to achieve the goals of the experiments.

The reconstruction is done in several steps, from clustering correctly the fired MDC wires to finally provide a full reconstructed track with all the important information retrieved from all the subsystems that can allow a particle identification as good as possible. If we look, for example, the fired wires, cells, pads, etc of all the detectors of the spectrometer in a Gold-Gold collision, we will find an overwhelming jungle, where to find a good track is as difficult as looking for a needle in a haystack. The picture Fig.1.14 sets a good starting point to explain how from that jumble we can arrive to a clean and accurate reconstruction of the event.

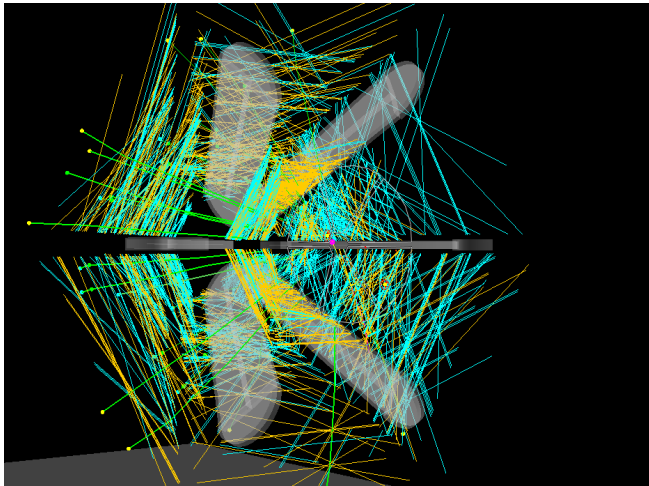


Figure 1.14: Particle's tracks produced in an event. Light blue and yellow lines are fired MDC wires[35].

1.2.3.1 From fired MDC cell to track candidate

The track reconstruction task is not completely independent from momentum reconstruction, however, for the sake of clarity these tasks are split.

To understand better the reconstruction of the particle trajectory from the signals measured in the MDC cells we can imagine a spider web, but instead the usual, one formed by multiple layers. The three dimensional intersections of the strands will depend on our point of view. Thus, if we want to find the path of a particle, we must first decide the best possible projection, because finding clusters in a three dimension space is harder that doing it in a two dimension one.

The MDC system, at this point, tries to find segments in the pairs of chambers placed before and after the magnet. If we assume that particles pass through them following straight trajectories, in order to find the wire clusters we project our drift cell areas in a projection plane[36], as shown in the Fig.1.15. These clusters are fitted through a least squares method explained in detail in the Section 2.2, as it is dependent on avalanche physics in gases[37].

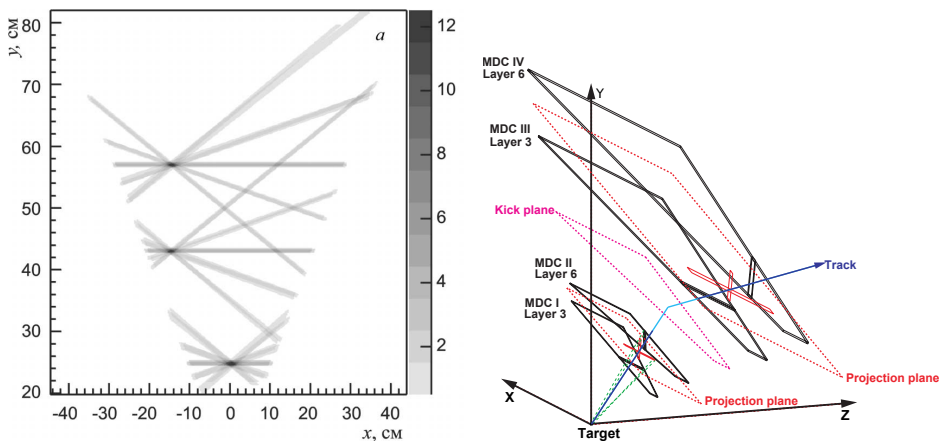


Figure 1.15: Left: MDC wire cluster finder method. Right: Schematic representation of the track finder [36].

Both the outer and inner segments are now matched among them to define the first track candidates through the kick plane method. This method is explained better in 1.2.3.3.

1.2.3.2 Matching with RICH and META detectors

The selection of particle candidates and its identification is done with the help of the Cherenkov detector installed close to the target and the META detectors placed downstream, after the tracking system. The different candidates of particle trajectories are projected forwards and backwards to find intersections with other detectors of the spectrometer. As a first approach it is assumed a straight trajectory outside the tracking system, neglecting the weak magnetic field outside MDC chambers. Those hits in the detectors are sorted by its matching quality: the square deviation between the projected hit position and the measured one, normalised by their errors. These errors are stored in the Oracle data base and are provided by each detector. The methods to obtain these errors are detector-dependent, and in Section 4.2 is devoted to explain the RPC-TOF wall procedure.

1.2.3.3 Momentum determination

The momentum reconstruction follows a three-stage process. Besides the historical reasons leading to the existence of the three algorithms, each one provides specific precision-time cost performance needed for reconstruction tasks and provide a start value for the next one. These three algorithms are namely: the Kick-Plane method[34], the Spline method [38] and the Runge-Kutta method[39]. The first one uses the inner MDC segment and a position given by the META detectors to calculate momentum. The Spline method uses positions from both MDC segments. The latter one, as Spline, uses all the available tracking information, improving the results of Spline. The last two are standard methods to reconstruct the momentum in systems based on deflection by a magnetic field. A schematic explanation of the three methods is shown in the Fig. 1.16.

Though the three methods combined provides an accurate solution, some physical properties of particle motion are neglected. To include such effects as energy loss and multiple scattering, a Kalman Filter algorithm is being developed[40].

Regarding performance, the achieved momentum resolution is better than 4% for all particles.

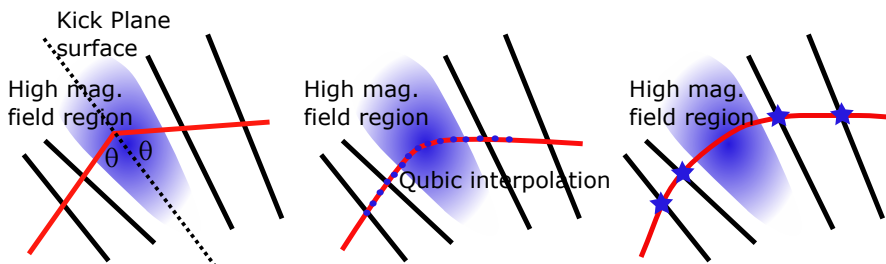


Figure 1.16: Momentum reconstruction strategies in HADES. Left: Kick-Plane method. Center: Cubic Spline method. Right: Runge-Kutta Method.

Kick plane

The Kick-plane method assumes that the magnetic field influence on the particle trajectory can be reduced to a virtual plane where the passing through particle receives an angular deflection. Therefore, the particle's momentum can be obtained as a function of three variables: the deflection angle, and the initial azimuthal and polar angles at the interaction vertex. The parameters connecting these inputs with particles momenta are stored in tables and are previously obtained by simulation using the GEANT3 package, where a detailed parametrisation of the local values of the magnetic field has been implemented.

The historical reason of the implementation of this method was the initial configuration of the spectrometer, where the outer MDC modules were missing. Thus, the available tools were limited by the spectrometer's configuration and relied on simulation studies. However, this method has two important advantages. The first one is the computational speed because the momentum is tabulated. The latter, is the reduced information needed to provide a reasonable momentum estimation. On the other hand, the disadvantages of this implementation are the dependence of the momentum resolution on the generated parametrisation table and the assumption of a localised magnetic field which neglects bending outside the Kick-Plane region.

Spline

The Spline method relies on the cubic interpolation between hits in all

MDCs. Thus, besides a smooth trajectory, the first and second order derivatives at each point can be calculated. The path is divided in 50 equally spaced segments and the magnetic field strength is calculated for each point using the three dimensional field map. Afterwards, the momentum is determined as the mean values of the obtained momentum for each of the 50 points.

However, since the cubic spline does not reproduce the real trajectory, systematic deviation exist. To overcome these errors, deviations should be previously obtained through simulations and correctly parameterised, complicating the algorithm.

Runge-Kutta

Barely, the Runge-Kutta methods are iterative algorithms to solve differential equations. In case of trajectory and momentum determination, the differential equation of motion in a magnetic field is derived and solved. The numerical method requires several initial conditions, as a initial estimation of the momentum, that is provided by the Spline method, the polarity of the particle, its coordinates and slopes (first derivatives) provided by the segment fitter.

Once all ingredients are introduced in the algorithm, the iterative minimisation starts. As a result, the track parameters, as direction and momentum, arise from the most probable trajectory as well as its flight length and a quality criteria chi square, useful for further particle selection and identification.

Kalman-Filter

Thus far, all the above explained methods, do not regard the deviation from the ideal case, due to energy losses and multiple scattering processes. Therefore, the values of the fit quality are far away from the real case. A method to overcome this problem is being developed in HADES.

The Kalman filter is a very powerful fitting method that has found a very broad field of applications in science, finances, engineering, etc. It is a recursive method that starts from an initial non-accurate proposed solution given in a start point and improves it step by step at the same time that it is transported to the different points were the data were taken. In each step the covariance matrix of the solution is updated, taking into account the

transport equation to the following point, and it is improved with the new measurement. The new solution is obtained without needing the inversion of the full-space dimension matrix, becoming a very fast procedure. The Kalman filter is very useful for finding the track solution both in very complicated experimental setups and in inhomogeneous magnetic fields.

1.2.3.4 Particle Identification

The particle identification is performed in HADES in two different ways. The first one consists on hard cuts in several measured observables such as the velocity, the momentum, the energy loss in the drift chambers and TOF, the charge measured in the Pre-Shower and several quality magnitudes commented above, as the chi and the correlation with the Cherenkov detector. The cuts depend on the type of the particle and several of them depends on other parameters such as the momentum. In this Thesis, cuts are the method of choice for particle selection.

The other one is a Bayesian statistical method. It collects all the information from the detectors and provides a probability that these observables are compatible and consistent with the initial particle hypothesis.

2 Gaseous Ionisation Detectors

The measurement of non perceptible objects by our senses is always quite complicated and it is biased by our theoretical understanding of the structure of the object of study. Furthermore, its interpretation is truncated by the model that we try to fit to the measured data. However, this problem do not underlie only the imperceptible objects for our senses, as a correct interpretation of perceptible complicated systems and objects suffers the same problem. Moreover, our systematic simplification and subdivisions of the studied object shadows sometime the real relationship and interrelationship with regard to the environment. In that sense, the observation of objects at a very large or small scales, involves besides the appropriate tools for the measurement, a set of abstract ideas or theories about its structure and properties. Here, we assume the standard understanding of the structure of matter.

The interpretation of the microscopic world and its structure is only accessibly through the measurement of the tiny footprints left within a certain material. Usually, before accessing the information, an amplification of the signal must be performed. In order to achieve this aim, several techniques such as amplification electronics, multiplication of the signal induced by a external electrical field, chemical reactions or material properties which stays close to transition points are used. Then, the resulting signal is recorded and analysed.

This chapter is devoted to gaseous ionisation detectors. The interaction of radiation with matter and the main principles of detectors construction is analysed first, in Section 2.1. Next topic is the study of gaseous ionisation detectors in Section 2.2 and the methods and techniques used to measure the signals and the information that is enclosed there, in Section 2.2. Finally, the last topic is the Resistive Plate Chamber detector. The evolution of the detector trough the time and its physics is explained in Section 2.3.

2.1 Interaction of radiation with matter

This section explains the main mechanisms by which moving particles through matter interact and lose their energy within the media. This is a matter of fundamental importance because the detection of particles and the design of the detectors are closely bound to these interactions and the released energy within the detectors materials. Moreover, this is the theoretical background needed to interpret the measurements.

But before launching into the properties and interactions of particles with matter it is convenient to group the different families of particles according to the proposed by Glenn F. Knoll[41] shown in the Table 2.1.

Charged particles		Uncharged particles	
Heavy charged particles	←=	Neutrons	
Fast electrons	←=	Photons	

Table 2.1: Classification of particles according their interaction with matter.

This classification resumes four main groups of particles according to their interaction with the medium. The charged particles interact because of the electric charge with the medium electrons trough the Coulomb force. The distinction between heavy particles and electrons is motivated by the huge mass difference between them. The uncharged particles interaction is measured through conversion of neutrons in other heavy particles through elastic scattering or nuclear interaction and the photons through conversion into electrons.

2.1.1 Heavy charged particle interaction

The heavy fast charged particles interact through Coulomb forces with the electrons present within the medium. The energy transferred to the medium leads to ionisation or excitation of the atoms. The number of interactions and the total amount of transferred energy varies with the incident particle characteristics as its charge q , kinetic energy E^1 and velocity $\beta = v/c$, and the properties of the media as its density ρ or the

¹The use of E to define the kinetic energy is due to historical reasons, whereas E means the total energy in other parts of this Thesis.

atomic number/mass rate Z/A . Let's call total differential probability of interaction, or differential cross section, as a function of velocity and momenta $d\sigma(E; \beta)/dE$. Then, the number of collisions N_c within a certain distance δx and with momenta between E and $E + dE$ is

$$N_c = N_e \delta x \frac{d\sigma(E; \beta)}{dE} dE, \quad N_e = N_A \frac{Z}{A}, \quad (2.1)$$

where N_A is the Avogadro's number and N_e is the electron density². The collisions are equally distributed along δX . A more general expression can be derived from the differential cross section. Following [42], general moments $M_j(\beta)$ can be formulated as follows:

$$M_j(\beta) = N_e \delta x \int E^j \frac{d\sigma(E; \beta)}{dE} dE. \quad (2.2)$$

The M_0 moment is the previously defined N_c , M_1 is the mean energy loss in δx and $M_2 - M_1^2$ is the variance.

The M_1 moment or the mean energy loss in intermediate Z materials is well described by the Bethe-Bloch formula in the range of $0.1 \leq \beta\gamma \leq 1000$ as shown in the Fig. 2.1. These two limits are set by interactions which occurs below and over that range. At very slow incident velocities, it became similar to the velocity of the bound electrons in the atom and at very high energies radiation processes start to dominate. The equation itself can be expressed as a function of β , γ , the mean excitation energy I and the maximum energy that can be transferred to a free electron of an atom by a particle of mass m_i that is:

$$T_{max} = \frac{2m_e c^2 \beta^2 \gamma^2}{1 + 2\gamma \frac{m_e}{m_i} + \left(\frac{m_e}{m_i}\right)^2}. \quad (2.3)$$

Therefore, mixing all these ingredients and several constants the mean energy loss is:

$$-\left\langle \frac{dE}{dX} \right\rangle = K z^2 \frac{Z}{A\beta^2} \left\{ \frac{1}{2} \ln \left(\frac{2m_e c^2 \beta^2 \gamma^2 T_{max}}{I^2} \right) - \beta^2 - \frac{\delta}{2} \right\}, \quad (2.4)$$

² The N_e term can also be expressed as a function of the density of the medium, giving a dimension of electrons/cm³ instead electrons/g as in the former definition.

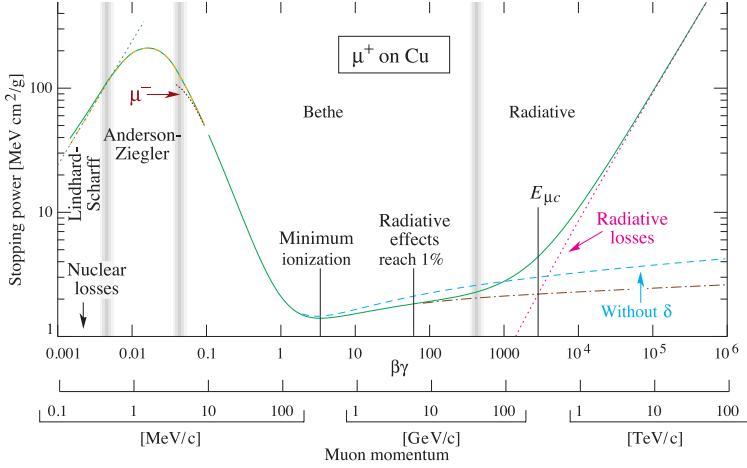


Figure 2.1: Energy loss of a μ^+ in Copper. The solid curve is the total stopping power. The dotted lines indicate several contributions and the result of the Bethe-Bloch formula with and without the density term. The validity range of the Bethe-Bloch formula 2.4 is between the vertical bars marked as "Bethe". Other radiation regions are also shown[42].

where $K = 4\pi N_A r_e^2 m_e c^2$ is a constant which contains among others already mentioned, the classical electron radius $r_e = e/4\pi\epsilon_0 m_e c^2$ and the electron mass m_e . The $\delta/2$ term is the medium density effect correction.

As the incident particle energy increases, the distant collision probability grows as $\ln(\beta\gamma)$ neglecting the polarisation of the media being necessary to introduce a correction as:

$$\frac{\delta}{2} = \ln\left(\frac{\hbar\omega_p}{I}\right) + \ln(\beta\gamma) - \frac{1}{2}. \quad (2.5)$$

where we call $\hbar\omega_p = \sqrt{4\pi N_e r_e^3 m_e c^2 / \alpha}$ the plasma energy of the medium and α is the fine structure constant.

The particles with $\beta\gamma \sim 3$ or around the minimum values are called minimum ionising particles or MIPs. Most of the cosmic muons can be considered as MIPs.

The formula 2.4 can be integrated to find the CSDA³ range R neglect-

³Continuous slowing down approximation

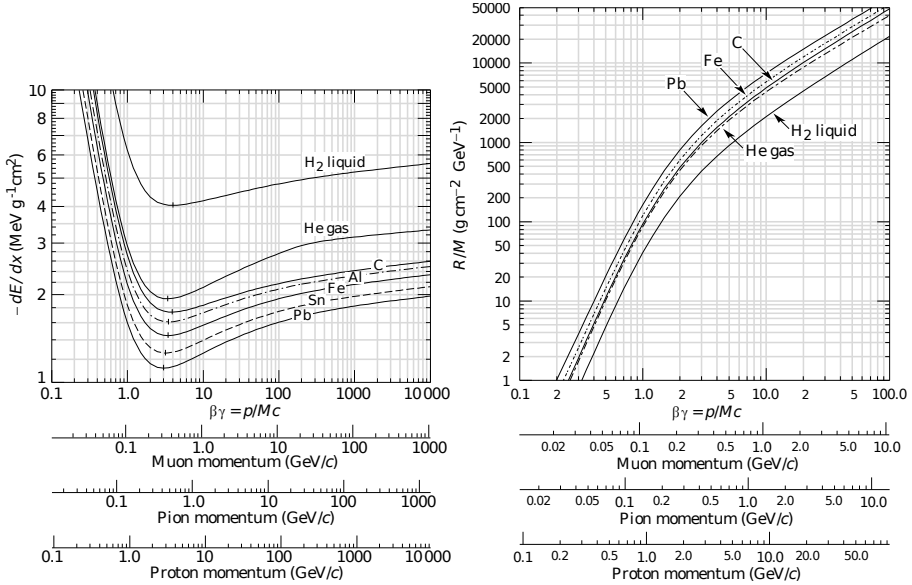


Figure 2.2: Left: Mean energy loss as a function of $\beta\gamma$ for several common materials. Right: Range of particles in several mediums accounting ionisation and atom excitation. [42].

ing radiative losses. The mean energy loss and the mean range for heavy ionising particles in several materials are shown in Fig.2.2. Notice the differences between the lightest and heavier materials. Besides the different Z/A factor, the mean excitation energy varies significantly with Z . Tabulated values for elements and most used compound materials can be find in [43].

However, as it is shown in the Section 2.1.3, in the case of thin materials the mean energy loss is not a good estimator, instead, others as the most probable lost should be used.

2.1.2 Electron and photon interaction

Whereas heavy charged particles loose mostly their energy by ionisation and atomic excitation in the range of intermediate energies, electrons above 10 MeV do it by Bremsstrahlung and photons above ~ 1 MeV do it by

e^+e^- pair creation. Both processes are closely related. Instead the mean energy loss is convenient to define to new variables. The radiation length X_0 is defined for electrons as the distance over which an electron losses $1/e$ of its energy and as a $\sim 7/9$ of the mean free path for pair production for photons. The mean free path, or attenuation length λ is defined as the distance at which remains an $1/e$ fraction of the total incident photons. Both variables are usually measured in g/cm^2 . Following [42], the radiation length can be obtained as:

$$X_0^{-1} = 4\alpha r_e^2 \frac{N_A}{A} \{ Z^2 [L_{rad} - f(Z)] + ZL'_{rad} \} , \quad (2.6)$$

where L_{rad} and L'_{rad} are the radiation logarithms[44] and $f(Z)$ is the Coulomb correction. Both values and the radiation length can be found in [44] and tabulated up to $Z=92$.

Besides bremsstrahlung, at low energies electrons loose most of their energy by other interactions with the media. The main processes such as ionisation (the most important), Moller scattering, Bhabha scattering and e^+ annihilation are shown in the Fig. 2.3. The energy at which energy loss by ionisation equals Bremsstrahlung is usually called critical energy.

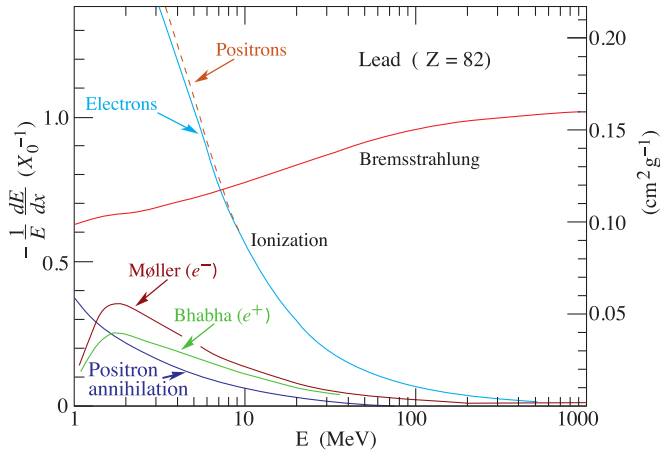


Figure 2.3: Fractional energy loss in lead for e^+ and e^- . The different processes which contribute to the energy loss are shown. [42].

Concerning photons, the most significant processes are the following: at low energies, corresponding to the ultraviolet region, the most important

contribution to the total energy loss is the photoelectric effect. In this process, an electron is ejected from the atom whereas the photon is absorbed by it. Its characteristic sharp spectra is due to the atomic levels structure. At intermediate energies, the Rayleigh and Compton scatterings dominates the energy loss. And finally the pair production region is reached. The photon mean free path in several materials is shown in the Fig. 2.4.

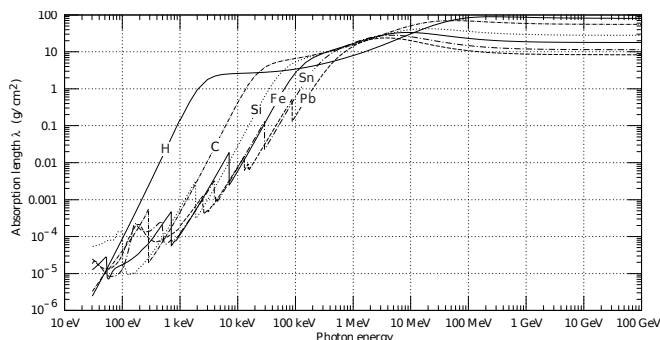


Figure 2.4: Photon mean free path, λ , for several media is shown.[42].

2.1.3 Energy losses in thin absorbers

Energy loss in thin absorbers was revised by Hans Bichsel in [45]. He pointed out:

The concept dE/dx representing the mean rate of energy loss in an absorber is used inappropriately in the description of the physics of most high energy particle detectors...The most probable energy loss Δp and the width w of $f(\Delta p)$ are more representative of $f(\Delta p)$ than the mean energy loss $\langle \Delta \rangle = x \cdot dE/dx$.

The mean energy loss, due to its large tails, is of complicated measurement. For this reason, another parametrisation should be used instead. The most probable energy loss can be described by the Landau-Vavilov-Bichsel (LVB) function[42]:

$$\Delta p = \xi \left(\ln \left(\frac{2mec^2 \beta^2 \gamma^2}{I} \right) + \ln \frac{\xi}{I} + 0.200 - \beta^2 - \delta \right), \quad (2.7)$$

where $\xi = KZx/2A\beta^2$ is a thickness-dependent factor. Despite the most probable energy loss is well described by the LVB function, in very thin mediums, the real distributions are wider than the highly skewed Landau width. This is shown in the figure 2.5. To overcome this problem a detailed explanation can be found in [45].

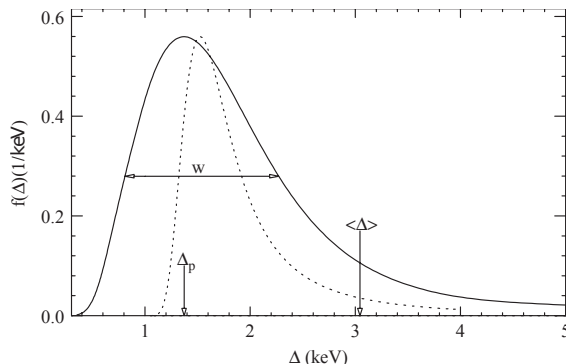


Figure 2.5: The energy deposit probability in a thin detector (1.2 cm filled with Ar) by an ionising particle with $\beta\gamma = 3.6$ is represented with a solid line. The dotted line shows the Landau function. The following parameters are shown: The most probable energy loss $\Delta_p(x; \beta\gamma)$, the FWHM $w(x; \beta\gamma)$ and the mean energy loss $\langle \Delta \rangle$. [45].

2.2 Physics and Measurements in Gaseous Ionisation Detectors

Gaseous ionisation detectors are one of the most widespread detector families in nuclear and particle physics. Moreover, the realm of nuclear physics began with the simplest gaseous detector: the Geiger-Müller counter. Those measurements of alpha particles permitted a separation from chemistry and the first atomic model formulation done by Lord Ernst Rutherford, becoming a new field itself.

The story continues turning around alpha radiation into probes to explore the atomic structure of matter. Available energies from natural radioactive sources became insufficient to penetrate the atomic barrier to explore

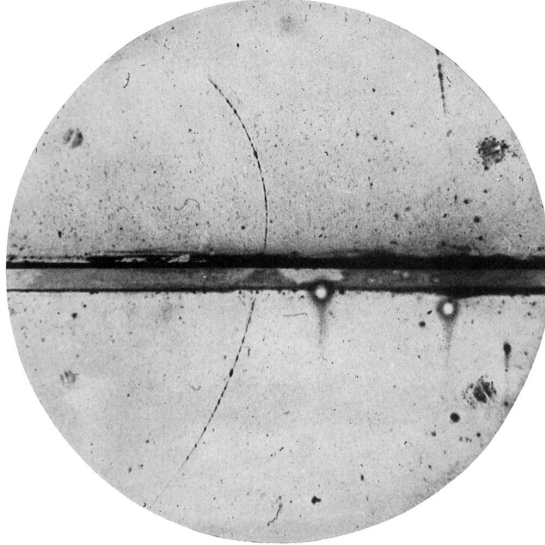


FIG. 1. A 63 million volt positron ($H\rho = 2.1 \times 10^6$ gauss-cm) passing through a 6 mm lead plate and emerging as a 23 million volt positron ($H\rho = 7.5 \times 10^4$ gauss-cm). The length of this latter path is at least ten times greater than the possible length of a proton path of this curvature.

Figure 2.6: An positron track photographed by C.D. Anderson (its discoverer). The horizontal line is a lead plate. Thus, the bending within the magnetic field of the positron is different before and after the absorber. The picture has been taken from [46].

the nucleus motivating the development of accelerators and new detectors. In parallel, other natural sources of radiation as cosmic rays were studied, leading to the discovery of several fundamental particles such as the positron, the muon and the π meson together with the strange particles.

For a long time, cosmic ray radiation was the only high energy particle source. Due to its relatively low rate (around $2 \cdot 10^2$ Hz/m²) and the existed limitation of registering events electronically the most used detectors where the Geiger-Müller and the cloud chambers invented by C.T.R Wilson and others as electroscopes, photo-emulsions and scintillating materials. The physics of the cloud chambers differs from the standard gaseous detectors as it work using another principle. The gas within the chamber is in a supersaturated state. Ionised particles act as condensation nuclei. These ions form a mist along the path of a particle passing through the chamber. An example of the mist caused by a positron is shown in Fig. 2.6.

Since Geiger-Müller counter, the preferred detectors geometry was the cylindrical. The paradigm shift came with G. Charpak and its Multiwire Proportional Counter (or Chamber) MWPC[47]. He proposed to build chambers made of planes of independent wires placed between two plane electrodes, improving the idea of proportional counters with wires connected in parallel. In the MWPC, each wire was an independent detector itself connected to a preamplification circuit. Wire separation of 0.1 mm where possible. Moreover, the design had the capability to couple more layers at different angles to improve the measurements. At the end of the article [47] the authors pointed out:

These observations give us confidence that this type of instrument deserves a very detailed study since it can in some respects replace classical wire chambers or hodoscopes, or be a useful complementary tool, for instance as a fast decision-making chamber to trigger.

Indeed, besides studying the MWPC in detail, the constructional ideas spread to other detectors. However, to understand better their characteristics, the physics of the avalanche in gases is important and it will be studied in the next section.

2.2.1 Physics of the avalanche

The general operating principles of gaseous detectors are the following:

- The gas within the detector ionise by interaction with charged particles passing through.
- The unbound electrons and ions start to drift under the influence of the applied electrical field to the electrodes.
- A induced current is produced in the electrodes and it can be registered by the acquisition equipment.
- The process stops once all the charges have been absorbed.

This process will depend on the applied electric field, the gas mixture, the incident radiation and the geometry of the detector. Regarding the electric field, its presence is mandatory because the recombination in the

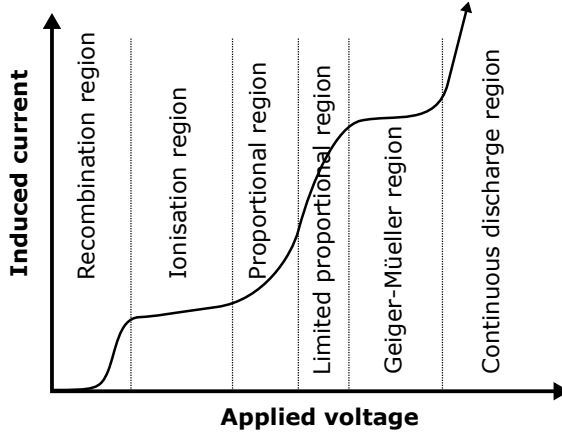


Figure 2.7: Gas filled detectors regions of operation as a function of the applied electrical field.

gas and the need to collect the induced signal. In the case the ions and electrons were not accelerated to the electrodes they would return to the equilibrium, i.e. they will recombine, and the energy left will contribute only to the excitation. On the other hand, during acceleration, electrons and ions can get enough energy to produce more ionisations in the gas. The number of produced secondary ionisation is related with the mean free path, λ , and the energy transferred from the external field. The number of produced secondary ionisations divided by the initial number caused by radiation, is defined as the gain of the gas, which depends on the applied electrical field. The number of the produced pair electron-ion as a function of the voltage, determine the working regime of the detector. The most important regions are shown in the Fig.2.8 and are namely: recombination, ionisation, proportional, limited proportional, Geiger-Müller and continuous discharge regions.

The main properties of these regions are listed below:

- *Recombination region:* The applied electrical field is not enough to collect all the produced e^- /ion pairs and some of them are lost due to recombination, excitation, absorption.
- *Ionisation region:* The potential is enough to transport and collect all the e^- /Ion pairs, but there is no multiplication, i.e. there is not

enough potential to generate an avalanche.

- *Proportional region*: The avalanche grows proportionally to the deposited energy. The induced signal is proportional to the number of primary ionisations.
- *Limited proportional region*: The avalanche grows proportionally but not linearly as a function of the applied potential because the electrical field created by avalanche starts to screen the applied potential.
- *Geiger-Mueller region*: The induced signal is no more related with the initial ionisation in the gas. The screening of the applied electrical field by the generated within the avalanche makes the process self-limited.
- *Continuous discharge region*: Once the avalanche process starts, it becomes self-sustained.

It is thus important to select properly the work region regarding the measured variable. Ionisation and proportional regions are suitable to perform energy loss and position measurements whereas the limited proportional and the Geiger-Müller regions are also suitable for timing measurements.

If we want to measure the currents created in a gas the easiest way is to confine it between two electrodes with an applied potential between them. That was exactly what J. S. Townsend did in “The theory of ionization of gases by collision” in 1910[48]. He measured systematically several gases applying an electrical field between two electrodes and releasing electrons at the cathode. He formulated the fractional increase of electron number n in a dx width as:

$$\frac{dn}{n} = \alpha dx , \quad (2.8)$$

where α is the first Townsend coefficient or the inverse of the mean free path between two collisions. If we consider that the field is applied between two parallel electrodes and $\alpha = cte$, the avalanche growth will be:

$$N(x) = N_0 e^{\int \alpha(x) \cdot dx} . \quad (2.9)$$

Regarding the evolution with time of the avalanche, the number of electrons n_e and positive ions e_p in the swarm can be formulated as following[49]:

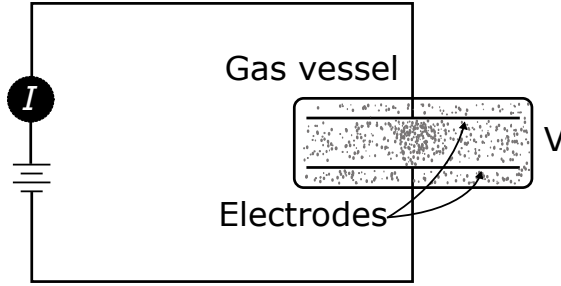


Figure 2.8: Schematic set up for measurement of induced currents in gases.

$$\frac{\partial n_e(x, y, z, t)}{\partial t} = (\alpha - \eta)n_e v_e - \nabla \cdot (n_e v_e) + D_e \nabla^2 n_e, \quad (2.10)$$

$$\frac{\partial n_p(x, y, z, t)}{\partial t} = (\alpha - \eta)n_p v_p - \nabla \cdot (n_p v_p) + D_p \nabla^2 n_p, \quad (2.11)$$

where η is the attachment coefficient, $v_{e/p}$ is the drift velocity of electrons/positive ions and $D_{e/p}$ is the corresponding diffusion coefficient.

Following the definition for attachment given by Davies and Evans [49] as "the probability of attachment per unit distance travelled by an electron in the direction of the field", electrons may be attached to neutral molecules forming negative ions. It is of special importance "in electronegative gases where the potential energy of the negative ion is smaller than of the atom or molecule in its normal state"[49].

For electrons, assuming α and η are constant and neglecting the diffusion contribution, the solution is:

$$n_e(t) = n_0 e^{(\alpha - \eta)v_e t}. \quad (2.12)$$

Thus, the avalanche grows exponentially in time. However, the exponential amplification is disturbed once the own electrical field of the avalanche became comparable to the applied one. At this point, the effective field has different values along the avalanche. This effect is called space-charge [50] and is of special importance to understand the avalanche behaviour in RPCs.

Besides the normal propagation of the avalanches exists another phenomena called streamer, characterised by a fast increase of the charge.

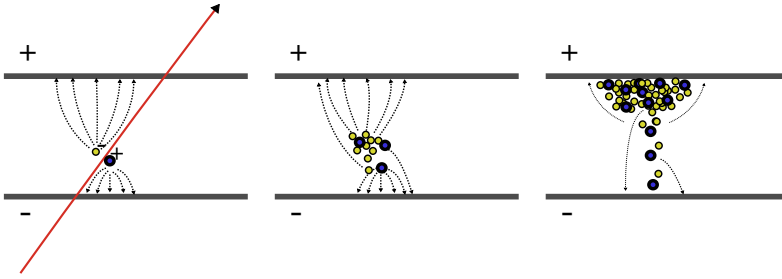


Figure 2.9: Evolution of an avalanche in a parallel electrodes geometry detector. From left to right: First a primary ionisation is produced, next, the electrons start to drift to the anode and the ions to the cathode. Finally, the electrons arrive to the anode whereas ions drift from the anode to the cathode.

The origin of these avalanches, closely related with the space charge effect, can be twofold[51]: from one side, ultraviolet photons radiated from the avalanche may ionise molecules outside the avalanche feeding again the avalanche growth. To minimise the probability of ionisations coming from the UV photons, is usually added a gas to the mixture called quencher. From the other, electrons created at the tip are subject to start new avalanches as they are under the influence of an enhanced electrical field because of the space-charge effect.

The drift velocity for electrons is orders of magnitude faster than ions one. For that reason we can split the induced charge in two terms: the q_{prompt} and $q_{induced}$. Moreover, mainly the ions will be produced close to the anode because of the multiplication of the electron swarm, and will drift towards the cathode. The avalanche and drift of electrons and ions in two different configurations detector are shown in the Fig. 2.9 and Fig. 2.10.

The induced current in the electrodes by the avalanche can be calculated using the Ramo theorem[53] introduced in 1939:

$$i = E_v e v \quad (2.13)$$

where i is the instantaneous current received by the given electrode due to a single electron's motion, e is the charge on the electron, v is its instantaneous velocity, and E_v , is the component in the direction v of that electric field which would

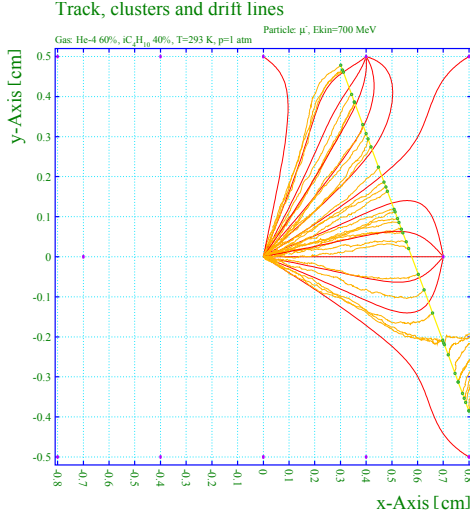


Figure 2.10: Simulation of a muon signal in an MDC cell. Primary ionisations (green), Electron drift lines (orange) and drift path of ions from the anode to the cathodes (red). The picture has been taken from [52].

exist at the electron's instantaneous position under the following circumstances: electron removed, given electrode raised to unit potential, all other conductors grounded. The equation involves the usual assumptions that induced currents due to magnetic effects are negligible and that the electrostatic field propagates instantaneously.

The induced charges q_{prompt} and $q_{induced}$ in the electrodes is the integral of the induced current starting at time t_0 and finishing at t_e/p :

$$q_{prompt} = \int_{t_0}^{t_e} E_v e v_e dt, \quad (2.14)$$

and therefore the total induced charge is:

$$q_{induced} = q_{prompt} + \int_{t_0}^{t_p} E_v e v_p dt. \quad (2.15)$$

2.3 Historical approach to Resistive Plate Chambers

Parallel Plate geometry has the advantage of a constant electrical field in the gas contained between two electrodes. The precursors of the RPC technology are the Parallel Plate Spark Chambers. In 1956 M.V Babykin, A.G. Plakhov, Y.F. Skachkov, V.V. Shapkin, E.K. Zavoijskiy and G.E. Smolkin, aiming to improve the time resolution of a spark chamber, reduced the distance between the electrodes to 0.2mm and operated the detector at 13 atm with a mixture of Argon and Ether. They measured in coincidence through a electro-optical readout and achieved a time resolution of 100 ps. [54]⁴. To overcome some constructional limitations as a low counting rate and a small size, in 1970, V.V. Parkhomchuck, Y. N. Pestov and N.V. Petrovikh [55] improved the design substantially by introducing a high resistive material⁵ in order to limit the sparks progress in the detector. The achieved time resolution was around 25 ps and the efficiency about 96% operating the detector at 12 bar with a gas gap of 0.1 mm[56].

Thus far, we have described the Parallel Plate Spark Chambers and a special Pestov counter, though the first Resistive Plate Chamber was introduced by R. Santonico and R. Cardarelli in 1981[57]. Originally they called the new detector Resistive Plate Counter, however it became more popular the denomination Chamber over time among authors. Their goal was to extend the working principle of the Pestov Counter:

The detector presented in this paper, which will be called "Resistive Plate Counter" (RPC) is based on essentially the same principle as that recently developed by Pestov and Fedotovitch. Nevertheless the drastic simplifications introduced in its realization, such as the absence of high pressure gas, the low requirements of mechanical precision, and the use of plastic materials instead of glass, makes it of potential interest in a

⁴The author was not able to find neither the originals or translated version of the original publications. The information was retrieved from a review of the state of the art of ionising particles detectors published in 1963. However, the citation is: M. Babykin et al. Parallel-plate spark counters for measuring short time intervals. Journal of Nuclear Energy, 4. p345, 1954

⁵semiconductive glass, called the Pestov glass, had a resistivity between 2×10^8 and $4 \times 10^9 \Omega \text{cm}$.

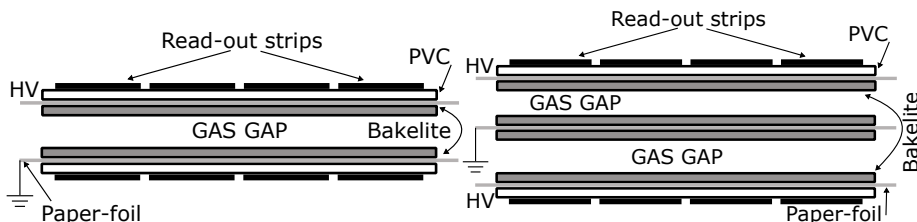


Figure 2.11: Left: Schematic cross section of the first built RPC by R.Santonico and R.Cardarelli showing the different materials, read-out and dimensions. Right: A two gap arrangement, with shared ground electrode in the center.

different and possibly wider range of applications. In particular it could replace with great economic advantages plastic scintillators, whenever large detecting areas are needed under not exceedingly high fluxes of particles.

Their detector achieved a 1.2 ns^6 time resolution and 97% of efficiency operating at atmospheric gas pressure, a gas gap of 1.5 mm and an 60 kV/cm applied potential. The design was easily scalable, cheap compared to other detectors offering similar performances e.g. plastic scintillators. As a resistive material was used bakelite, a phenolic resin with resistivity if the order of 10^{10} - $10^{11} \text{ } \Omega\text{-cm}$. The gas mixture used was 50% Argon and 50% iso-butane[57]. The schematic cross section of the detector is shown in the Fig.2.11 in two configurations: single gap RPC and two RPC sharing the same ground electrode. The detector was operated in the streamer mode being thus the counting rate limited. On the other hand, the read-out scheme could be simplified as no external amplification was needed, contrary to what happens in detectors operated in the avalanche mode.

The next remarkable step was done by M.C.S. Williams's group introducing the concept of the multigap RPC[58]. Their goal was to achieve a time resolution of a narrow gap rpc (2-3 mm) together with the efficiency and rate capability of a wide gap rpc (5-9 mm) operated in avalanche mode. The design solution was a three gap geometry with four resistive layers, two of them protecting the electrodes and the other two defining

⁶The time resolution was given at the F.W.H.M, which corresponds in a Gaussian distribution to $F.W.H.M. = 2\sqrt{2\ln 2}\sigma$, thus $\sigma_t = 510 \text{ ps}$.

the gaps as shown in the Fig. 2.12. The voltage was applied in the external electrodes remaining the internal resistive Bakelite layers electrically floating. Besides a new constructional solution, their research also was focused on find a gas mixture to overcome the low efficiency of narrow gap RPC filled with standard Argon quenched mixtures. They achieve to operate in avalanche mode, something critical in terms of counting rate, with quenched Freon gas mixtures obtaining same efficiencies than Argon based 8 mm gap RPC only with a 2 mm gap RPC[59].

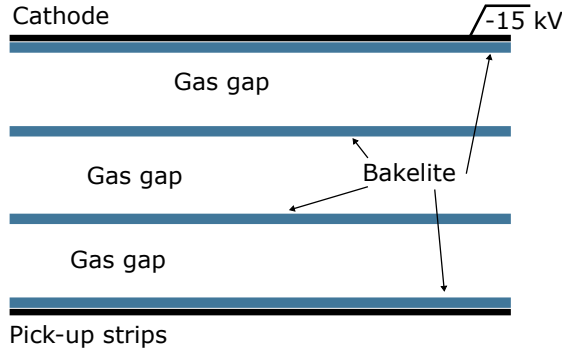


Figure 2.12: Schematic cross section of the multigap RPC proposed by M.C.S. Williams’ group.

The last sub-type, the timing RPCs, were introduced by P. Fonte, A. Smirnitski and M.C.S. Williams in 2000[60]. They built a detector capable of provide a timing accuracy of 120 ps sigma and a efficiency about 98% for MIPS. The design consisted of four narrow gaps of 0.3 mm each, gass plates having a resistivity around $10^{12} \Omega\text{cm}$ and metallised ceramics as electrodes. The read-out was done amplifying the signals with a low rise time current amplifier. The gas mixture was a Freon based, with isobutane as a quencher and Sulfur hexafluoride (SF_6), as it was observed previously its streamers suppression capability [61].

Other important achievements are noteworthy to mention, regarding applications of the RPC technology or new studies in materials:

- The first one, is a 21 ps device, made of 24 gas gaps with a width of $160 \mu\text{m}$ [62]. The achieved resolution was similar to the Pestov’s counter...38 years later.

- The next remarkable R&D development regards RPC based calorimeters. Several groups are working in these devices, the Digital and Semi-Digital Hadronic Calorimeters⁷. The improvement in integration the Front-End electronics allowed to build detectors with 500 thousand channels distributed in 50 planes of 10.000 pads each of $1 \times 1 \text{ cm}^2$ [63][64].
- Important steps toward RPC based systems with high position resolution were reported in the RPC2012 Workshop on Resistive Plate chambers by P. Fonte[65]. They achieved to build a tracking-ToF module with an position accuracy below $50 \mu\text{m}$ combined with a time resolution of about 80 ps. The combination of both, the best tracking capabilities and time of flight measurements in a single detector paves the way of substantial improvement in particle tracking and identification, as timing information can facilitate a better cluster finder and the time measurement through several planes can be substantially improved, once the track is identified.

Among other advances we can find another proposed detector along the same line with tracking RPCs, within the TRASGO project. Of course, the aimed position resolution is of the order of cm, nevertheless it deepens in the time with tracking concept[66]. Within this project it was developed the TimTrack algorithm, discussed in the Chapter 5, which is a extended Least Squares Method which takes advantage of detectors offering both time and position information[67].

The application of the RPC technology out of high energy physic experiments means the field has come of age. A good example of this, is the research done by A. Blanco at LIP, who used RPCs to build a small PET prototype with sub-millimetre resolution at a low cost[51].

Finally, it is important to highlight the R&D dedicated to new materials capable to extend the operational rate limit done by M. Morales at Lab-CAF USC and CSIC Madrid. Besides develop and test several encouraging materials for the future high rate RPC, he has done a deep analysis and measurement of the electrical properties of the most common materials used to build the detectors and he pointed out the importance not only of

⁷DHCal and SDHCal respectively

the resistivity of the material, as also the permittivity and the conduction mechanisms of these materials[68].

3 HADES RPC-ToF Wall

The development of the HADES RPC TOF wall involved in this endeavour universities and research institutes from four European countries. A joint effort was needed to achieve the goals of this project.

Is noteworthy to mention that, to date, four PhD. Thesis were already defended. Several aspects as design, front end electronics, software and performance tests are explain in detail by the authors who where involved in the R&D and test phases of the detector[15][69][70][71].

The first section of this chapter is devoted to the building and design goals of the HADES RPC ToF wall. Both, the physical and building constraints set by the physical program and the design of the spectrometer, where the newly developed technology replaced a low granularity scintillator wall at low angles. The next section deals with the proposed design solution, from the point of view of geometry, front end electronics and acquisition. Also, in the same section is done a review of the state of art of timing RPC detectors used in other experiments as ALICE, FOPI, HARP or STAR. The latter section of this chapter shows the possible implementation of a digitiser.

3.1 RPC TOF wall goals

The encouraging performance of the first timing RPC detectors [60] and the growing expectations the RPC technology offered for future experiments, led the HADES collaboration to choose them, among other options, to replace the low granularity scintillator wall at low angles of the spectrometer. Other reason was the affordable price.

The physical program and the design of the HADES spectrometer itself set strict conditions on the design. The most relevant of them are listed below:

- Total area around 8 m^2 , with trapezoidal shape and capable of being

attached to the Pre-Shower detectors frame with maximum acceptance.

- Efficiency above 95% for single hits.
- Time resolution below 100 ps for minimum ionising particles, in order to provide a good separation between $e^{+/-}$, $\pi^{+/-}$ and K^+ .
- Rate capability up to 1 kHz/cm² in the innermost part.
- High granularity and maximum hit loss probability below 20% for the central collisions of the heaviest systems.
- Small probability of production of secondary particles which could contaminate the measurement of the detectors placed downstream the RPC.

The occupancy and efficiency requirements limited the design of the RPC detector. To meet occupancy requirement the read out strips were displaced in a three column structure. To avoid the crosstalk between neighbouring cells, observed in previous experiences[72], a proper electrical insulation was required. On the other hand, to reach full efficiency, a two layer design was needed to fill all the uncovered regions between insulated strips and meet full geometrical acceptance at low angles.

3.2 Design, geometry, FEE and acquisition of the RPC TOF wall

The final design of the RPC ToF wall was done in several steps. Before deciding the final arrangement of the six sectors, it was decided to use a longitudinal cell shapes. Each cell is a full detector itself, packed in an aluminium box to electrically insulate it from external high frequency signals induced by neighbouring cells and to avoid propagation to the neighbours the signals produced within it. Inside the aluminium box, as shown in the Fig. 3.1, the main components of the basic structure are shown. Barely, it is a four gap design, each gap of 0.27 mm, defined with PEEK monofilaments¹. As resistive material are used two Soda Lime Silicate glass (more

¹PEEK is the acronym for polyether ether ketone a sort of organic polymer thermoplastics.

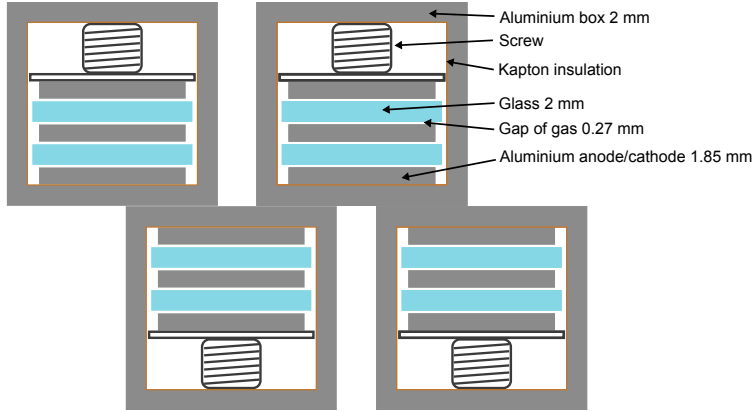


Figure 3.1: The HADES RPC cells cross section picture showing the main materials composing the internal structure

known as float glass) floating electrodes and three aluminium electrodes which serve both to generate an electric field inside the gas gap and to transport the signal from the place it is induced to the output[73]. The gas inside the RPC is composed by 90% Freon 10% Sulfur Hexafluoride ($0.90 \text{ C}_2\text{H}_2\text{F}_4 + 0.10 \text{ SF}_6$). This design showed previously an encouraging performance: time resolution around 50 ps sigma and a position resolution of 1.2 cm sigma while efficiency was close to 100% [74]. The geometrical acceptance of the final design and the size of one sector are shown in the Fig. 3.2.

The first prototype was done to test the concept. It showed a resolution well below 100 ps[75] and a very low cross talk level, something of the utmost importance in high multiplicity events and . This practically imperceptible level was a warranty of a clean measurement, as the high frequency signal travelling along the cell, if not isolated, can induce signals in the closest neighbours or even in the whole detector. The final shape of each sector was previously defined by the keep-in volume of the spectrometer between the 4th MDC plane and the Pre-Shower detector. The two layer with three column structure of each sector is shown in the Fig. 3.3a. The two partially overlapped layers increase efficiency and resolution. Within each column 32 cells with growing width and height in order to provide the same dose to all of them, as shown in the Fig. 3.3b.

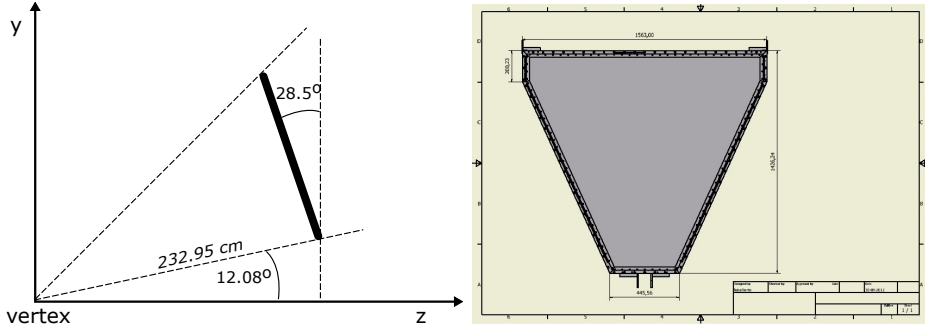


Figure 3.2: Left: Geometric acceptance at the RPC in the sector reference system, with origin in the target. Right: Dimensions of a RPC sector in its own reference system (module ref. sys.).

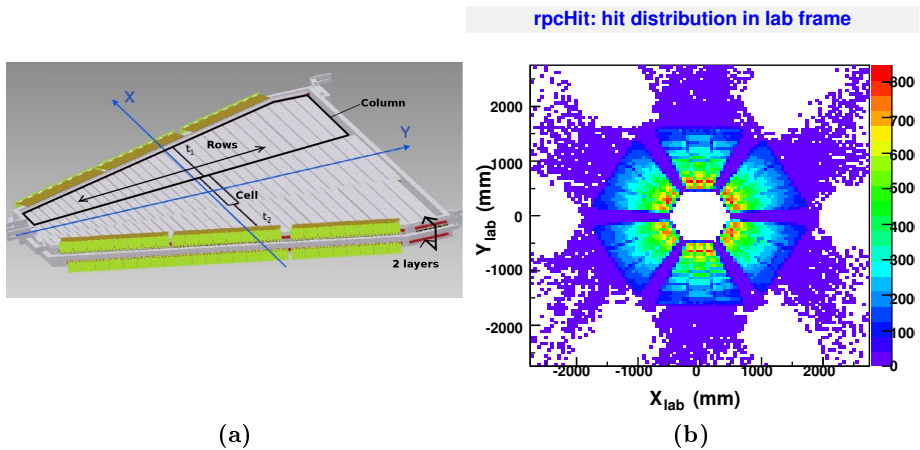


Figure 3.3: a) A RPC sector showing its internal structure and the Module reference system of the detector. b) Example of the hit distribution over a RPC sector in Au+Au collisions.

The existing overlap between both layers, allows also to estimate the intrinsic time and spatial resolutions. As shown in the Fig. 3.4, each cell shares part of its surface with two cells from the other layer. This surface, covered by two cells varies along the radial y coordinate. Moreover, this arrangement facilitate calibration and synchronisation of the detector. All

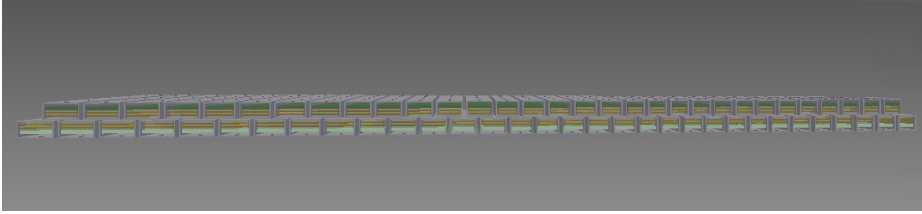


Figure 3.4: The overlapped structure of the RPC detector. Measuring the same particle at two overlapped cells allow to evaluate the intrinsic resolution of the cells. Moreover, this structure facilitate synchronisation and increase the efficiency.



Figure 3.5: The HADES RPC Front End Electronics. Left: The four channels DBO (Daughter board). Right: The 32 channels MBO (Mother Board).

the used methods are explained in detail in the Sections 4.1 and 4.2

The design of the cell sizes was thought to maximise acceptance while keeping the occupancy almost constant regardless of the cell position and size. A too high segmentation would increase dead region and a non optimised cell arrangement would increase efficiency losses due to double hits. The minimum number of cells to achieve a 20% occupancy was obtained from simulation of central Au+Au collisions at 1.5 A GeV. Simulations showed 30 particles expected over each sector, thus the minimum number of cells can be derived as following: $N_{min} = 6_{sectors} \times 30/0.2 = 900$. The considerations about the geometrical design and results of occupancy and expected rates can be found in [15].

The Front End Electronics, FEE, used to amplify, digitalise and transport the signal is implemented in a two board scheme: the DBO (Daugh-

ter BOard) and the MBO (Mother BOard); both are shown in the Fig.3.5. Each DBO has 4 input channels. First, the incoming signal is pre-amplified with a 1-2 Ghz bandwidth fast amplifier. Then, signals are treated twofold: from one side the signal is send to a dual discriminator with a constant threshold value and the other perform a charge measurement integrating the signal with an operational amplifier through a Charge to Width (QtoW) algorithm. Both signals are recombined in the output in a single LVDS signal carrying both the time and charge measurement[69]. The TOF and charge measurements are codified in the following way: the start of the LVDS pulse correspond to the time and its width is the charge.

The DBO is connected to the 32-channel MBO, which can house 8 DBO. One of the channels is used for synchronisations purposes, thus, 31 channels are available for time measurement. This board have five main functionalities[70]:

1. Transport the signals from the DBOs to the acquisition.
2. Provide a combination of the 32 multiplicity signals for the low-level trigger signal.
3. Set the programmable thresholds voltages for the time and charge measurements through digital to analogue converters.
4. Distribute the test signals to the DBOs.
5. Generate a low rippled voltage required by the DBO.

Besides the DBO and the MBO, the full electronic chain includes the TRB board, which has been introduced in the Section 1.1.8. As each cell has a two side readout, both times and charges are codified and stored in units of TDC bins. Thus, before recovering the time of flight of the particle and the position, the stored data are unpacked and calibrated. Both measurements are labelled with *left* and *right* referred to the RPC cell centre. Each time $t_k (k = left/right)$ is a sum of these contributions:

$$t_k = t_{\mathcal{O}} + t_{ks} + t_{k0} + t_q(Q) + t_x(x) \quad (3.1)$$

where $t_{\mathcal{O}}$ is the time of flight of the incident particle, t_{ks} is the time the induced signal propagated through the electrode from the interaction

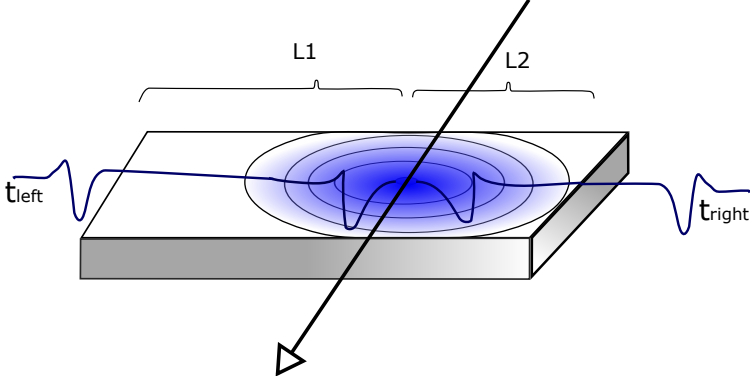


Figure 3.6: Representation of several contributions to the measured time by an RPC cell: the particle time of flight t_{ϕ} , the propagation of the signal through the electrode t_{k_s} and a constant offset t_{r_0} .

point x_{RPC} to the FEE, t_{k_0} is a constant for each channel where several contributions are combined as the cable lengths or the delay in the FEE, $t_q(Q)$ is the correction term dependent on the charge of the avalanche. The latter contribution is twofold: from one side, it has jitter due to electronic response of the FEE components to the signal size and rise time and from the other, simulations suggest the influence of the avalanche size in the time the induced signals crosses the FEE threshold value[76]. The different contributions of the time measurement for a better understanding are shown in Fig. 3.6.

It is useful to consider the half sum $\Sigma T = t_l + t_r$ and the half difference $\Delta T = t_l - t_r$ of the time measured at both sides of a cell of expression 3.1. Considering a null attenuation of the signal and the same response from electronics:

$$\Sigma T = 2t_{\phi} + (t_{l_s} + t_{r_s}) + (t_{l_0} + t_{r_0}) + 2t_q(Q) \quad (3.2)$$

$$\Delta T = (t_{l_s} - t_{r_s}) + (t_{l_0} - t_{r_0}). \quad (3.3)$$

The terms grouped in brackets can be expressed as a function of the cell length L , the signal velocity in the electrode v_s and the coordinates of the hit position x_{RPC} and the both ends x_{left} and x_{right} . Neglecting the contribution of the y_{RPC} coordinate, the term $(t_{l_s} + t_{r_s}) = 2L/v_s = \tau$, that we may call the time length of the cell, is a constant which can be

included in the constant global offset term $t_0_{TOF} = (t_{l0} + t_{r0}) + \tau$. The $(t_{l0} - t_{r0})$ can be included in a global position offset t_0_X . Thus, keeping in mind that $t_{ks} = |x_{left/right} - x_{RPC}|/v_s$, and neglecting calibration and correction parameters, the t_{RPC} and x_{RPC} can be expressed as a linear combination of the registered left and right times as follows:

$$t_{RPC} = \frac{1}{2} (t_{left} + t_{right}) , \quad (3.4)$$

$$x_{RPC} = \frac{1}{2} (t_{left} - t_{right}) v_s . \quad (3.5)$$

3.2.1 RPC software design

The software dedicated to perform the calibration of the data and transform them from a digital time measurement to natural variables in ns and mm is integrated in HYDRA. The data are sorted as a function of the level of the analysis:

- The unpacked data coming from the FEE is called RAW data.
- The CAL data stores the data corrected by constant offsets and converted to ns.
- The data with times corrected by charge and position expressed in length units is called HIT.

The algorithms which perform the unpacking, calibration and hit finder tasks are called as *hrpcunpacker*, *hrpccalibrator* and *hrpchitf* following the HYDRA standard nomenclature[34]. Furthermore, there is a higher level data and analysis called CLUSTER, done by the *hrpcclusterf* task which merge the hits of overlapped cells in one cluster with a consequent improve in resolution. Further and more detailed analysis of the RPC software structure, including the parameter container management or details about the unpacking task, can be found in [71].

The picture shown in the Fig. 3.6 sometimes is distorted by the presence of more than one particle in a narrow time interval. For example if two particles impact in a certain cell in positions x_1 and x_2 at a time t_1 and t_2 there are three main possibilities considering $t_1 < t_2$ and the signal propagation time of the first particle t_{s1} :

- The first and second particles are measured properly. This happens if the second particle arrives once the collection time of the first particle is already finished. $t_2 - t_1 = \delta t_{1,2} > t_{int} \sim 50$ ns.
- The second particle arrival time allows a correct time readout of the first whereas the charge measurement is distorted. In this case the second particle is completely lost. $t_{s1} < \delta t_{1,2} < t_{int}$
- The second particle arrival time shadows the propagation of the first signal and both measurements are lost from the point of view of the standard algorithm. $\delta t_{1,2} < t_{s1}$

An algorithm to recover the third case is shown in the Section 4.4.

3.2.2 The state of art of time of flight RPC based detectors

ALICE

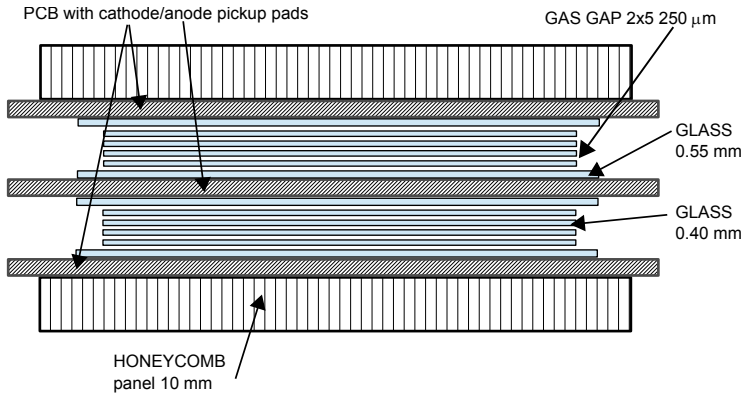


Figure 3.7: Schematic cross section of the RPC installed at ALICE.

The ALICE spectrometer is located at LHC[77]. The Time of Flight System was designed to perform charged particle identification in the momentum range from 0.5 to a few GeV and at a maximum rate of 50 Hz/cm^2 [78]. The detector covers a total area of $\sim 160 \text{ m}^2$ and is segmented in ~ 160000 readout pads of $2.5 \times 3.7 \text{ cm}^2$ each in order to keep the occupancy below 15%. It covers the polar region $|\theta - 90^\circ| < 45^\circ$ and have a full azimuthal acceptance because of its cylindrical shape[79].

The basic detector element is the double-stack Multigap Resistive Plate Chamber. Each stack has 5 gaps of 250 μm each, defined by fishing lines. The resistive material is soda-lime glass of 400 μm and 550 μ thickness. The former is electrically floating and the latter, facing the read-out PCB is painted with a resistive coating used to apply the voltage. The whole structure is embedded in 10 mm thick honeycomb panel. A schematic cross section of the detector can be found in Fig. 3.7. The RPC was initially operating with a gas mixture of 90% Freon, 5% Isobutane and 5% SF₆, replaced later by 93% Freon 7% SF₆ as reported in [80]. The total applied voltage is 13 kV, (+6.5 kV,-6.5 kV) with a dark current at the nA/MRPC level. [79].

The reported detector performance from the commissioning of the modules, cosmics and beam data show a intrinsic time resolution of 50 ps sigma with a RMS of 5 ps. The intrinsic efficiency was above 99% starting from 12.0 kV.[79]. The whole system time resolution with cosmic ray was around 112 ps sigma. However, the authors claim that there was not enough statistics to perform a single-channel analysis and corrections are introduced using overall values. The efficiency was obtained through Monte-Carlo and the declared value was 97%[81].

Regarding beam data, in [80], the efficiency used to match MC simulations and real data increased to 98% and the time resolution for selected pions with $0.95 < p < 1.05 \text{ GeV}/c$ ($\beta\gamma \sim 7$) was 86 ps sigma, well above the ionisation minimum.

FOPI

The FOPI spectrometer is located at the SIS accelerator of GSI[83]. The Time of Flight barrel has as its main goal provide kaon identification up to 1 GeV/c in heavy ion collisions at 2 AGeV. The expected rate at the ToF barrel is around 25-50 Hz/cm²[82]. To cover the surface of 5 m², the detector is split in 150 modules of $4.6 \times 90 \text{ cm}^2$, each one with 16 strips read-out at both sides. Thus the total amount of channels is of 4800. The strip width is 1.64 mm and the separation between them is 0.9 mm. The detector uses a 2×4 gap configuration, defined by 220 μm fishing line. The anode is placed in between both stacks. As a resistive material is used glass of 1.1 and 0.5 mm width placed alternately. The

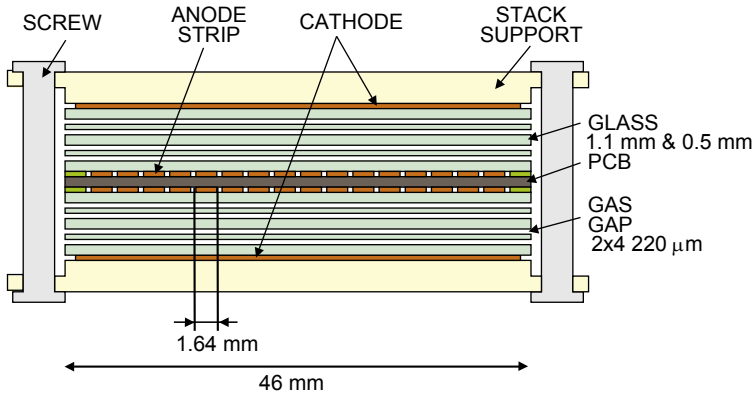


Figure 3.8: Schematic cross section of the RPC installed at FOPI. The figure has been adapted from [82].

high voltage is applied through copper electrodes attached to the external glass plates[84]. A schematic cross section of the detector can be found in Fig. 3.8. The gas mixture used by the FOPI RPC barrel was initially 85.1/4.3/10.6 (Freon/Isobutane/SF6), later changed to 80/5/15, in order to extend the streamer free region adding more SF6[61].

The particularity of the design is its strip configuration. Once an avalanche induces a current in the electrode, the probability that signal, propagates through the neighbouring strips can be measured by means of the number of fired strips per hit (cluster size). In FOPI, during the tests, the reported average cluster size was below 1.5-3.0 depending on the applied voltage[84], while in Ni+Ni beam data, the mean number of strips in a cluster, regardless of particle type, was 4.6 and 3.6 in case the particle were a pion[85].

The reported performance for the FOPI RPC barrel shows an efficiency above 99%. The achieved time resolution of the full system, i.e. RPC + Start + Tracking is below 90 ps sigma, whereas RPC barrel alone was below 70 ps sigma. The strips provided also a spatial resolution below 1.7 mm in the y-direction (transversal) and 1.55 cm in the z-direction (longitudinal).

HARP

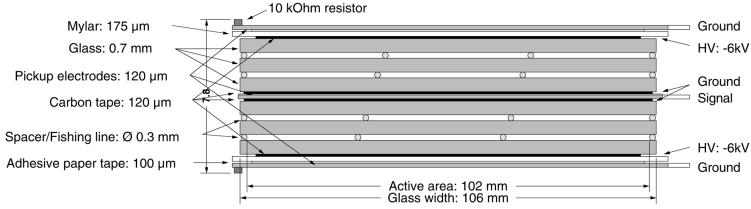


Figure 3.9: Schematic cross section of the RPC installed at HARP[86].

The HARP experiment is located at the Proton Synchrotron at CERN. The main aim of the HARP RPC wall is to provide particle identification in the momentum region where the TPC cannot distinguish neither electrons and pions in the 100-250 MeV/c range, electrons and kaons of 500 MeV/c nor electrons and protons at 1 GeV/c. The RPC system consists of 46 identical chambers of $1920 \times 106 \times 7.8$ mm³ each, 30 of them are placed surrounding the TPC detector and the other 16 are installed ~ 2 m downstream the target at forward angles and perpendicular to the beam axis[87].

Each RPC module consists in a four gap structure of 0.3 mm width defined by fishing line. The resistive material is float glass (soda-lime). The high voltage (-6.0 kV) is applied on the outer glass plates which are coated with graphite tape. The inner glass plate is grounded. The pick up electrodes are located in the center of the detector and the strip size is 29×104 mm², being connected by groups of 8 to the same pre-amplifier. Thus the total number of readout channels is $46 \times 64 / 8 = 368$. A schematic cross section of the detector can be found in Fig. 3.9. The used gas mixture is 90/5/5 (Freon/Isobutane/SF6)[86].

The intrinsic efficiency of the HARP RPC cells is above 99%. The observed noise rate is below 1kHz/m². Initially, the measured intrinsic time resolution was 150 ps[87], although, this number fell down to 127 ps sigma in a more recent performance publication[86]. Finally, the total time resolution, including the t_0 determination coming from the beam line, increase the value up to 175 ps.

STAR

The STAR experiment is located at the RHIC facility at Brookhaven.

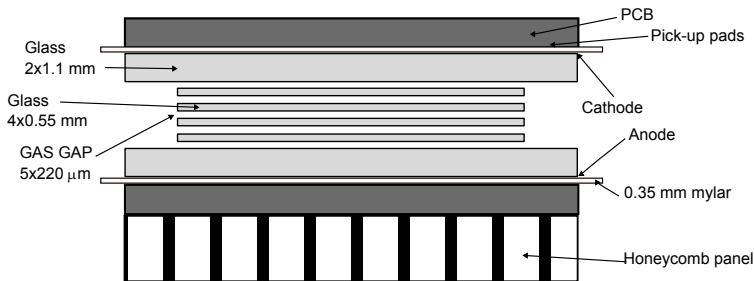


Figure 3.10: Schematic cross section of the RPC installed at STAR.

The goal of the RPC time of flight system is to provide particle identification up to ~ 3 GeV/c for pions, kaons and protons. In addition it is used to improve muon identification, which is extremely limited without the RPC TOF system.

The RPC system covers about ~ 50 m² and consists in 120 trays or modules arranged in two rings closed and surrounding the TPC detector. There are 32 MRPCs in each tray, with 6 3.5×6.1 cm² pads within each detector, thus the total number of channels is $160 \times 32 \times 6 = 23040$. The RPCs are made of float glass as resistive material, of 0.54 mm-tick, with five 220 μm gaps. The 14 kV voltage is distributed through graphite electrodes attached to the 1.1 mm-tick outer glasses. A schematic cross section of the detector can be found in Fig. 3.10. The used gas mixture is 95% Freon and 5% Isobutane: however, in the first prototypes the used mixture was 90/5/5 (Freon/Iso-butane/SF6)[88]. The expected maximum rate is about 200 Hz/cm² at a maximum occupancy of 12% in Au+Au collisions[89].

The intrinsic performance of the RPC system shows a time resolution about 74-82 ps sigma depending on the studied system, whereas the total ToF resolution, which includes start contribution was about 86 to 160 ps. The efficiency plateau starts at 15 kV and is above 95%[89].

Moreover, after the successful use and good performance of the STAR ToF RPC system, the RPC technology has been selected to be used in the STAR Muon Telescope Detector (MTD). The STAR electromagnetic calorimeter and the Magnet support provide ~ 6 interaction lengths. Thus, the fully reconstructed particles that pass through the whole detector and left signal in the MTD can be considered muons. The projected detector, is larger than the TOF's, and it will be composed by 117 modules covering

about $\sim 65 \text{ m}^2$. Each module or tray consists of a double-stack of float glass defining 5 gas gaps of $250 \text{ }\mu\text{m}$. The expected efficiency is about 95% and $\sim 70 \text{ ps}$ sigma time resolution[89].

3.3 General purpose RPC digitiser

Simulations are widely used as a powerful tools which allow to explore characteristics and performances, study design optimisations of the detectors or even full experiments. Many of the results obtained in complex experiments can be achieved only through detailed simulations of all the details of the experimental set-up which are inaccessible with analytical approaches. Moreover, simulations allow for a good efficiency estimation, as unfortunately, without dedicated set-ups in a complicated radiation and acceptance environment in most cases is the only reliable alternative.

Furthermore, simulations are used as a way to proof the validity of the theoretical explanations of the experimentally observed phenomena whenever the model, because of its complexity, non-existence of analytical solutions or large statistical fluctuations. Also simulations are very helpful when the model has no direct way to match the real measured data.

Here, two different approaches of digitising methods are shown and discussed. The first one is based on measured observables and uses this information to assign a value to all the measured variables as time, position and charge to a simulated hit as a function of previously parametrised values. The second one tries to produce a realistic output based on a macroscopic simulation of each event using as input parameters some detector characteristic as voltage and used gas mixture and combine this information with the number of primary ionisations produced by the simulated particle which is going to be digitised.

3.3.1 The empirical approach

The empirical approach has a direct implementation. Each fired RPC cell produces two times and two charges which are combines in three measured values: a time, a position and a charge. From previous analysis of these parameters as a function of the type of particle, its momentum and its angle we get a reasonable well described response of the detector.

This approach has an important advantage: what you measure is what you get in the simulation. At the same time, the weak point of this method is it relies on measurements and whenever the circumstances differ from the parametrised ones, the obtained values are no more describing the measurements. For example, setting a different voltage or threshold value will force to generate new parameters.

3.3.2 The macroscopic simulation approach

Behind the name *macroscopic simulation* we find a simplified method to simulate avalanches in Resistive Plate Chambers. It is called macroscopic because the microscopic events are neglected by integrating their contribution to the macroscopic avalanche parameters[90].

An important step forward in RPC simulation was done by W. Riegler and C. Lippmann. They performed a detailed simulation of all the process, starting from the primary ionisation, avalanche multiplication, drift velocity, etc... and the avalanche was simulated electron by electron to understand better its development[76][50][91].

This approach however is not suitable for detectors digitising purposes. The computational time and memory needed to simulate each avalanche makes impossible to generate responses of millions of particles. So, in terms of computational speed, is important to simplify as much as possible the model and the way how the response of the detector is codified, leaving for simulation only the essential process affecting directly the physical response. For most of the steps, analytical solutions are used.

The main ingredients of such code are:

- The detector geometry: size of the gap.
- The electronic configuration: the detector and electronic impedance and thresholds (Q_{th}).
- The gas parameters: the drift velocity and the Townsend and attachment coefficients.
- The weighting field E_w ² of the detector.

²Previously defined as E_v due to historical reasons, however nowadays is preferred the use of E_w notation.

- The incident particle properties.

The idea is, for a given geometry, gas and threshold, to reproduce the response of the detector with precision. The required steps to reproduce detector response are:

- Generate the position of the primary ionisations produced by the incident particle.
- Propagate analytically the avalanche within the gap, following some rules.
- Add the statistical avalanche fluctuations in the number of electrons.
- Reproduce the signal seen by the FEE.
- Calculate both the time at which the signal reach the corresponding threshold and the prompt induced charge.

The position of primary ionisations is randomly distributed along the path of the particle through the detector. The number of these e/ion pairs are taken from [76]. For MIPs and the gas mixture used the value is ~ 7.5 clusters/mm. From that moment the clusters are supposed to be independent and each one generate its own avalanche neglecting the field attenuation effect produced by other avalanches. A distribution of the closest pair to the cathode in a 4-gap RPC is shown in the Fig. 3.11

As each avalanche is supposed to be independent, we need a simple model to simulate how they grow. As a first approach we can use the model visualised in the Fig. 3.12. The most important assumptions made about the avalanche development are an exponential growth with exponential statistical fluctuation in the number of particles until the saturation limit. After reaching the maximum electron number N_{sat} in the avalanche, the space-charge regime dominates and we consider that the avalanche growth stops and electrons are assumed just to drift. Also it is important to stress out that it is supposed that the threshold value is far below the saturation limit and it will not affect efficiency or time measurement. The saturation number is introduced in order to limit the signal once the space-charge regime is reached to estimate better its influence in the induced prompt charge. This value is obtained from data and can be fixed for a better fit.

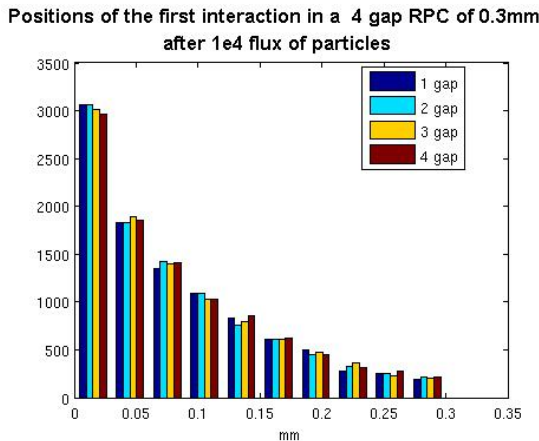


Figure 3.11: Simulation of the position of the closest primary cluster to cathode in a 4-gap RPC

The mean number of electrons present in the avalanche after a time t , given by Eq. 2.12, can be expressed, neglecting the diffusion coefficient, as:

$$\bar{n}_e(t) = n_0 e^{(\alpha - \eta)v_e t}. \quad (3.6)$$

and their statistics are described by the Furry law:

$$\frac{dN}{dn_e} = e^{-n_e/\bar{n}_e}. \quad (3.7)$$

Thus, once the mean number of electrons in each avalanche is generated, a posteriori, its modified by a random number from the exponential distribution to match the measured fluctuations. Otherwise the time resolution would be always zero.

From the Eq. 2.14, we can get the time wherein the Q_{th} is reached and the total induced prompt charge, keeping in mind the limit N_{sat} after which the exponential growth stops.

The other needed parameters, as the drift velocity and the effective Townsend coefficient, were extracted from [92][93][94]. The gases used in RPCs are well known in industry by their cooling and their behaviour under strong electrical fields is of great interest for insulating purposes.

Finally, regarding performance of the method, in first place, in the Fig. 3.13 we show the charge spectra for a 4 gap of 0.3 mm using a $N_{sat} = 4.2 \cdot$

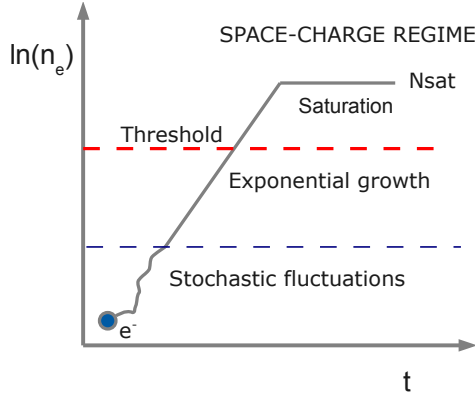


Figure 3.12: A simplified model showing the growth of an avalanche. For details see the text.

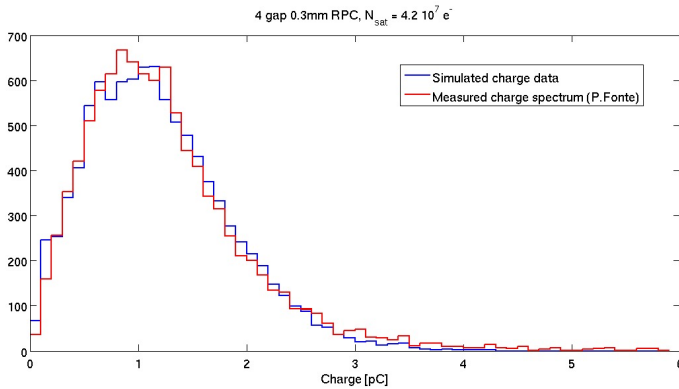


Figure 3.13: Simulated vs measured charge spectra of a 4-gap of 0.3 mm RPC with $N_{sat} = 4.2 \cdot 10^7$. The measured charge spectra was taken from [95]

10^7 , below the Raether limit[97]. The comparison between the measured efficiency and the simulated is shown in the Fig. 3.14 while the comparison between the measured time resolution and the simulated is shown in Fig. 3.15.

This approach was evolved by D. González-Díaz. in order to allow to predict the performance of whichever RPC design is chosen. Moreover, other effects as crosstalk were included in order to improve the prediction

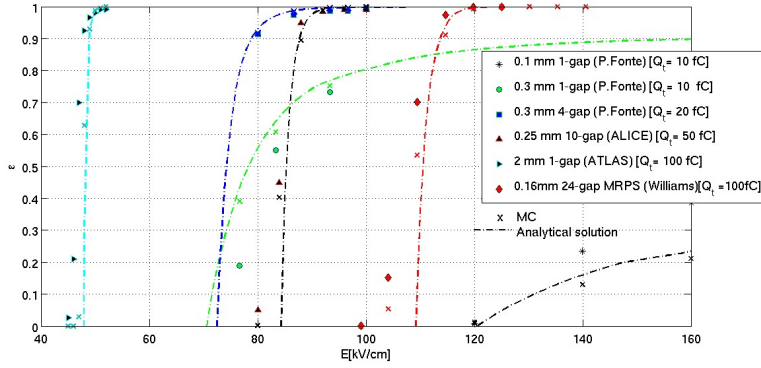


Figure 3.14: Comparison between measured efficiency (full symbols) of several RPCs and its simulated value (crosses). The data was taken from [95][79][62][96]

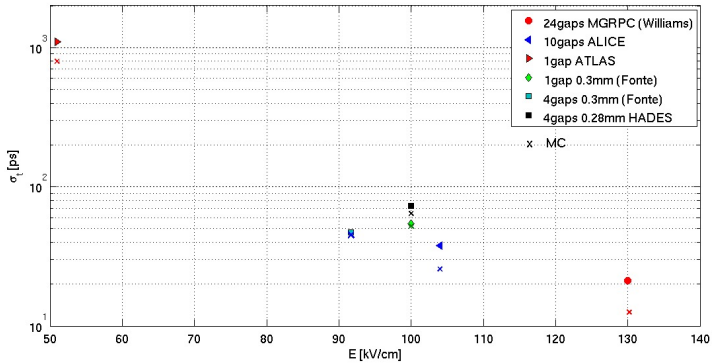


Figure 3.15: Comparison between measured time resolution (full symbols) of several RPCs and its simulated value (crosses). The data has been taken from [95][79][62][96]

capability of the performance of multi-strips RPCs. The idea of testing geometry and read out designs without the need of building prototypes lead to the development of dedicated software tools for Resistive Plate Chambers simulations[98].

4 Performance of the HADES RPC-ToF Wall

In August of 2011, HADES took data for the first time with a gold beam on a gold target after a deep upgrade of the system, concerning the lower angle Time Of Flight detector, the Front End Electronics, the data acquisition system and a new Forward Hodoscope wall. All these elements were developed and installed in order to meet the needed specifications of high multiplicity gold on gold events.

In this chapter we present the results of the analysis of the performance of the RPC-ToF wall detector within the HADES reconstruction software framework: HYDRA¹. For this purpose, dedicated algorithms and macros were written in tune with the existing C++ classes and methods. Besides calibration tasks, which were already partially implemented within HYDRA framework, a new sets of methods and algorithms designed for efficiency and resolution calculations are presented. In previous reports those calculations were done using mostly MATLAB source code [99], [69], [100], [71], [101]. Here, we also have the opportunity to merge results obtained with different strategies and frameworks, which gives it true solidity. It is important to highlight that as calculations follows different algorithms, some results could differ but always keeping consistency between them. This is the case, for example, of the new time-position correction, which takes advantage of the track position determination accuracy given by the MDCs, instead of using a one dimensional correction using the RPC position information. Of course, this technique cannot be used as a self-calibration procedure as it relies on track positioning from the HADES track reconstruction software, but it allows to correct in two dimensions the gain inhomogeneities present in the cells due to small variations of the gap of gas.

Before going into the analysis of the performance, it is important to understand the used calibration procedures. The total amount of read-out channels sets a strong constraint on the stability of the output of

¹HYDRA: **H**ADES **s**ystem for **D**ata **R**eduction and **A**nalysis

the calibration procedures. The implemented algorithms must be suitable almost for all cells. Moreover, it must meet computational time and space requirements and it should be possible in the future to get different sets of calibration parameters within the same beam time. Otherwise, future corrections related with the gain variation with pressure or temperature would not be possible to perform.

The high requirements that the RPC-ToF wall should meet in order to handle efficiently the entrusted tasks are the key part of this chapter. Efficiency, time and position resolution were assessed in detail.

The capability of particle identification through charge measurement in the RPC is limited, as it was already shown in [102]. Nevertheless, this feature is not only interesting for calibration purposes, as it was pointed in [103], but also it has special interest from statistical point of view, as it will be shown in the next chapter 6, related with cosmic ray analysis. Despite a single particle cannot be definitely identified by its charge, taken together, charges coming from several particles in the same event can shed some light on the cocktail of particles. This is quite difficult if many types of particles come into play but, in cosmic ray events, we have mostly high energy muons and low energy electrons, showing a very different behaviour.

Finally, the multihit capability of the RPC is revised. With usual procedures, a double hit in the same RPC cell if the second arrives before the signal from the first reaches both electrodes, a priori is lost. Here, a method to partially recover these hits is shown.

4.1 Calibration

Here, as mentioned above, we will focus on calibration algorithms and methods. It is important to bear in mind the design, geometry and technical issues described in the Section 3.2.

4.1.1 Position calibration

The longitudinal coordinate along the RPC cell is calculated by the time difference between measured times at both ends. As a consequence an offset arise due to a slightly different electronics and mostly due to the length of the signal cable between the cell and the FEE electronics. The

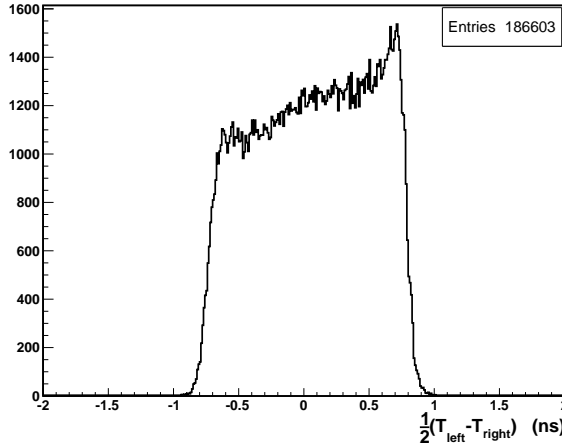


Figure 4.1: $\Delta T/2$ distribution used to characterise the position offset. Notice the excess of statistics on one side. This effect comes from the inhomogeneous density of particles, especially significant in the lateral columns.

position determination can be written as follows:

$$x_{RPC} = \left(\frac{T_{left} - T_{right}}{2} + x_o \right) \cdot v_s, \quad (4.1)$$

where x_o is the constant offset needed to correct the aforementioned effect and the v_s is the signal propagation velocity in the cell, ~ 177 mm/ns [101]. This offset can be estimated by determining the left and right edges of the time-difference histogram as it is shown in Fig. 4.1. However, this method was not precise enough for alignment purposes in HADES, as it requires a position accuracy better than 1 mm. The main limitation of this method concerns the correct determination of the edge, as in case of non uniform radiation, each end has its own threshold value. Moreover, the non symmetric design of the cells of the first and third column adds a complication to an already unfavourable situation. Thereby, it was decided to make the fine-position-calibration while alignment is done, by introducing this offset as a free parameter [104].

Concerning the position calibration of the data acquired during the cosmic test described in chapter 6, the uniform distribution of cosmic rays and

the Y-coordinate uncertainty makes the accuracy provided by this method enough for the entrusted tasks.

4.1.2 Width to Charge calibration

The charge of the avalanche, see section 3.2, is stored in the width of the FEE output signal through the charge to width (QtoW) algorithm [103]. It is a mandatory process to reverse the charge codified in TDC bin units back to physical units. This is achieved in several steps. First of all, the measured QtoW value in TDC bins is multiplied by the TDC-time conversion factor, converting it to ns. Then, the QtoW pedestal is subtracted in order to homogenise the response of each FEE channel, as they have a slightly different behaviour. This is accomplished by a method that locates the time emplacement of the left edge of the QtoW spectra. It is important to bear in mind that signals below this left edge are mostly crosstalk events without a real charge. Despite the RPC strips are electrically isolated by aluminium shielding, some large signals, coming mostly from streamers can still produce an induced crosstalk signal in their neighbours. Most of these induced signals can be removed by asking to have a measured charge above zero. But coming back to the calibration question, once the pedestal is subtracted and the measurement is already in ns, we can convert it into physical charge units through a sixth order polynomial parametrisation. The WtoQ calibration is explained in detail in [69] and [102].

4.1.3 Time of Flight calibration

Time measurement is the primary role of the RPC-ToF wall within HADES spectrometer. It is thus essential to have a very accurate time calibration. Owing to the specific geometry, design and acquisition this procedure must be accomplished in several stages, explained in detail here. Stated briefly, time calibration is done in four steps:

1. A rough time calibration is performed positioning the the time of flight spectra for all cells at a constant value.
2. Time spectra from overlapped events is centred in zero, thus allowing a correct slewing correction, regardless of their offsets.

3. The reconstructed time of flight from tracked momentum is used to establish correctly the measured time offset.
4. The two dimensional reconstructed position from tracking is used to correct small deviations in gain along the gap.

The following is a more detailed explanation of these methods, stressing the importance of the convergence of the algorithms for all the RPC cells.

4.1.3.1 Offsets with tracking: protons and pions

Calibrations tasks are usually made independently of other systems of the HADES spectrometer. In this case, we are using the reconstructed momentum from the Runge-Kutta method and the particle path length[2]. This method relies on a good alignment and START detector calibration, making this procedure iterative because start time calibration uses information from both TOF and RPC detectors. There are several reasons which led to that decision. On one hand, the particle path length between the target and the position of the RPC cannot be estimated without tracking detectors if the high intensity magnetic field is on. On the other hand, an algorithm that uses the hypothesis that the time of flight of the fastest particles, usually leptons, is set constant in the TOF spectra, one must find correctly this value, leading to an unnecessary additional possible error. If all RPC cells in one sector are synchronised and that value is obtained at once for all of them, even then, this cannot warranty the needed calibration quality.

Much effort has been put into achieving the time self-calibration of the RPC but, unfortunately, the final time offset still need external information from other systems. The possibility of using Monte-Carlo simulations to produce the desired results seems not to be a convenient solution, as each experiment have its own characteristic, e.g. target position, beam intensity, etcetera.

As a first approach, we can take advantage of the overlapped geometry of the RPC cells. Centroids of time differences through the successive cell rows give a reasonable start point for other more precise calibrations. This method was used as a starting point for the time calibration in the section 6.3.1.

Returning to the subject in question, the strategy followed is as simple as select particles with a known momenta. Then, by introducing the mass hypothesis it is possible to obtain the time of flight as:

$$T_{mom} = L/v, \quad (4.2)$$

where L is the path length of the tracked particle and v is its velocity. The travelled distance is obtained directly from tracking and the velocity can be derived from momentum p and energy E as $v = p/cE$. Bearing in mind that $E = \sqrt{p^2 + m_0^2}$, the previous expression can be rewritten as:

$$T_{mom} = Lc\sqrt{p^2 + m_0^2}/p. \quad (4.3)$$

Once we have an estimated time of flight from momentum, we use the following condition to get the correct offset for each cell:

$$\Delta T = T_{RPC} - T_{mom} = \tau_{RPC}, \quad (4.4)$$

being τ_{RPC} the correct time offset.

Thus, the main role in this calibration is a correct particle selection for calibration purposes. The section title gives us a clue about the selected particle species. Moreover, it is important to take into account two processes that may distort the final time of flight: the energy losses and the multiple scattering. At first sight, both contribute to make larger the measured arrival time, but momentum is reconstructed using inner and outer segments of the MDC detector. Thus, the reconstructed time of flight from the momentum is not taking into account the energy losses before the magnetic field. These effects make the characteristic behaviour showed in the Fig. 4.2.

For these reasons, it was setted a cut in momentum for protons over 1100 MeV and for pions over 300 MeV. The initial idea was to use only protons, as it is the most common particle in the cocktail and multiple scattering is not so relevant as it depends on the momentum, but the acceptance for protons over the threshold value left the innermost part of the detector uncovered. To fill the empty region, pions were selected. It is important to highlight that the mass hypothesis is applied to all tracked particles without any previous assumption. This means that if the particle was in reality a deuterium or a positron instead a proton or pion, it will be used

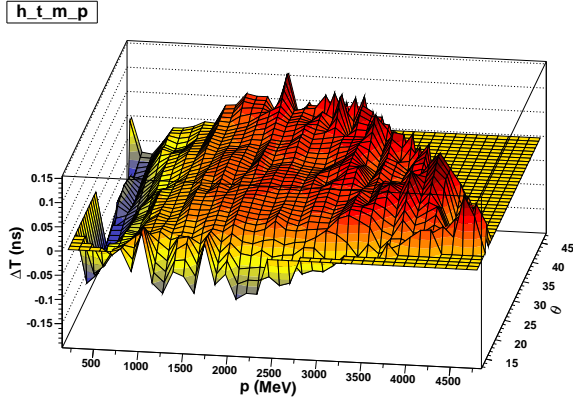


Figure 4.2: Figure showing the dependence between momentum - production angle and the difference between measured and expected time of flight for protons

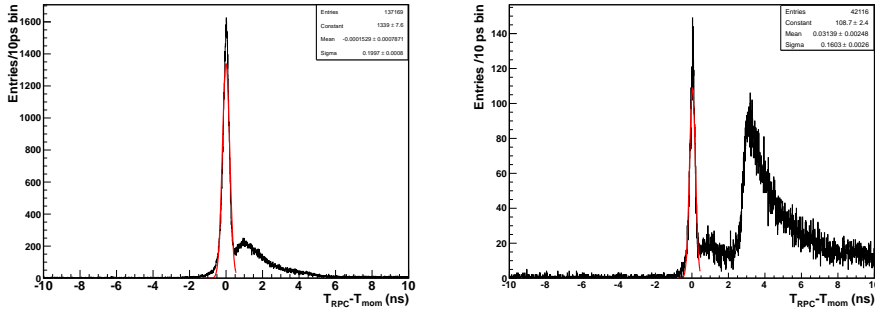


Figure 4.3: Time of flight spectra ($t_{rpc}-t_{mom}$) for proton and pion hypothesis. Left: spectra with pion mass hypothesis. Right: spectra with proton mass hypothesis.

to fill the histogram too. However, it will not contribute to the centroid of the ΔT peak as it is shown in the Fig.4.3.

The centroid of the peak of the Fig. 4.3 is the offset of the cell. Large statistics are needed, as the variance of the centroid depends on the square root of the number of entries.

Once reached the desired results, the method was applied once again to already calibrated data to estimate the possible miss-calibration and the

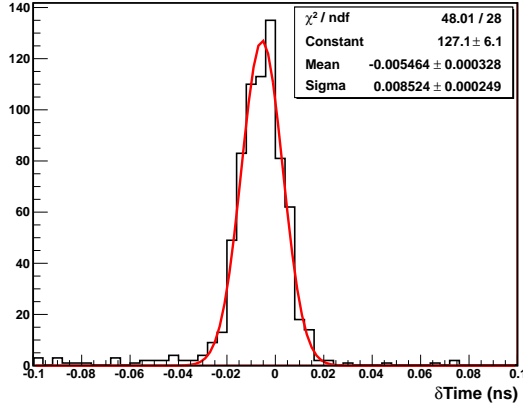


Figure 4.4: Difference between time of flight calibration parameters and the obtained if the method is applied once again to an already calibrated data. The 8 ps Gaussian sigma shows that the convergence is reached and can be interpreted in terms of synchronisation and quality of the calibration.

fluctuations of the previously found solution. The result of this stress-test to the algorithm is shown in the Fig. 4.4.

4.1.3.2 Slewing correction

The correction of the charge to time correlations is a mandatory step. It can improve the time resolution of RPCs by 20%-50% [50]. Many discussions did take place regarding this issue [95],[72],[50]. Here, we will focus only on the technical aspects of the charge correction method; a detailed discussion of this correlation is done in 4.3. Experimentally was found that the charge correction can be done by localising the two regions in the charge spectra with different behaviour, both of them having an exponential behaviour [72], [75]. The method implemented here was described in [71], and it consists in fitting the two regions to two polynomials, rather than exponentials, as it is more robust and less dependent on locating the exact point where the trend changes. The result of applying the charge to time correction is shown in the Fig. 4.5. The improvement of time resolution is apparent and is about 25% or 25-30 ps and is consistent with

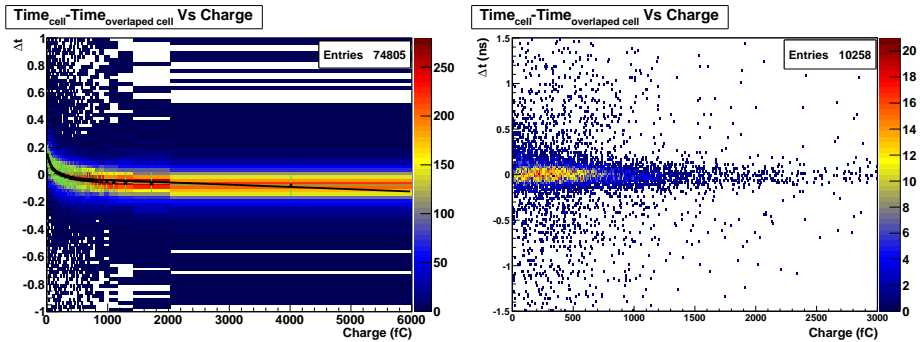


Figure 4.5: Correction of the charge-time dependence (slewing correction) in a RPC cell. In the left is shown the histogram used for calculation of the correction parameters. The bins width is set in order to have the same statistics in them. The black triangles are the Gaussian mean position for each charge slice and the black curve is the resulted fit. On the right is shown the ΔT distribution for the same cell after correction. The rising time at low charges have disappear completely.

other reported data before.

4.1.3.3 Position - Time dependence correction

Behind the name “Position - Time correlation” is found the last and finest correction of all the aforementioned methods. This correction tries to minimise the local effects that could be present in the cells. Slight deviations in the gap size, of the order of few microns, can introduce an systematic offset in the time measurement.

This method can be implemented in two ways: the first one relies on the correlation between longitudinal position and time in two overlapped cells as it is done in the slewing correction 4.1.3.2. This is the standard implementation, as reported in [99]. The improvement in time resolution with this method is around 10%.

The second one, uses the positioning from tracking, providing a second dimension to the correction. This method relies on tracking accuracy and requires a big amount of data to calculate the needed parameters. The strong point of this approach is the possibility to correct local gain devi-

ations in both dimensions, X and Y. There are two weak points: the first one is the dependence of tracking and the second one is the huge data amount needed, as it makes impossible to make several parameter sets. Indeed, this approach follows the same strategy as in 4.1.3.1, although, the physical meaning of the corrected effect is not the same.

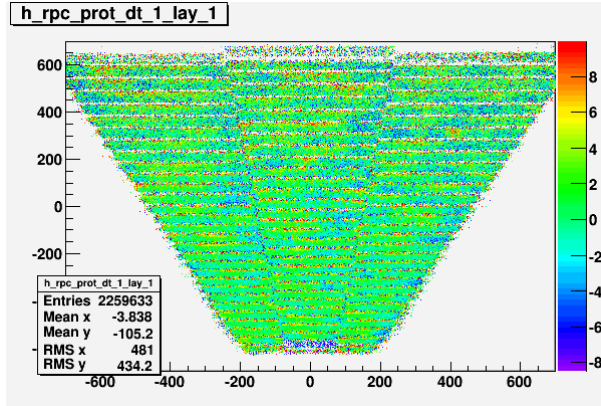


Figure 4.6: Correction matrix for one layer of one sector of the RPC for the position-time correlation. The colours represent the time deviations for each region in units of 10 ps, thus the maximum value 8 = 80 ps.

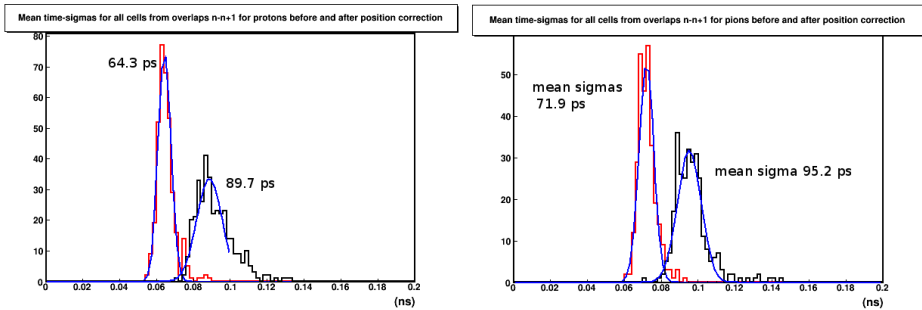


Figure 4.7: Improvement in time of flight resolution after correcting the time-position dependence. Left: improvement for protons (30 %). Right: improvement for pions (25 %)

In the Fig. 4.6 we show the correction matrix as a result of this method.

The time resolution achieved after this method is improved by 30-25 % as it is shown in the Fig. 4.7 for selected protons and pions.

4.2 Efficiency and position resolution

Each recorded event in the RPC, stores both the time and charge information read-out at both ends and information about the position of the cell in the detector. On the basis of this information, and after all the calibration procedures, the RPC provides two values: a time and its related coordinate. As we have left and right signals, the longitudinal position is obtained directly as the half time difference times the signal velocity in the cell. The transversal coordinate is given by the geometry and its resolution depends only on the cell width. The measured time is obtained as the half of the sum of the left and right times. Taking advantage of the two layers design, the quality of these measurements can be estimated in two ways: using the information provided by tracking or by characterising the distributions of overlapped events.

4.2.1 Position resolution

The accuracy of the position determination of a hit, directly impacts the matching quality between the META detectors and MDC-Magnet system. A well understood position resolution helps to prevent fakes. All matching procedures only use the transversal and longitudinal coordinates discarding time measurement.

The transversal position resolution is given by the geometry and the readout. Considering an uniform hit distribution in the Y-axis, the resolution is:

$$\sigma_y = \frac{Width}{\sqrt{12}}. \quad (4.5)$$

The design was sought to have the same radiation load over all the cells, independently of the geometry. Thus, in order to cover the whole angle range and fulfil the specifications, cell widths grow with cell number from 22 up to 42 mm width.

The intrinsic longitudinal position resolution is calculated with particles

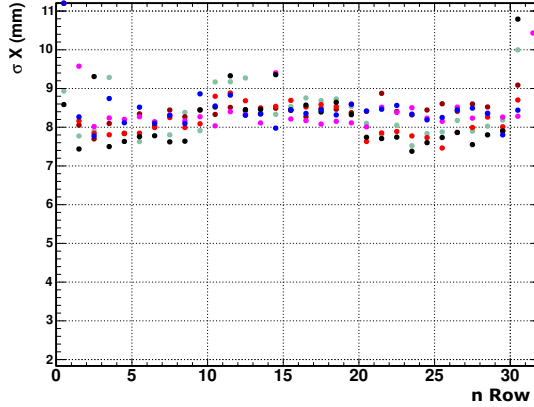


Figure 4.8: Longitudinal position resolution for all the RPC cells of one sector obtained characterising the distribution of the position differences between the tracking and the RPC. Each column is represented by one colour. The mean obtained resolution is of 8 mm sigma.

which left signal in two overlapped cells by characterising the distribution:

$$\Delta x_{up-down} = \left[(t_l - t_r) \Big|_{up} - (t_l - t_r) \Big|_{down} \right] \cdot \frac{v_s}{2} \quad , \quad (4.6)$$

which is, in fact, just the difference between measured positions in the overlapped region of both cells. The intrinsic resolution is given by

$$\sigma_X = \sigma(\Delta X_{up-down}) / \sqrt{2}$$

assuming both cells contribute equally. The $\sigma(\Delta X_{up-down})$ is the sigma of the fitted Gaussian distribution around the maximum in the interval with 1.5σ width. The mean longitudinal resolution is around 8 mm, as reported in [105].

The position resolution can be calculated also comparing the given position by the tracking at the RPC and the measured position in the cell. Thus, the resolution is obtained by characterising the distribution:

$$\Delta x_{rpc-rk} = x_{rk} - x_{rpc}, \quad (4.7)$$

where x_{rk} is the intersection of the trajectory of the particle with the RPC obtained using the Runge-Kutta method. In the Fig. 4.8 are represented the position resolution for all the cells of one sector.

4.2.2 System time resolution: START time from tracking+RPC

The spectrometer system resolution is influenced by the uncertainties of START, tracking and the RPC ToF wall. In order to study the contribution of each detector to the final resolution we have followed the following strategy:

- Clean Au+Au collisions: events with only one interaction in the target and multiplicities in the RPC wall above 9 particles.
- Correction of the measured momenta as a function of initial production zenith angle and momentum of the particles.
- Recalculate event START time using corrected information from tracking and particle identification by velocity-momentum cuts.
- Recalculation of the new differences in the $t_{rpc} - t_{mom}$ spectra.

The first step must be performed mandatory because interaction probability in the target was $\sim 2\%$. As a consequence, beam particles may have several reactions within the same time window affecting time and start reconstruction. The requirement of at least 10 particles in the RPC is set as the minimum threshold value as not all of these particles would successfully be identified. The identification was performed on positive and negative pions and protons, the most abundant species in the cocktail.

The second step is to counteract multiple scattering and energy losses which contribute to distort the time obtained from the momentum. For each selected particle, it was calculated previously an correction factor in time units as a function of the initial zenith angle (θ) and its momentum p . Thus, the time of flight of the particle t_{mcorr} , obtained from the momentum, can be expressed as follows:

$$t_{mcorr} = path \cdot \frac{\sqrt{p^2 + m_0^2} \cdot c}{p} + t_{corr}(p, \theta), \quad (4.8)$$

being m_0 the rest mass of the selected particle and $path$ the travelled distance from the target to the RPC. The correction values for positive and negative pions are shown in the Fig.4.9. The proton correction matrix was already shown to illustrate this issue in the Fig. 4.2.

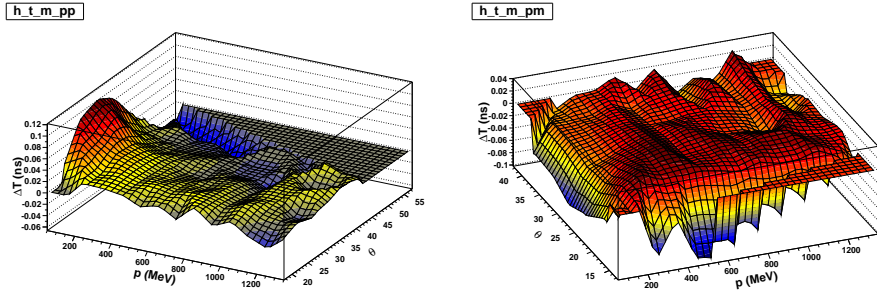


Figure 4.9: Correction matrices as a function of the momentum and zenith angle ($t_{corr}(p, \theta)$) for both, positive (left) and negative (right) pions.

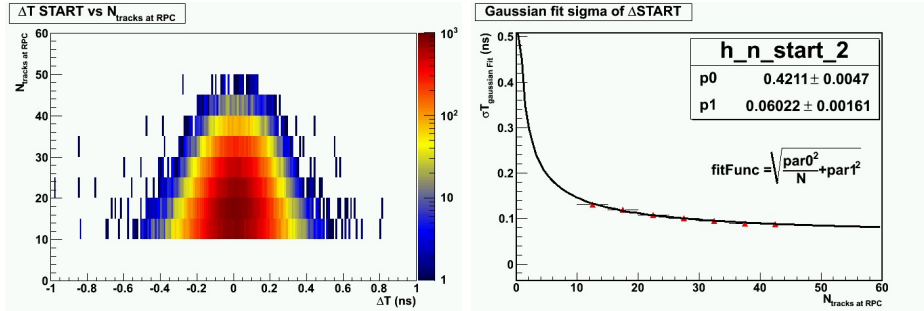


Figure 4.10: Recalculated start time from traced particles in the RPC (left) and START detector resolution obtained from the fit: 60 ps sigma (right).

Once the time is corrected, the mean values of the offsets of the measured and calculated time is calculated as a new reaction start time. The distribution of $t_{rpc} - t_{mcorr}$ is closely related to the START resolution, as the uncertainty of the calculated start time can be supposed to contribute proportionally to the square root of the number of tracks used in the calculations. The distribution of the obtained start times as a function of number of particles in the calculation together with the START detector resolution are shown in the Fig. 4.10. The obtained resolution using the hypothesis that recalculated start time resolution improves with square root of number of tracks, is of 60 ps sigma.

On the other hand, the contribution from the uncertainty of the momentum determination from tracking is around 2%. Thus, the $t_{rpc} - t_{mcorr}$ distribution versus the momentum of the incident particle is a good estimator of the time of flight resolution. At velocities close to speed of light, $\beta = c$, this 2% does not contribute to the time resolution. Making the hypothesis, as in the previous case, that the limit where the contribution of the momentum is negligible, the constant term is the system time of flight resolution. The obtained value was of 80 ps sigma for pions, the most unfavourable case, which is compatible with the value obtained from characterising the time distribution of overlapped cells. The $t_{rpc} - t_{mcorr}$ distribution as a function of the momentum and the determination of the system resolution are shown in the Fig. 4.11.

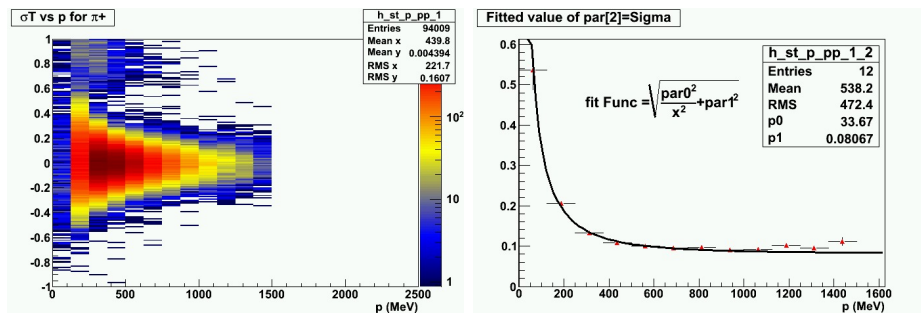


Figure 4.11: System resolution of the time of flight for positive pions, showing a 80 ps sigma as once the momentum contribution is subtracted.

4.2.3 Efficiency

The efficiency of the RPC TOF wall can be obtained by following detected particles through the volume occupied by the detector. To suppress partially fake tracks, is asked to have a hit in the Pre-Shower detector that is located behind. The allowed matching window for the tracks should fulfil:

$$\left(\frac{x_{rpc} - x_{rk}}{\sigma_x}\right)^2 + \left(\frac{y_{rpc} - y_{rk}}{\sigma_y}\right)^2 \leq 25, \quad (4.9)$$

for the RPC detector and the same criteria for the shower.

Moreover, to suppress the effect that the incidence angle may increase artificially the efficiency real value, particles with an incidence angle less than 5° were selected. This criteria also enhance the cell structure and the regions covered by two cells will present a gain in efficiency. The opposite behaviour is expected for the regions covered only by one cell with independence of belonging to the top or the bottom layers. Furthermore, events with less than 40 hits in the RPC were selected to improve fake tracks rejection.

After the cuts, the efficiency was obtained as a function of the y-coordinate for the central layers. The RPC was operated at 5500V, a balanced value between efficiency and low streamer probability, which in high occupancy Au+Au events is of utmost importance: large discharges may induce crosstalk signals to the neighbouring cells. The resulting values of efficiency are shown in the Fig. 4.12.

A modulated profile is apparent between a minimum and a maximum efficiency values, ε_{min} and ε_{max} , respectively. This modulation along the areas covered by one or two RPC cells can be used to derive the intrinsic efficiency ε_{int} . Lets suppose that exists an external efficiency factor ε_{ext} , thus:

$$\varepsilon_{min} = \varepsilon_{int} \cdot \varepsilon_{ext} \quad (4.10)$$

and

$$\varepsilon_{max} = (1 - (1 - \varepsilon_{int})^2) \cdot \varepsilon_{ext}. \quad (4.11)$$

Solving this system we can get the efficiency as a function of the values in the maximum and minimum as:

$$\varepsilon_{int} = 2 - \frac{\varepsilon_{max}}{\varepsilon_{min}}. \quad (4.12)$$

Now, taking into account that $\varepsilon_{min} \simeq 0.935$ and $\varepsilon_{max} \simeq 0.985$, the obtained efficiency is $\varepsilon_{int} = 0.946$. Bearing in mind that overlap region covers half of the detector, the total intrinsic efficiency of the RPC TOF wall is:

$$\varepsilon_{total} = 0.971 .$$

The same strategy was applied to investigate the most unfavoured case: negative pions above 300 MeV, which are minimum ionising particles. In this case, the incidence angle window was widened up to 10° because of a statistical lack of negative pions with normal incidence on the detector.

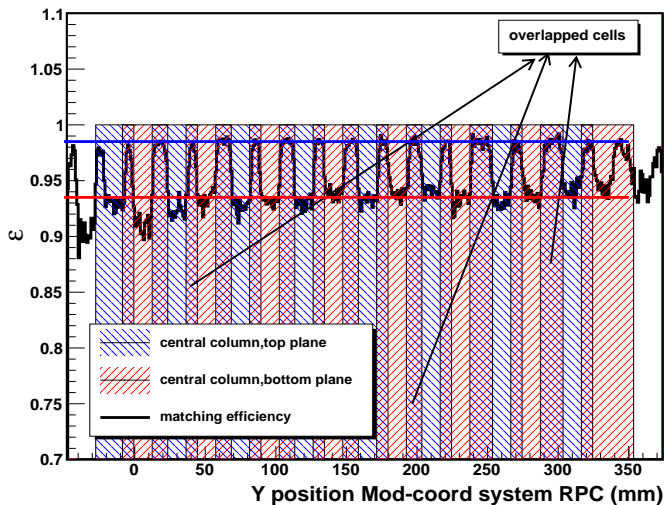


Figure 4.12: RPC efficiency as a function of the transversal y -coordinate. The minimums and maximums shows clearly the modulation effect produced by regions which are covered by one or two overlapped cells. The vertical bars coloured with blue and red indicates cells from the top or bottom layers. In the overlap region both colors are present. From these values an intrinsic resolution of 97.1% can be extracted (for details see text).

The other reason of selecting negative pions is that they can be identified by the polarity of the bending in the magnetic field and no time information is needed. Other negative particles are highly suppressed in the cocktail or in the case of electrons, they mostly have low momentum. The obtained modulation is shown in the Fig. 4.13.

Making the same calculations as in the previous case, taking as the minimum value $\varepsilon_{min} \simeq 0.875$ and maximum $\varepsilon_{max} \simeq 0.960$, we obtain a mean efficiency over the RPC for negative pions of

$$\varepsilon_{total \pi^-} = 0.946 .$$

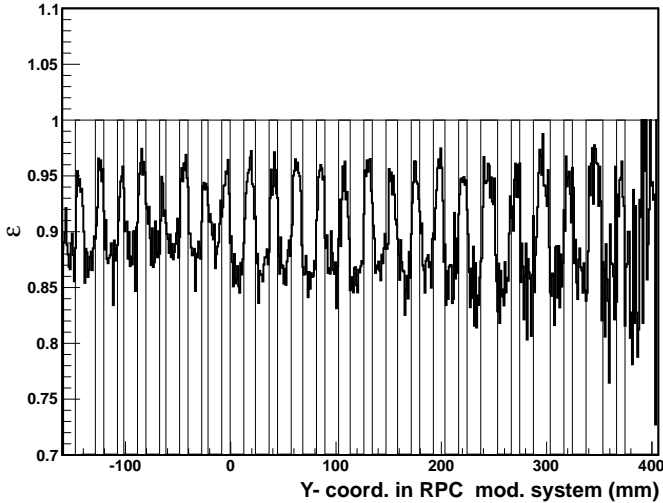


Figure 4.13: RPC efficiency modulation as a function of the transversal y-coordinate for negative pions. Vertical lines indicate the edges in the y-coordinate of the RPC cells. From these values an intrinsic resolution of 94.6% can be extracted (for details see text).

4.3 Extended charge study

The measurement of the prompt charge of an avalanche in a RPC detector is mainly used to improve time resolution by applying the slewing correction. In this section we will focus on the behaviour of the charge dependencies with momentum, velocity, resolution, angle and streamer fraction in order to understand better the detector response and to improve future digitising algorithms and particle identification.

Even though RPCs are not proportional detectors and the relation between the energy loss by a particle and the measured charge depends on other factors, on average this information still remain partially. Furthermore, another difference with other gaseous detectors used to measure the energy loss is that, the amplification region correspond with the ionisation region, i.e. ionised electrons are immediately affected by the high electric field existing in the gap. This aspect will be important to understand the implications of the observed behaviour.

4.3.1 Methods

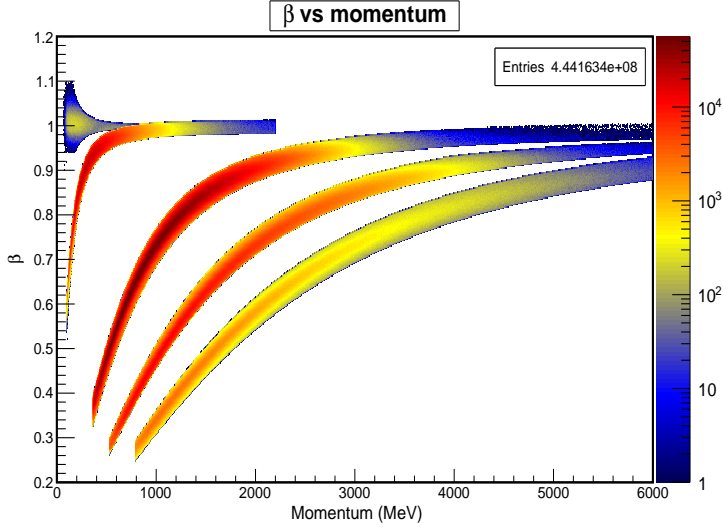


Figure 4.14: β vs momentum plot of the selected particles used in the charge analysis. Starting from the top left we can find electrons and positrons, pions, protons, deuterium/helium and tritium.

The charge analysis was performed relying in the HADES tracking system which provides accuracies in momentum around 2% and good capability of particle identification, using cuts in the β vs momentum distribution. The selected particles in this analysis are shown in the Fig. 4.14 and are namely e^\pm , π^\pm , protons, deuterium/helium and tritium. The deuterium and helium lines are superimposed because momentum reconstruction implicitly supposes particles charge being unity. Then, particles having the same mass-charge relation will appear in the same region in the plot. Electrons were selected by requiring coincidence with the Cherenkov RICH detector.

As the data come from Au+Au collisions, a hard cut on the number of hits in the RPC was set: events with less than 8 hits or more than 60 hits were suppressed to avoid contamination in the charge coming from double hits and to minimise the fraction of events contaminated by other reactions within the same time window. Moreover, the incidence angle of

the particles at the RPC was limited to a narrow band $0.18 \leq \theta \leq 0.225$ rad, to avoid angular effects.

The analysis includes relations among variables that can be either directly measured, obtained from the measured values or are statistically obtained from the distributions. They are summarised in the Table. 4.1. It is important to stress out that both, the Lorentz factor and the velocity, are obtained from the measured momentum of the particle and, at any time, the time measurement plays any role. This is done in this way to disentangle the possible correlations between charge and velocity measured by the RPCs.

Accessible variables		
Direct measurement	individual	statistical
q		$\langle q \rangle, s_f, \varepsilon$
$t + \theta$	$\Delta t = t_2 - t_1 - ToF(\theta, p)$	σ_t
p	$\beta(p, m_0), \gamma(p, m_0)$	

Table 4.1: Variables accessible in the RPC charge study. From the directly measured variables such as charge q , time t , incidence angle θ and momentum p we can obtain other variables as the time difference Δt in overlapped cells corrected by the time of flight between them, $ToF(\theta, p)$ or the Lorentz factor γ and velocity β . Moreover, from the charge distribution we can calculate the median charge $\langle q \rangle$, the streamer fraction s_f and the efficiency ε . From the Δt distribution we can obtain the time resolution. All these variables were used in the charge analysis.

The measured charge distribution provide three important quantities: the median charge, the efficiency and the streamer fraction. The use of the median charge instead of the mean is motivated by the highly asymmetrical charge distribution. It was already discussed in the Section 2.1.3 as a more useful parameter to describe ionisation processes in thin detectors.

The efficiency and the streamer fraction in a charge distribution is obtained as it is shown in the Fig. 4.15. The charge spectra is represented with the black line and the functions used to estimate efficiency and streamer fractions are the red and the blue ones respectively. The function $f_\varepsilon(q; a)$ which encloses the blue area, or the inefficiency, is $f_\varepsilon = aq^b$, being b the slope of the exponential as it is painted in logarithmic scale. Thus,

the efficiency is given by:

$$\varepsilon = 1 - \frac{\int_{-\infty}^0 f_{\varepsilon}(q; a)}{\int_{-\infty}^0 f_{\varepsilon}(q; a) + \int_{q_{min}}^{q_{max}} q} \quad (4.13)$$

The function $f_{sf}(q; a, b, c)$, we use to estimate the behaviour of the charge spectra at high values to separate streamers from large avalanches, is $f_{sf} = aq^b e^{-q/c}$. Thus, the number of streamers in the sample is the enclosed area between the spectra and the fitted curve and its fraction is the ratio between the extrapolated area and the total area.

A more standard way of calculating the streamer fraction is to set a hard cut in the measured charge, considering signals above some constant value - streamers. This approach has the inconvenient of mixture both, normal avalanches and discharges and in some conditions, were a big fraction of avalanches with high values, can increase artificially the streamers fraction estimation.

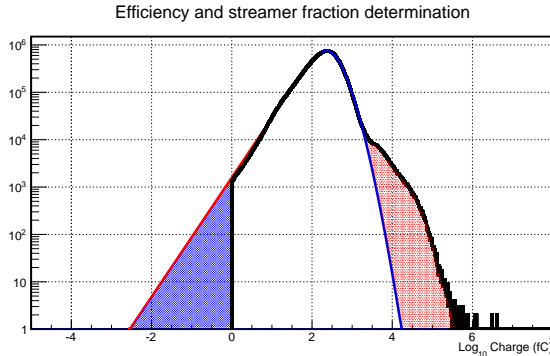


Figure 4.15: Efficiency and streamer fraction determination from the charge spectra. The black line represents the charge distribution, the red line is the function used to calculate the inefficiency area (blue) and the blue line delimits the separation between normal avalanches and streamers, coloured in red.

The time resolution is obtained characterising the distribution:

$$\Delta t = t_2 - t_1 - ToF(\theta, p). \quad (4.14)$$

These distributions are fitted to Gauss functions in the interval $\pm 1.5 \sigma$. This value, besides the uncertainty in the time measurement, offers an

estimation of the internal jitter of the induced signals, being these the main source that affects the time resolution since the charge to time dependence was already subtracted.

Results are sorted in the following way: first we present the trends and correlations between efficiency, time resolution - median charge for heavy charged particles (π^\pm , p, d/He, t) as a function of the velocity β and the momentum normalised to the mass, $\beta\gamma$. Then, we analyse the streamer production probability and the dependence of the charge and efficiency with incidence angle. The next results concerns the time-charge correlation, and deviations from the expected behaviour is shown for protons. Finally, the charge analysis including efficiency, resolution, streamer production probability and median charge is presented for e^\pm .

4.3.2 Efficiency determination through the charge spectra

The method used to determine the efficiency of the particles through the estimation of the inefficiency area is represented as a function of β and $\beta\gamma = p/m_0$ in the Fig. 4.16. These two curves enhance the trends at low energy of the particles and at values above the ionisation minimum, located at $\beta\gamma \sim 3$, seen in Section 2.1.

The mean energy loss, given by the Bethe-Bloch approximation has one important feature: it is independent from the mass of the incident particle. As the mean energy loss is closely related to the number of primary clusters (secondary electrons and ions in the gas), from both figures we conclude that the efficiency follows the expected behaviour at low energies, where ionisation grows exponentially and thus efficiency for heavy charged particles reaches 100% at velocities below 0.45 c. For larger velocities, the curves start to diverge, being their rest mass a scale factor between them. This separation stays at high momenta and, then, we can conclude that this effect is related to the avalanche formation in the initial steps of the multiplication. Besides the mass scaling factor and a possible shift observed in the location of the minimum the trend is the expected one.

Values obtained for the efficiency using the charge spectra analysis method, slightly differs from the results obtained from the matching efficiency with matching detector being about 1% larger. Nevertheless, the incidence angle selection is different for both cases and a small decrease is expected.

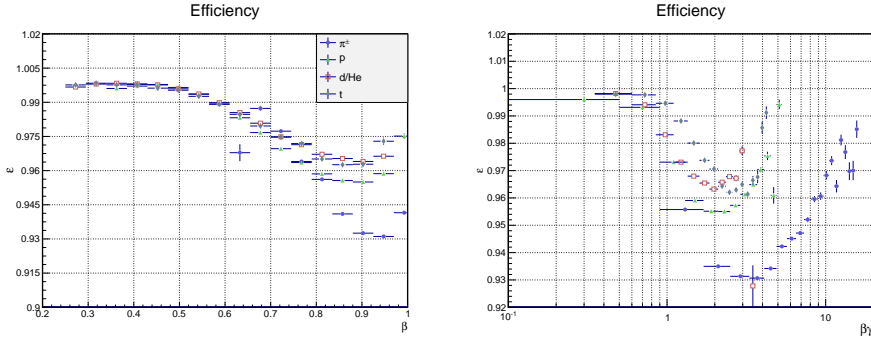


Figure 4.16: RPC efficiency estimated as a function of β and $\beta\gamma$ for pions, protons, deuterium/helium and tritium. The efficiency trends to the same value at low β whereas at high values it is scaled, following their rest masses in increasing order: higher mass-higher efficiency.

4.3.3 Time resolution - charge correlation

The median of the charge has been chosen as the representative variable to analyse the charge spectra as this estimator is less affected than the mean value by the tails of the measurements. The median of the measured charge is partially proportional to the number of clusters produced by the incident particle. Here, we present in the Fig. 4.17 and Fig. 4.18 the comparative between the median and the time resolution as a function of β and $\beta\gamma$. These two variables are inversely related. The median charge follows a trend similar to the Bethe-Bloch curve, showing the minimum between 2 and 3 for the sampled particles. The time resolution follows the opposite trend, and the maximum is located at the same place where the minimum ionisation point is. This behaviour is the expected one. However, as in the efficiency, we observe an unexpected dependence with the mass of the particles at the highest β . As the particles energy grows, the differences between the median charges and the resolutions for the different masses, became larger.

The origin of this effect can be that the multiplication and primary ionisation happen both at the same time and in the same gas volume. The energy transferred to secondary electrons that depend on the incoming momentum can affect the avalanche formation, reducing the required drift

distance needed to achieve enough energy to produce the next ionisation. At low momenta, as ionisation grows, the number of produced clusters inducing the signal in the electrode reduce the fluctuations in the signal. As it is shown, all the particles produce similar median charges and thus the time resolution behaves accordingly. As the energy of the incident particle grows, the probability of transferring enough momenta to secondary electrons and to produce further ionisations, without acceleration from the external electrical field, seems to reduce fluctuations in the time jitter. Moreover, once the maximum is reached, the time resolution starts to decrease as faster as heavier is the incident particle. In case of the lightest particles - pions, this decrease in time resolution is only of 8% from the maximum, at $\beta\gamma = 3$, to $\beta\gamma = 15$. The deuterium and tritium reduce their resolution in 10% just from $\beta\gamma = 3$ to $\beta\gamma = 4$. Furthermore, the median charge difference is of $\sim 50\%$ for pions and $\sim 14\%$ for the deuterium and tritium in the same $\beta\gamma$ ranges. Hence, if we assume that the charge is related with the number of primary clusters, the non-proportionality between the signal rising time and the median charge, together with the mass scaling, highlight the existence of extra contributions to the avalanche growth that reduce the fluctuation in the time.

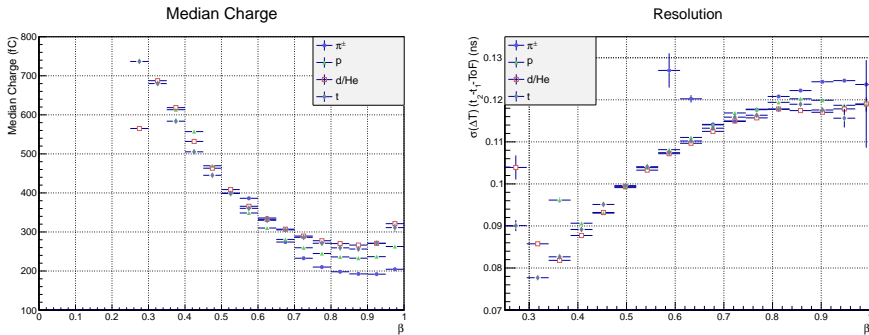


Figure 4.17: Median charge and time resolution as a function of the velocity for pions, protons, deuterium/helium and tritium. Both variables are inversely related.

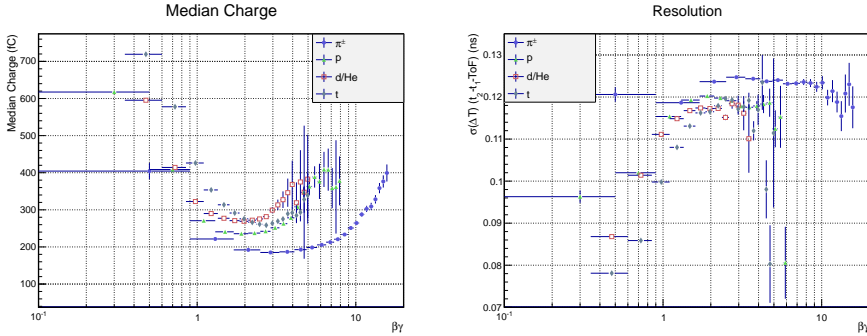


Figure 4.18: Median charge and time resolution as a function of the normalised to mass momentum for pions, protons, deuterium/helium and tritium. The inverse proportional behaviour is altered between the median of the charge and the resolution, showing extra contributions in the avalanche formation (see text for details).

4.3.4 Streamers probability and correlations with momentum

The mechanisms of streamer formation and the probability that an avalanche derive in a streamer discharge shows differences respect the behaviour of the charge, the resolution and the efficiency. The minimum production probability of streamers can be found at $\beta\gamma \simeq 1$. As in the previous cases, the distributions scale with the masses.

The streamer formation seems to be affected by two different contributions as can be deduced from Fig. 4.20. The first one is related to the avalanche size and, as this grows, the probability of streamer development also grows. This behaviour can be found at energies that present a charge above the measured at $\beta\gamma = 1$. The second region shows a linear dependence with momentum, independently of the particle type. The increase of the streamer fraction in this region is $\sim 0.44\%/GeV$. The linear dependence with momentum points to the secondary electrons produced in the ionisation as the responsible of the streamer formation.

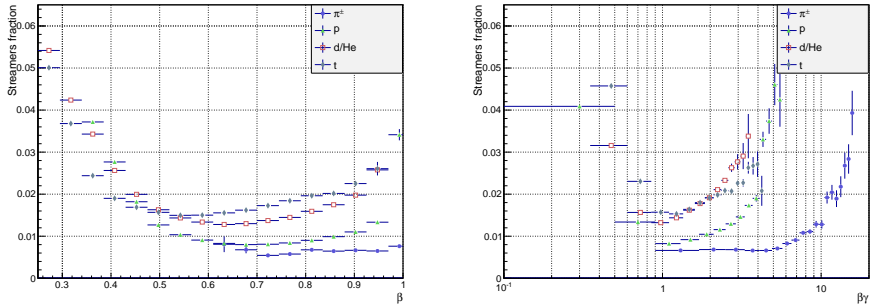


Figure 4.19: Streamer formation probability as a function of velocity β and normalised momentum $\beta\gamma$ for pions, protons, deuterium/helium and tritium. For $\beta\gamma < 1$ the probability seems to be independent on the mass whereas above that value, the probability increases with the mass.

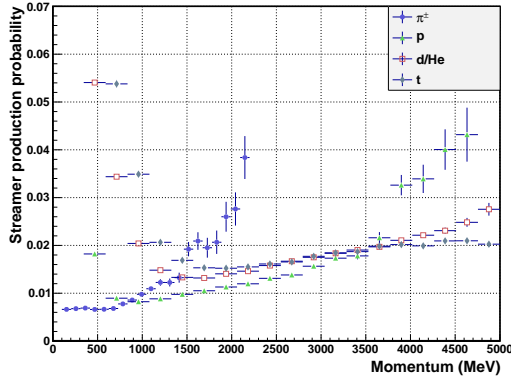


Figure 4.20: Streamer formation probability as a function of momentum for pions, protons, deuterium/helium and tritium. It seems that at momenta corresponding to the minimum ionisation regime, a linear dependence in streamer formation occurs, growing $\sim 0.44\%/GeV$, independently of the particle type.

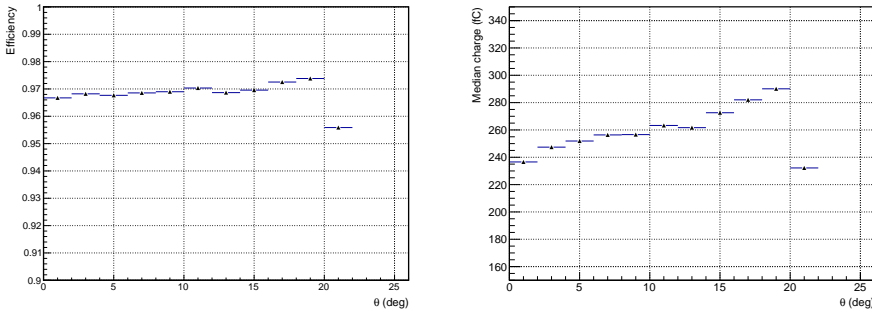


Figure 4.21: Efficiency and median charge of protons within the momentum range $800 \leq p \leq 1200$ as a function of the arriving angle at the RPC.

4.3.5 Dependence of efficiency and median charge with particle incidence angle

The previous charge analysis was performed selecting a narrow incidence angle range to avoid distortion of the results, because in HADES the angle distribution is particle type and momentum dependent. Both, efficiency and the charge depend on the number of primary ionisations in the gas. Thus, if the particle is arriving to the detector with an angle θ , the number of produced ionisations should scale as $1/\cos(\theta)$. On the other hand, the area of the electrodes affected by the avalanche grows as $\sin\theta$. Both effects should make the induced charge proportional to $\tan\theta$. Fig. 4.21. shows the efficiency and the median charge as a function of the incoming particles angle. To minimise effects coming from a non uniform momentum distribution protons with $800 \leq p \leq 1200$ MeV were selected.

Protons arriving with 20° show 1% more efficiency and 19% more charge than those with normal incidence.

Unfortunately, only data with small angles (less than 25°) are available and to extract any further conclusion is not possible. To improve the understanding of the influence of the diffusion coefficient and efficiency gain on the charge as a function of the incidence angle, should be produced data in a broader range of angles.

4.3.6 Charge-time dependence

The mean charge-time dependence for each particle was already subtracted from this data during the calibration, explained in the Section 4.1.3.2. However, in accordance with the findings of the previous sections, we have seen that signal formation depends on the mass, momentum and arriving angle of the particle. Hence, it is interesting to explore how is performing the correction if we select particles in the low charge region ($100 \leq Q \leq 150$ fC) as a function of the momentum. The median of the Δt distribution defined previously in eq. 4.14, is the correction constant in the time of flight needed to suppress the charge influence. The time resolution, for this selection, shows that even for the same charge interval, i.e. the same charge-time correction constant following the usual method, its value differs as a function of momentum. Both dependencies are shown in the Fig. 4.22.

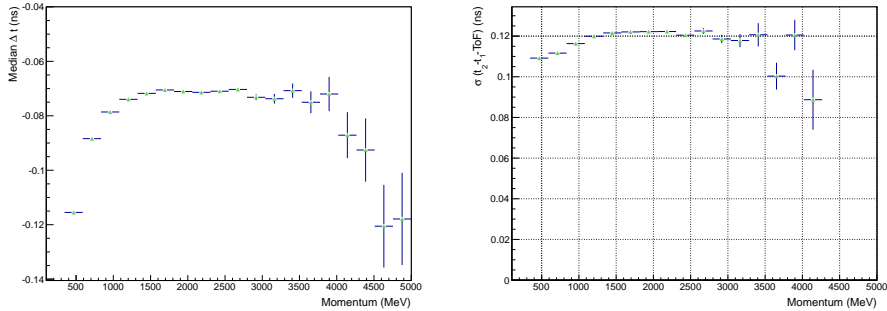


Figure 4.22: Median and resolution behaviour of the Δt distribution as a function of momentum for particles with charges in the $100 \leq Q \leq 150$ fC range. The dependence of the median value of the ΔT with the momentum shows the significant deviation of the slewing correction parameter. The resolution shows a different avalanche growth in different momentum regions.

The explanation of these plots goes hand in hand with the number of primary clusters produced in the gap. Out of the ionisation minimum, the number of produced clusters is enough to provide $\sim 100\%$ efficiency and good time resolution. If we suppose that these primary ionisations are Poisson distributed along the gap, there is always a probability of

not having an unbound electron close enough to the anode, capable of producing large signals. However, efficiency and resolution does not suffer from this effect as the number of growing avalanches is enough to reach the threshold with low fluctuations in time.

The slewing correction is the mean deviation in time for each charge value, neglecting the influence of momentum and particle mass. For a complete suppression of this effect, besides charge, the particle type and momentum should be included and this parameters produced. This fine correction is only possible after particle identification and cannot be accomplished using only the two layers HADES RPCs.

4.3.7 Efficiency, median charge, resolution and streamer probability for electrons

To finalise this section we show here a summary of the results of the analysis for positive and negative electrons. Due to the lack of statistics of these particles in the cocktail, the trend in efficiency and streamer fraction are not as clear as for other charged particles. The results are shown in the Fig. 4.23.

The median charge behaves as expected because in the HADES regime, where electron energies range between 100 MeV and a few GeV, energy loss take places by Bremsstrahlung, growing slowly with the momentum. This effect is also observed in the time resolution plot. In case of the efficiency, it would be expected also to grow with momentum. However, this effect is not visible in part because of the large statistics needed to get the value from the charge plot. Regarding streamer probability, neglecting the drop between 500-650 MeV, it follows a linear trend and the fraction of streamers increases $\sim 0.40\%$ in 500 MeV.

4.4 Double hit recovery

A RPC cell may have in HADES the chance of being hit by several particles within the time needed to perform the charge measurement of the first arrived particle. Here we analyse the case were two particles arrive during that time interval. There are two main different scenarios:

- The first arriving particle shadows completely the signal left by the

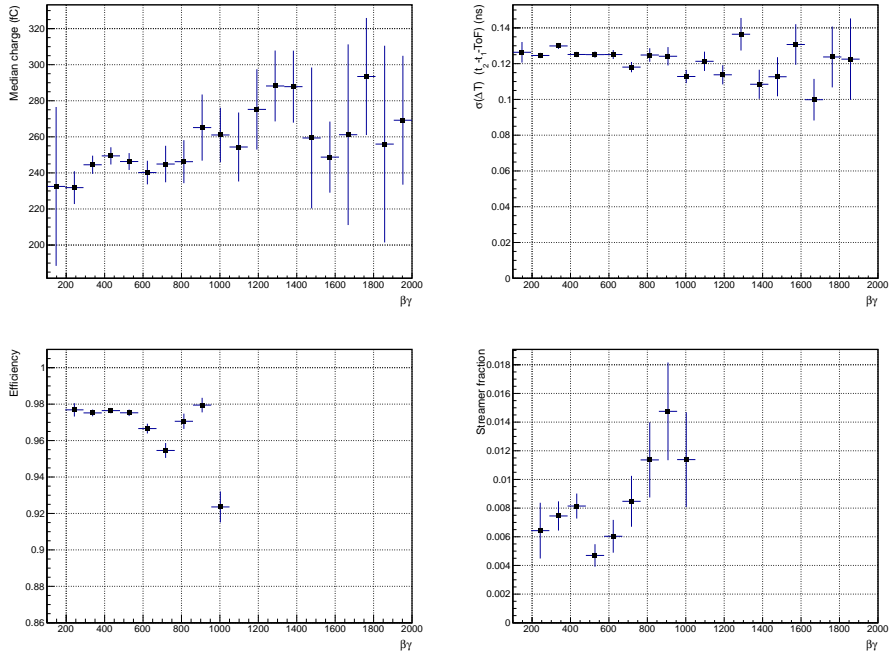


Figure 4.23: Median (top left), resolution (top right), efficiency (bottom left) and streamer probability (bottom right) for e^\pm as a function of $\beta\gamma$.

second particle in the case the induced signal reaches both cell ends before arriving the signals induced by the second particle.

- The signals induced by both particles arrive each one to different ends of the cell, screening the arrival of the remaining signals to the other end.

In the first case, the second particle is completely lost, and the charge information of the first particle is distorted by the induced current by the second particle which is also integrated in the same time window. Here, it is not possible to perform any algorithm to retrieve the second particle or correct the charge measurement of the first one.

The second case is shown in the Fig. 4.24. Here, the particle information can be partially recovered if the missing extra information provided

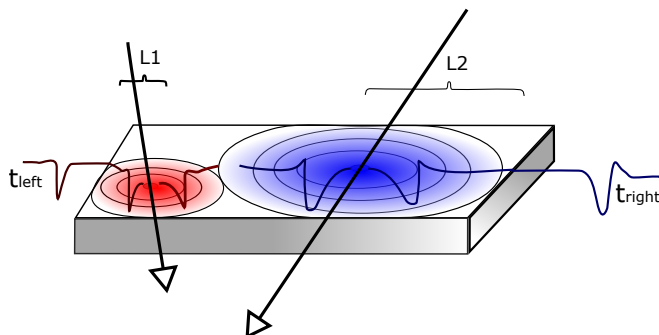


Figure 4.24: Double hit event in a RPC cell. The induced signal by both particles are shown in red and blue. The signal of the red particle arrives to the left edge and of the blue particle to the right. The distances travelled by both signals are L_1 and L_2 respectively. The arrival time and the positions of both particles with the extra information provided by the tracking system.

by other detectors is used. Two possible cases should be analysed separately. In terms of degrees of freedom, when two particles hit the same cell, 4 different measurements are required to successfully reconstruct all positions and times. As only two measurements are available, we need two extra data to perform the reconstruction. The first and more favourable case is that when the tracking can provide both positions in the cell. This case was analysed formally in D. González-Díaz Thesis [15], where both times (t_{left} , t_{right}) can be recovered by subtracting the signal propagation time from the measured times at both ends t_l^m , t_r^m respectively:

$$t_{left} = t_l^m - \frac{L_1}{v_s}, \quad (4.15)$$

$$t_{right} = t_r^m - \frac{L_2}{v_s}, \quad (4.16)$$

being $L_{1/2}$ the distance shown in the Fig. 4.24.

This solution is only suitable when we can trace two trajectories through a cell. Thus, a more general approach is needed in order to recover as much as possible double hits.

When only one track is available, the position information is not enough to disentangle the ambiguity between left and right signals. In this situa-

tion we have already three data and four unknown variables. The needed fourth datum may come from the momentum information of the track. Then, if we can assign a mass to one of the times, and it is compatible with the measured momentum, the time of flight of the particle can be unambiguously obtained. Thus, a condition of the form:

$$|t_{mom} - t_{l/r}^m| < n \cdot \sqrt{2}\sigma_t, \quad (4.17)$$

can be requested, being

$$t_{mom} = \frac{path \cdot \sqrt{p^2 + m_0^2}}{pc} + \frac{L_{1/2}}{v_s}, \quad (4.18)$$

n is the range of acceptance in sigma units, p is the momentum, $path$ is the particle's path length, c is the speed of light and v_s is the signal propagation velocity in the cell. The quantity $n \cdot \sqrt{2}\sigma_t$ is the range for accepting a time read out at only one side. We use $n = 3$ in our analysis.

4.4.1 Results of double hits recovery method

The method explained above was applied for three mass hypothesis: electron, pion and proton. If none of these masses filled the required condition, the track was skipped. The distribution of recovered particles as a function of both β and momentum is shown in the Fig. 4.25.

The increase in statistic achieved with this method is shown in the Fig. 4.26. Here, two different momentum ranges were selected. The first goes from 0 to 200 MeV and shows clearly the increase in both, the electrons and pions peak. Low momenta light particles reach in this momentum regime the maximum increase in statistics. Negative particles with momentum between 200 and 350 MeV also present an increase. However, the fraction between recovered and measured hits is smaller than in the previous momentum cut.

Globally, the impact of this algorithm in the matching efficiency as a function of multiplicity of the events is shown in the Fig. 4.27. It is important to stress out, that this matching efficiency does not have any cuts in momenta or fake track rejection and thus differs from the efficiency values showed in previous sections. An increase between 1 and 2 % is apparent.

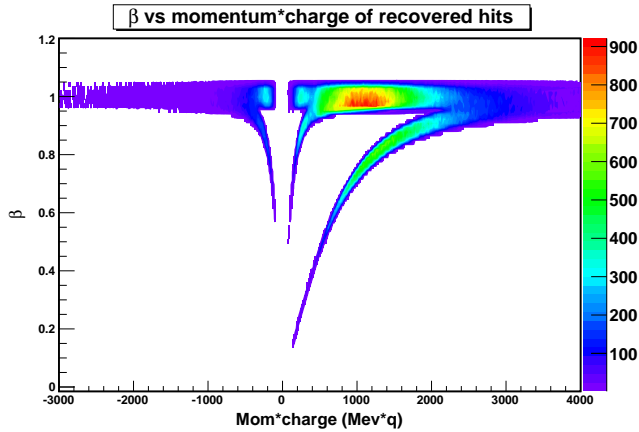


Figure 4.25: β vs momentum \times polarity distribution for recovered double hits events. Only e^\pm , π^\pm and p have been recovered

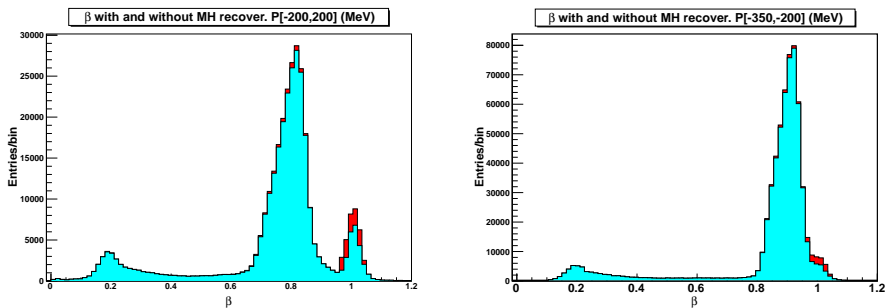


Figure 4.26: Recovered double hits particles in two momenta ranges (0-200) and (200-350) as a function of the velocity. Matched particles with tracking detectors which not needed the recovery method are shown in blue. In red are shown those particles which were recovered. The increase in statistics is apparent. Left: Distribution of particles as a function of velocity for momenta \times polarity between -200 and 200 MeV. Right: Particles distribution as a function of velocity for momenta \times polarity between -200 and -350 MeV. The peak in $\beta = 0.2$ is due to interactions happened within same START signal.

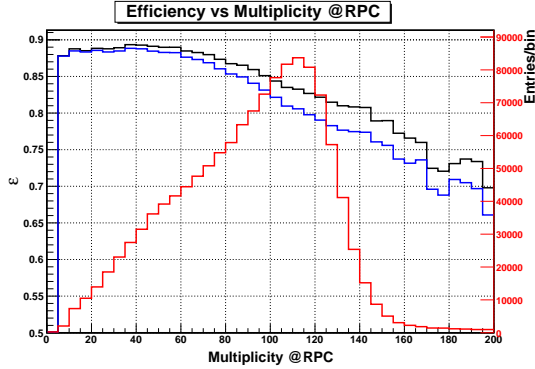


Figure 4.27: Matching efficiency with double hits recovery algorithm (black line) compared with the matching efficiency without the algorithm (blue line) as a function of multiplicity of the event. The improvement in the efficiency is around 1-2%. The red line shows the number of events analysed as a function of number of particles seen by the RPC detector (right side scale).

4.5 Conclusions

In this chapter the performances of the RPC wall have been analyzed using real data taken with the upgraded spectrometer in gold on gold collisions. The new setup made necessary to perform a new calibration of the detector and to improve the existing algorithms for using them with the new higher multiplicity environment. As consequence, new calibration were done on the position estimation and in the width to charge and the time of flight calibrations.

We have analysed the charges of the signals as a function of different variables and we have observed the very surprising and significant effect that, at very high velocities, they depend on the mass of the particle going through the detector. As the induced charge is a consequence of both the release of charges during the ionisation process in the chamber and the screening effect on the applied external electric field, some new effect could exist that depend on the mass of the incoming particle. We think that these effect is mainly a consequence of the momentum transferred by the particle to the secondary electrons in the gap. In any case, as it is an intrinsic properties of the detector that behaved in different way

for different particles and at different velocities close to the speed of light region, opens a lot of new possibilities that should be explored in the future.

As the charge of the signal is also related with the time resolution and the efficiency, this magnitudes are also influenced by the mass and the velocity of the particle. As a consequence, it is expected that further improvements could be done in the detector making a specific slewing correction for particles with different masses. As the mass of a track candidate is unknown until both the reconstruction and the particle identification process have been done, the slewing correction should be repeated once those processes have been finished. We estimate that an improvement of around $\sim 5-10$ ps could be reached.

5 Tracking with Timing: TimTrack

The determination of the trajectory of a particle which has left footprints in several detectors can be performed using different methods or algorithms. Usually, one tries to improve the quality of the reconstructed positions at each detector and combine these coordinates in a trajectory. At the same time other important parameters of the motion of the particle can be deduced as, for example, the velocity or momentum. Usually both processes are done in sequential steps, and in first place only the geometrical projection of the particle's path is done, adding the temporal information in subsequent interactions of the algorithm.

This approach has an important historical reason as the detection is performed either by timing or position sensitive equipments. Nevertheless, systems which can offer an accurate position and time measurement are now available [65],[66] and are of great interest because of the simplification and reduction of elements needed to track particles trajectories. Thus, to take advantage of the extra information, timing is used from the beginning of the fitting process modelling the particle's path including its motion. In this chapter, in the Section 5.1, is introduced the TimTrack's concept, that we are developing which is the abbreviation for Timing-Tracking. Then, in the Section 5.2, is described the mathematical formalism, based on Least Square Method, that underlies the whole concept and some examples are shown to illustrate how to build a model or the matrices which connect from detector's output and the fitted track parameters. In the Section 5.3, the TimTrack algorithm is used to re-fit trajectories in the HADES spectrometer, in order to show an implementation in a real experiment. Finally we conclude this chapter outlining the strengths and weakness of the method.

5.1 Take advantage of timing detector for tracking

The determination of the motion parameters of particles is one of the most important issues in an experiment and should be analysed in detail before choosing a suitable design of the detectors. To illustrate the importance of the time measurement let suppose a ideal detection system consisting of five planes placed perpendicular to the incidence direction as shown in the Fig. 5.1 and a flux of 200 particles in a interval of time T with random incidence angles and positions. In this scenario, the registered time by the detector planes is essential to perform a clean separation of particles tracks. The Fig. 5.2 shows the measured positions in the x, y, z and in the x, y, t reference systems. In this picture can be appreciated the difficulty of finding tracks in the case where time is not taken into account, and how this dimension can shed light in a priori complicated picture.

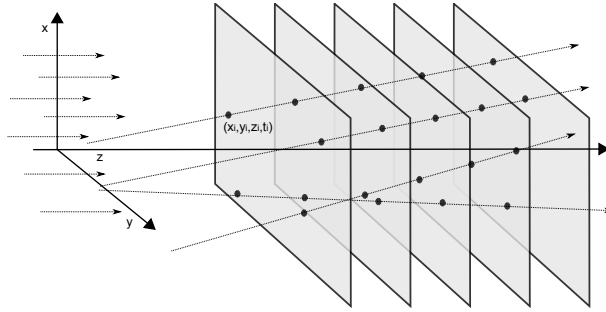


Figure 5.1: Example of 5 ideal planes able to measure both the position and the time.

In this scenario, we introduce the TimTrack algorithm[67]. The philosophy of the method is to work directly with the output of the detectors avoiding conversion of the measured variables (e.g. time) into other variables (e.g. position) with loss of relevant information. The main idea is resumed in the Fig. 5.3, where the data \mathbf{d} and a model $\mathbf{m}(\mathbf{s})$, which describes the data, are fed the algebraical engine of the method to provide the set of data, called saeta¹ (**s**mallest **s**et of **d**ata) which best fits the model to the data. A particularity of the method is that the process minimise the functional in the parameters space of the vector \mathbf{s} . Besides the

¹saeta, from latin *sagitta*, arrow

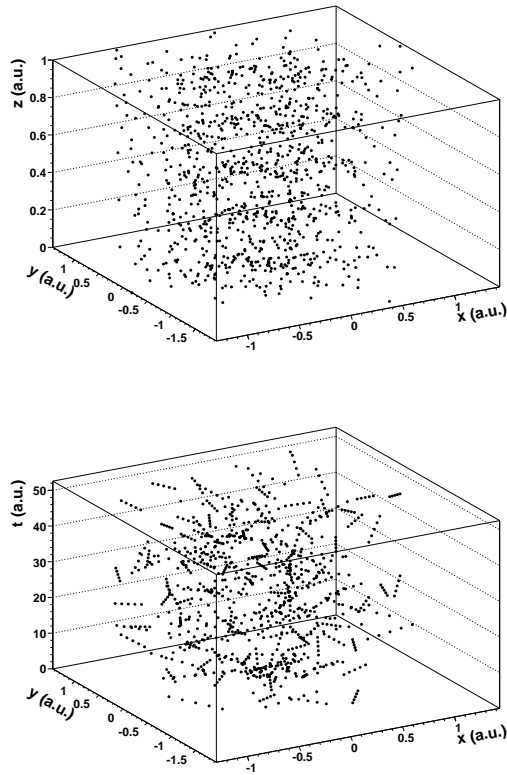


Figure 5.2: Top: Measured hit positions in x, y, z coordinates in an ideal detector. Bottom: Measured coordinates in the x, y, t reference system. The latter picture shows an intuitive track identification while the former presents difficulties.

fitted parameters, the method returns the variance-covariance matrix and the χ^2 of the fit naturally, as shown in the following section. Regarding the saeta vector, is composed by the minimum information needed to describe the trajectory of a particle:

$$\mathbf{s} = (X_0, X', Y_0, Y', T_0, V^{-1}), \quad (5.1)$$

where (X_0, Y_0) are the coordinates of the trajectory in the reconstruction plane, the (X', Y') are the slopes respect the x and y propagation axes, the T_0 is the time at which the particle crossed the plane and V^{-1} is the inverse of the velocity².

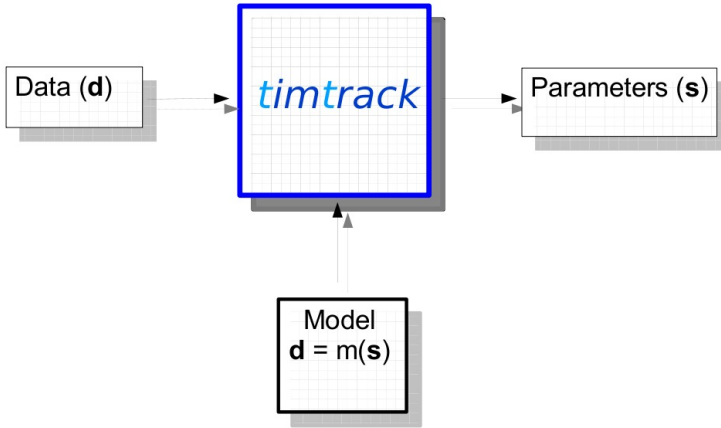


Figure 5.3: General scheme of the TimTrack algorithm.

Therefore the basic ideas that make TimTrack very different to other tracking or reconstruction algorithms are the following:

- Timtrack works always the six parameters defining the movement of a particle: two coordinates, two projected slopes, the time of the particle at a given reference plane and the velocity of the particle or its inverse (usually, working with the inverse makes most of the equations much easy to handle).

²The inverse of the velocity is sometimes referred as the slowness of the particle.

Working with all the given parameters make possible to include the relationships existing among them during the first stages of the reconstruction process. Other several processes like energy loss or multiple scattering, or constraints, like the vertex position or the mass, can be included in a very easy way at the beginning of the fit. All this features makes the algorithm more powerful and more sensitive to detecting ghost or wrong combination of data.

- TimTrack works with uncalibrated data allowing to include the calibration processes as part of the algorithm if enough data are available.
- TimTrack is formulated in a quite easy matrix formalism which handles in the same way parameters and calibration constants. It means that, at any moment, well known parameters can be fixed and the algorithm can be used to find the calibration constants or to analyze the possible correlations between them and the fixed parameters.

5.2 The χ^2 fitting in the parameter space

The Least Squares Methods (LSM) are widely as one of the most powerful and robust fitting methods. Their success is based on a simple implementation and the relatively common validity of the parabolic approximation when minimising close enough to the minimum. Moreover, it can be expressed in a clear and understandable way by using the matrix formalism. Therefore, following the notation of [67], bold letters are reserved to denote vectors and capital font for matrices and regular for constants.

The n_s parameters \mathbf{s} which best explain a set of n_d uncorrelated data \mathbf{d} using a model $\mathbf{m}(\mathbf{s})$ can be obtained by minimising the functional S defined as follows:

$$S = \sum_i^{n_d} \left(\frac{d_i - m_i(\mathbf{s})}{\sigma_i} \right)^2, \quad (5.2)$$

where σ_i is the incertitude associated to the i -term of the data vector. If $n_s \leq n_d$ is possible to calculate the set which minimise the functional S . In case $n_s = n_d$ the solution will be exact and analytical. The latter equation

can be expressed in a matrix form as:

$$S = (\mathbf{d} - \mathbf{m}(\mathbf{s}))' \cdot W \cdot (\mathbf{d} - \mathbf{m}(\mathbf{s})) , \quad (5.3)$$

where W is the inverse of the variance matrix V , or the weights matrix.

The set of parameters \mathbf{s} which best describes the model, according to LSM, is given by:

$$\frac{\partial S}{\partial \mathbf{s}} = 0. \quad (5.4)$$

The modelled data $\mathbf{m}(\mathbf{s})$ Jacobian matrix with respect to \mathbf{s}

$$\frac{\partial \mathbf{m}(\mathbf{s})}{\partial \mathbf{s}} = G, \quad (5.5)$$

can be used to expand $\mathbf{m}(\mathbf{s})$ linearly as:

$$\mathbf{m}(\mathbf{s}) = G \cdot \mathbf{s} + \mathbf{g}_0, \quad (5.6)$$

where \mathbf{g}_0 is defined as the difference $\mathbf{m}(\mathbf{s}) - G \cdot \mathbf{s}$. Thus, S can be expressed as a function of the matrix G and \mathbf{g}_0 as follows:

$$S = (G\mathbf{s})' \cdot W \cdot (G\mathbf{s}) - 2(G\mathbf{s})' \cdot W \cdot (\mathbf{d} - \mathbf{g}_0) + (\mathbf{d} - \mathbf{g}_0)' \cdot W \cdot (\mathbf{d} - \mathbf{g}_0). \quad (5.7)$$

This expression can be rewritten in a more comfortable way introducing the following definitions:

$$K = G' \cdot W \cdot G, \quad (5.8)$$

$$\mathbf{a} = G' \cdot W \cdot (\mathbf{d} - \mathbf{g}_0), \quad (5.9)$$

$$s_0 = (\mathbf{d} - \mathbf{g}_0)' \cdot W \cdot (\mathbf{d} - \mathbf{g}_0), \quad (5.10)$$

where K is always a square matrix with dimensions $n_s \times n_s$ called *configuration matrix* and depends only on the model and the variances of the measured data, \mathbf{a} compresses in a vector with dimensions n_s the n_d data and its called *vector of reduced data*, finally the s_0 is a scalar. Making the substitutions we arrive to:

$$S = \mathbf{s}' \cdot K \cdot \mathbf{s} - 2\mathbf{a}' \cdot \mathbf{s} + s_0. \quad (5.11)$$

If we apply the condition of the equation 5.4 to the expanded form of S , yields:

$$K \cdot \mathbf{s} = \mathbf{a}. \quad (5.12)$$

The matrix K , because of its definition is invertible, thus, the set of parameters \mathbf{s} which fulfils the minimum condition is given by the following expression:

$$\mathbf{s} = K^{-1} \cdot \mathbf{a}. \quad (5.13)$$

This is the general solution for the LSM method. Is noteworthy to mention, that the \mathbf{s} vector is connected to the measurements \mathbf{d} through the inverse of the matrix K , therefore, once this matrix is known, the needed steps can be resumed to calculate the vector \mathbf{a} and the scalar s_0 . The inverse of K , can be stored previously to afford computational time.

The variance-covariance matrix of the parameters are given by the inverse of the configuration matrix:

$$\mathcal{E} = K^{-1} \quad (5.14)$$

and the χ^2 is the value of S at the minimum \mathbf{s} .

If the model is linear with \mathbf{s} , \mathbf{g}_0 is a constant and the equation 5.13 determine the solution.

5.2.1 Non Linear TimTrack

On the other hand if \mathbf{g}_0 has a dependency on \mathbf{s} the solution should be obtained iteratively. Thus the expansion of S takes the following form:

$$S(\mathbf{s}) = \mathbf{s}' \cdot K_0 \cdot \mathbf{s} - 2\mathbf{a}_0(\mathbf{s})' \cdot \mathbf{s} + k_0(\mathbf{s}), \quad (5.15)$$

where

$$K_0 = G'_0 \cdot W \cdot G'_0 \quad (5.16)$$

$$\mathbf{a}_0(\mathbf{s}) = G'_0 \cdot W \cdot (\mathbf{d} - \mathbf{g}_0(\mathbf{s})) \quad (5.17)$$

$$k_0(\mathbf{s}) = (\mathbf{d} - \mathbf{g}_0(\mathbf{s}))' \cdot W \cdot (\mathbf{d} - \mathbf{g}_0(\mathbf{s})) \quad (5.18)$$

Let suppose a set of parameters \mathbf{s}_0 close to the minimum, thus the functional S can be expanded in a Taylor series around \mathbf{s}_0 as:

$$S(\mathbf{s}) \simeq S(\mathbf{s}_0) + \left. \frac{\partial S(\mathbf{s})'}{\partial \mathbf{s}} \right|_{\mathbf{s}_0} \cdot \delta \mathbf{s} + \frac{1}{2} \delta \mathbf{s}' \cdot \left. \frac{\partial^2 S(\mathbf{s})}{\partial \mathbf{s}^2} \right|_{\mathbf{s}_0} \cdot \delta \mathbf{s} + \dots \quad (5.19)$$

where $\mathbf{s} = \mathbf{s}_0 + \delta\mathbf{s}$ and the expansion at first order takes the following form:

$$S(\delta\mathbf{s}) \simeq \delta\mathbf{s}' \cdot K_0 \cdot \delta\mathbf{s} + 2(K_0 \cdot \mathbf{s}_0 - \mathbf{a}_0)' \cdot \delta\mathbf{s} + S(\mathbf{s}_0) \quad (5.20)$$

Therefore, the minimum condition of $S(\delta\mathbf{s})$ is verified by:

$$K_0 \cdot \delta\mathbf{s} + (K_0 \cdot \mathbf{s}_0 - \mathbf{a}_0) = 0, \quad (5.21)$$

from where the parameters $\delta\mathbf{s}$ can be obtained:

$$\delta\mathbf{s} = K_0^{-1} \mathbf{a}_0 - \mathbf{s}_0. \quad (5.22)$$

The sum of the parameters vectors \mathbf{s} and $\delta\mathbf{s}$ define

$$\mathbf{s}_1 = \mathbf{s}_0 + \delta\mathbf{s}, \quad (5.23)$$

and the equation which provides the solution takes the same form as in the equation 5.13:

$$\mathbf{s}_1 = K_0^{-1} \mathbf{a}_0. \quad (5.24)$$

This new value, closer to the minimum than \mathbf{s}_0 can be used to recalculate the matrices and vectors K , G , \mathbf{g}_0 and \mathbf{a} in order to obtain the next value \mathbf{s}_2 , where the process can be performed again. This result yields to a recursive equation, where the subindex- i refers to the number of iterations:

$$\mathbf{s}_i = K_{i-1}^{-1} \cdot \mathbf{a}_{i-1} \quad (5.25)$$

At some i -iteration, the $\delta\mathbf{s}$ will be approximately zero and thus the process stops. The exact criteria can be set as a function of uncertainties or do the iteration 3, 4 or n times. Usually convergence is reached in few steps and the largest values of $\delta\mathbf{s}$ are limited to the first two iterations.

The variance-covariance matrix of the parameters are given by the inverse of the configuration matrix as in the previous case:

$$\mathcal{E} = K_{i-1}^{-1} \quad (5.26)$$

5.2.2 Constrained TimTrack

The parameters of the \mathbf{s} vector are sometimes constrained by some physical or geometrical property. These relationships among parameters can be introduced in three different ways, where each has its own strong and weak sides. The simplest one is to redefine the set of parameters to include the relations. This solution has two weak sides, in first place the redefined parameter vector force to calculate a new more complicated Jacobian matrix of the model in case of non linear relationships, which should always be avoided as much as possible. In second place, the merging of parameters additionally entails the loss of the covariances and variances of the fused elements, discarding significant statistical information that might be useful.

Another solution is to extend the model to include these relations. In this case, a realistic weight factor should be introduced ad hoc in the W matrix. For example, if we know the interaction point (vertex) of the reaction and would like to introduce it as a model equation, its uncertainty will be given by the target's size.

The last possibility is to redefine the functional S , including a set of n_c functions $\mathbf{f}(\mathbf{s})$ which contain the constraints. Thus, the degrees of freedom are now $n_{DF} = n_d - n_s + n_c$. It is always possible to require the constraint functions satisfy

$$\mathbf{f}(\mathbf{s}) = 0. \quad (5.27)$$

The constraint functions can be used to extend the minimising function S by defining the Lagrange function as follows:

$$L(\mathbf{s}) = S(\mathbf{s}) + 2 \cdot \lambda' \cdot \mathbf{f}(\mathbf{s}), \quad (5.28)$$

where λ is an array of n_c Lagrange multipliers and the factor 2 was included for convenience later.

The constraint hypersurface keeps unchanged the value of L because of the condition 5.27, whenever the parameters fulfil the condition. However, outside the domain of the condition, the value of L is always $L \geq S$.

The minimum condition, as in the previous case is given by:

$$\frac{\partial L(\mathbf{s})}{\partial \mathbf{s}} = \frac{\partial}{\partial \mathbf{s}} [(\mathbf{d} - \mathbf{m}(\mathbf{s}))' \cdot W \cdot ((\mathbf{d} - \mathbf{m}(\mathbf{s})) + 2 \cdot \lambda' \cdot \mathbf{f}(\mathbf{s}))] = 0. \quad (5.29)$$

This equation can be solved in the general non-linear case by expanding both $\mathbf{m}(\mathbf{s})$ and $\mathbf{f}(\mathbf{s})$ in a Taylor series. Neglecting the high order terms of the expansion and the definition given in 5.6 we get:

$$\mathbf{m}(\mathbf{s}) \simeq \mathbf{m}(\mathbf{s}_0) + \left. \frac{\partial \mathbf{m}(\mathbf{s})}{\partial \mathbf{s}} \right|_{\mathbf{s}=\mathbf{s}_0} d\mathbf{s} = \mathbf{m}(\mathbf{s}_0) + G_0 \cdot d\mathbf{s} \quad (5.30)$$

and

$$\mathbf{f}(\mathbf{s}) \simeq \mathbf{f}(\mathbf{s}_0) + \left. \frac{\partial \mathbf{f}(\mathbf{s})}{\partial \mathbf{s}} \right|_{\mathbf{s}=\mathbf{s}_0} d\mathbf{s} = \mathbf{f}(\mathbf{s}_0) + R_0 \cdot d\mathbf{s}, \quad (5.31)$$

being the Jacobian matrix of $\partial_{\mathbf{s}} \mathbf{f}(\mathbf{s}) = R$ and R_0 its value at the $\mathbf{s} = \mathbf{s}_0$ coordinate.

The condition of the equation 5.29 verifies if

$$(\mathbf{d} - \mathbf{m}(\mathbf{s}_0))' \cdot W \cdot G_0 - \lambda' \cdot R_0 - d\mathbf{s}' \cdot G_0' \cdot W \cdot G_0 = 0. \quad (5.32)$$

Now, using the definition of $\mathbf{a}_0(\mathbf{s})$ and that $\mathbf{s}_1 = \mathbf{s}_0 + d\mathbf{s}$ we can rewrite the previous equation as:

$$K_0 \cdot \mathbf{s}_1 + R_0 \cdot \lambda = \delta \mathbf{a}_0, \quad (5.33)$$

where $\delta \mathbf{a}_0 = \mathbf{a}_0 - K_0 \mathbf{s}_0$. Following the same procedure as in the recursive case, the recursive solution of the constrained equations is given by:

$$\mathbf{s}_i = K_{i-1}^{-1} \cdot \mathbf{h}_{i-1}, \quad (5.34)$$

where \mathbf{h}_i was defined as $\mathbf{h}_i = \delta \mathbf{a}_i - R_i \cdot \lambda$.

Though the analytical solution is calculated, the elements of the \mathbf{s} vector require to know the value of the Lagrange multipliers, being thus useless. In order to obtain their values, we can propose the following set of equations, derived from the definition of the constraint function \mathbf{f} and the expression of the Lagrangian fulfilling the minimum condition from equation 5.33:

$$K_0 \cdot d\mathbf{s} + R_0 \cdot \lambda = \delta \mathbf{a}_0, \quad (5.35)$$

$$R_0 \cdot d\mathbf{s} \simeq -\mathbf{f}_0, \quad (5.36)$$

This equations can be used to extend the K_0 matrix, the vector $d\mathbf{s}$ and the vector $\delta\mathbf{a}_0$ as follows:

$$\underbrace{\begin{pmatrix} K_0 & R'_0 \\ R_0 & 0 \end{pmatrix}}_{\hat{K}_0} \cdot \underbrace{\begin{pmatrix} d\mathbf{s} \\ \lambda \end{pmatrix}}_{d\hat{\mathbf{s}}} = \underbrace{\begin{pmatrix} \delta\mathbf{a}_0 \\ -\mathbf{f}_0 \end{pmatrix}}_{\delta\hat{\mathbf{a}}_0}, \quad (5.37)$$

and the set of parameters and the Lagrange multipliers which best describe the data can be expressed as in the non linear case:

$$\delta\hat{\mathbf{s}}_i = \hat{K}_{i-1}^{-1} \cdot \delta\hat{\mathbf{a}}_{i-i}, \quad (5.38)$$

being $\hat{\mathbf{s}}_i = \hat{\mathbf{s}}_{i-1} + \delta\hat{\mathbf{s}}_i$

The error matrix associated to \mathbf{s} can be derived considering the set of the data at the minimum \mathbf{s}_m , thus the inverse of the \hat{K}_m matrix can be written as

$$\hat{K}_m^{-1} = \begin{pmatrix} K_m & R'_m \\ R_m & 0 \end{pmatrix}^{-1} = \begin{pmatrix} H_m & Q'_m \\ Q_m & Z_m \end{pmatrix} \quad (5.39)$$

and the product of these two matrices is the identity matrix with diagonal elements the sub-matrices I_{ss} and I_{cc} , where the sub-indexes ss and cc refers to the size of them, being $s = n_s$ (number of parameters) and $c = n_c$ (number of constraints):

$$\begin{pmatrix} H_m \cdot K_m + Q'_m \cdot R_m & H'_m \cdot R'_m \\ Q_m \cdot Z_m + Z_m \cdot R_m & Q_m \cdot R'_m \end{pmatrix}^{-1} = \begin{pmatrix} I_{ss} & 0_{sc} \\ 0_{sc} & I_{cc} \end{pmatrix}, \quad (5.40)$$

The Lagrange multipliers, can be therefore obtained as function of the vector $\delta\mathbf{a}$

$$\lambda = Q \cdot \delta\mathbf{a}. \quad (5.41)$$

It is important to stress that is not anymore $\hat{\mathbf{a}}$, as at the minimum, $\mathbf{f} = 0$. Using this relation for the multipliers, we can rewrite the minimum condition equation as a function of the matrices Q and R as

$$K \cdot \delta\mathbf{s} + R'Q \cdot \delta\mathbf{a} = \delta\mathbf{a}, \quad (5.42)$$

which can be regrouped as

$$\delta\mathbf{s} = K^{-1} \cdot (I - R' \cdot Q) \cdot \delta\mathbf{a} = K_c^{-1} \delta\mathbf{a}. \quad (5.43)$$

at the minimum $\delta\mathbf{s} \sim 0$, thus $K_m \sim K_{m-1}$ and the inverse of the K_c matrix is the error matrix.

5.3 TimTrack in a real spectrometer

The matrix formalism introduced in detail in the Section 5.2, has some interesting properties which allow to build the matrices whatever the model and set of measuring systems. One of the most interesting rules, is the additive property of the matrices K and a . If the measured data can be described by several models, whenever the initial parameters set remains the same, the matrices K and a can be obtained just as the sum of the respective matrices for each model/detector. Thus, in case we have a $s(x_0, x', y_0, y', t_0, 1/v)$ is a sufficient condition to calculate the Jacobian matrices of the models \mathbf{m}_i , follow the definitions given in the equations 5.8 and 5.9 to fill the K_i and a_i matrices, where the sub-index i refers to the number of the model or detector.

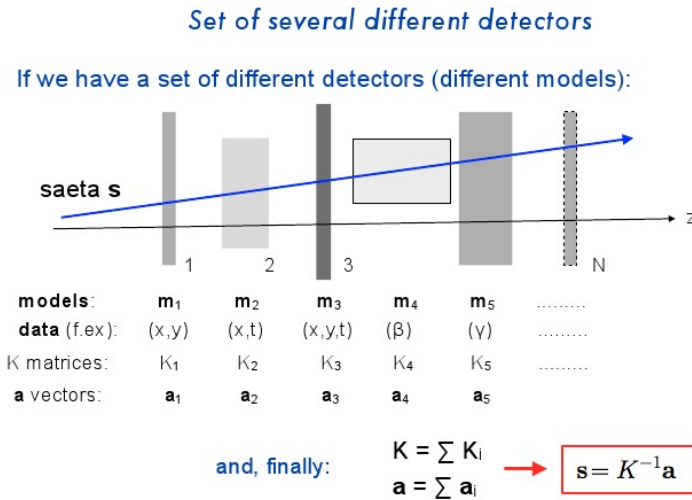


Figure 5.4: Scheme of the modelling of the matrices needed in the TimTrack algorithm. A set of position, time, energy sensitive detectors with their own models, data, K matrices and \mathbf{a} vectors. The saeta's parameters are obtained from the sum of all the individual K 's and \mathbf{a} 's, as they are additive.

In a general case, the measurement is performed by a combination of different detectors and techniques as shown in the Fig. 5.4. Each of them is sensitive to a specific dimension as time, energy or position, which are

used to obtain the fourth dimension: the information of the particle. As it was shown in the theoretical development of the LSM method, each model defines a complete set of matrices needed to perform the minimisation, being the \mathbf{s} given by:

$$\mathbf{s} = \left(\sum_n K_n \right)^{-1} \cdot \sum_n \mathbf{a}_n, \quad (5.44)$$

where n is the number of different models needed to describe the measurements.

The specific HADES spectrometer's design require at least two models to describe the tracking detectors (MDCs) and the timing (RPC and TOF). Momentum, requires a parametrisation of the magnetic field. The used model is described in detail in the following section.

5.3.1 Model

Because of the geometry of the spectrometer the coordinate reference systems can be referred to the whole system with origin in the target (laboratory reference system), to each sector (sector reference system) with origin on the target as the laboratory reference system, but with the y axis always at the center of the sector, and finally the module reference system, which is defined for each module or detector plane, where the x and y axis match with the natural longitudinal and transversal coordinates and being the origin placed in the center of the specified detector.

Though being equivalent the models in all the reference systems, the equations describing the measurement are system-dependent which for some geometries can turn in complicated non-linear expressions. Thus, it is important to choose the correct reference system for each model. In the MDCs case, it was decided to work always in the model reference system of each chamber, defining a \mathbf{s} vector at the centre of all the chambers as shown in the Fig. 5.5. Then, the four \mathbf{s} are constrained to a single track using a transformation of the coordinates and slopes to the sector reference system. The possibility of studying the behaviour of the parameters vector at the four chambers is an extra advantage introduced by this approach, otherwise it would not be possible.

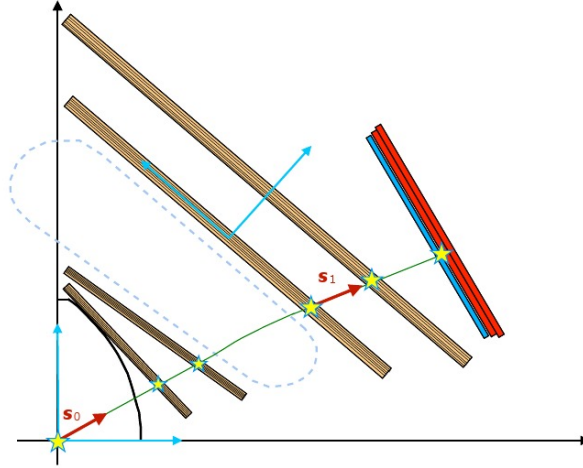


Figure 5.5: Schematic representation of a track reconstructed using multiples saetas. In this case the reconstruction is done by a minimisation in four different points located at each MDC plane.

Multiwire Drift Chambers model

Each MDC fired wire provides two data³: an transverse coordinate given by the spatial location of the wire and a time measured at one of the ends of the fired wire. The time measurement can be decomposed in four different terms:

$$t_{MDC} = T_0 + \frac{s}{V} + \frac{d}{v_d} + \frac{w}{v_s}, \quad (5.45)$$

where T_0 is the reference time, s/V is the time of flight from the reference plane to the plane defined by the particle's trajectory normal vector and the direction of the wire, d/v_d is the electron drift time and w/v_s is the signal propagation time along the wire. All the contributions and the geometry definitions are shown in the Fig. 5.6.

The distances s , d and w can be expressed as a function of the saeta's parameters as follows:

³Usually both data are reduced to a single one that should be iteratively improved.

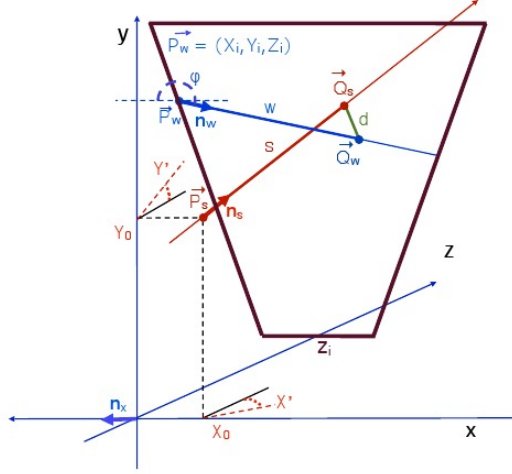


Figure 5.6: Multi wire drift chamber model for TimTrack. The track defined by $s(X_0, X', Y_0, Y', T_0, V_z^{-1})$, the path until the minimum distance to the wire is reached s , the drift distance d , the signal propagation distance w and the wire parameters n_w, φ, Z_i are shown.

$$s = \frac{z_i}{1 + (\sin \varphi X' - \cos \varphi Y')^2} \times [\mathbf{1} - (\sin \varphi X'_i - \cos \varphi Y'_i) \cdot (\sin \varphi X' - \cos \varphi Y')] \quad (5.46)$$

$$d = \frac{z_i}{\sqrt{1 + (\sin \varphi X' - \cos \varphi Y')^2}} \times [-\sin \varphi (X'_i + X') + \cos \varphi (Y'_i + Y')] \quad (5.47)$$

$$w = \frac{z_i [\cos \varphi (X'_i + X') - \sin \varphi (Y'_i + Y')]}{\sqrt{1 + X' + Y')^2} \cdot \sqrt{1 + (\sin \varphi X' - \cos \varphi Y')^2}} + \frac{z_i [(\sin \varphi X' - \cos \varphi Y') \cdot (X' \cdot Y'_i - X'_i \cdot Y')]}{\sqrt{1 + X' + Y')^2} \cdot \sqrt{1 + (\sin \varphi X' - \cos \varphi Y')^2}}, \quad (5.48)$$

where $Y'_i = (Y_0 - Y_i)/z_i$ and $X'_i = (X_0 - X_i)/z_i$. Notice the rotation introduced by the wire's angle φ .

In the general case, the model can be defined using the euler angles to define a free rotation of the wires of the MDC in the space and a

translational vector. However the introduction of two rotations more in the x and y axes would increase the non-linearity of the problem leading to an unnecessary complication of the model's Jacobian matrix and thus of the final solution.

The transversal coordinate provided by the wire geometry (the angle φ respect the horizontal axis and the end x_i, y_i, z_i) can be described as function of the saeta parameters as follows:

$$k_{MDC} = -(X_0 + X'z_i) \sin \varphi + (Y_0 + Y'z_i) \cos \varphi. \quad (5.49)$$

These models describe the minimum drift and signal distance between the track and the wire. However, in a drift chamber model the parametrisation of the drift velocity is particularly relevant as spatial and time resolution are closely related to the knowledge of the drift time. As it was already introduced in the Section 2.2, the geometry of the field far from the sense wire is highly asymmetrical. Thus, the first attempt to parametrise polynomially the drift time as a function of the distance to the wire was only suitable to describe the behaviour of the first MDC plane, where the cell has a square geometry. When the ratio width/height of the cell starts to increase, this approach starts to fail. Therefore, to overcome this problem a two dimensional parametrisation of the drift time, shown in the Fig. 5.7, based on the incidence angle and the distance to the sense wire is used as it is done in the standard procedure. However, the model requires the mean drift velocity v_d , which is obtained from the parametrisation as the quotient between the distance d and the incidence angle α in each iteration.

The signal velocity v_s is considered constant and of 250 mm/ns. The non zero probability of detection of a reflected pulse with time is:

$$t_{signal} = 2n \frac{L_w}{v_s} - \frac{w}{v_s}, \quad (5.50)$$

where n is the number of reflections and L_w is the length of the wire, is neglected.

Resistive Plate Chambers model

Each detected particle in a RPC cell provides five measurements: a left and right times (t_{left}, t_{right}) and charges (q_{left}, q_{right}) and the transversal

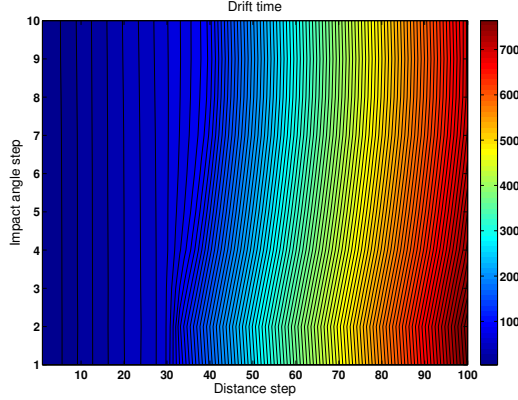


Figure 5.7: Parametrisation of the drift time (represented by the colour scale in ns) in a HADES MDC cell as a function of the impact angle α and distance d , both of them with discrete values dividing the interval of angles/distances in 10 and 100 values respectively. This parametrisation belongs to a chamber from the second MDC plane.

location of the cell in the detector (y_{rpc}) in the module coordinate system. The reference system and the observables are shown in the Fig. 5.8. Since the charge measurement has a high intrinsic variation because of the non proportional working regime, this quantity is not modelled as function of the saeta's parameters. The other measured values can be parametrised as follows:

$$y_{rpc} = Y_0 + Y' z_i, \quad (5.51)$$

$$t_{left} = T_0 + \frac{\sqrt{1 + X'^2 + Y'^2} z_i}{V} + \frac{X_l - X_0 - X' z_i}{v_s}, \quad (5.52)$$

$$t_{right} = T_0 + \frac{\sqrt{1 + X'^2 + Y'^2} z_i}{V} + \frac{-X_r + X_0 + X' z_i}{v_s}, \quad (5.53)$$

where X_l, X_r are the left and right ends along the x-axis of the cell and v_s is the velocity of the signal in the cell.

Magnetic field parametrisation

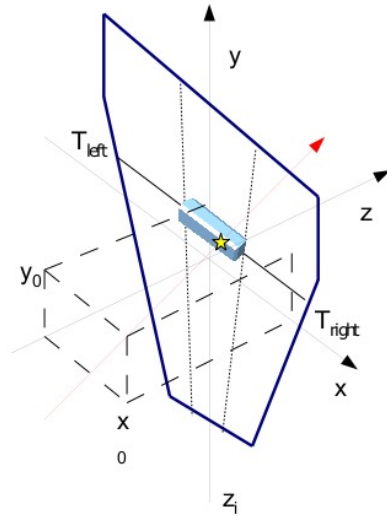


Figure 5.8: Measurement in a HADES RPC cell and geometry definitions.

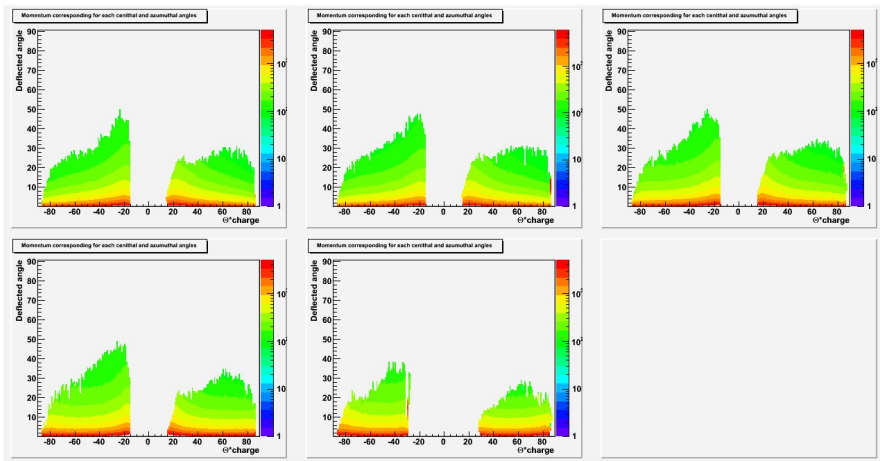


Figure 5.9: Momentum parametrization for the Tim Track algorithm. The momentum of the particle P is represented in the z -axis as function of the deflected angle θ (y -axis) and the angle θ before the magnetic field referred to the propagation direction- z (x -axis) for different φ angles starting from: $0^\circ - 5^\circ, 5^\circ - 10^\circ, 10^\circ - 15^\circ, 15^\circ - 20^\circ, 20^\circ - 30^\circ$.

The deflected angle within the magnetic field region, as seen in the Section 1.1.1.1 and 1.2.3.3 can be derived following different strategies as a parametrisation of the kick angle or solutions of the differential motion equations. Since trajectories of charged particles do not follow straight paths, the parameters of the \mathbf{s} vector are not enough to describe their motions. Thus the adopted strategy was similar to the kick plane. Considering that a particle with given initial parameters (X_0, Y_0, X', Y') and a momentum P will be deflected always in the same way, a map of these deflection angles as function of the initial parameters can be used.

The deflected angle θ was obtained by simulation of charged particles coming out of the interaction target using the PLUTO generator and connecting the output to GEANT. The resulting map of momenta is shown in the Fig. 5.9.

5.3.2 Method

The tracks for the TimTrack algorithm were obtained from the standard tracking procedure by reading the information of already analysed data. Since the HYDRA framework allows to access all data levels, the measured times and wire locations were used to fill the matrices according to the equations derived from the model.

The followed strategy begins building the analytical expressions derived from the MDC and RPC models. To obtain the initial parameters of the four reconstructed vectors, a simplified linear model, including only the fired wires positions is used. The accuracy of this first iteration is enough to provide an initial value for the non linear expressions which requires the positions, slopes, velocity and initial time at all the MDC planes.

Once the initial parameters are obtained, starts the non-linear procedure, where the full model for both detectors is used. Once convergence is reached over all the \mathbf{s} vectors, the matrices are expanded by the constraint equations which bind the solutions and add consistency among them. The Lagrangian functional is minimised and the output is compared to the input data, GEANT tracks in the simulated case, and the provided by the standard tracking in case of real measurements.

The distance travelled by the particle is computed considering a straight line between the target and the first two MDC planes. From the third MDC to the RPC is also considered to be a linear path. In the region where the

magnetic field is not negligible, the distance is computed using an ellipse approximation.

The analysis of the simulated data with GEANT was used to perform the detailed analysis of the performance of the method in a controlled environment. Once the desirable accuracy was reached with simulated data, the algorithm was used to refit beam data. These results are shown below.

5.3.3 Results

In this section, we compare the results of the *TimTrack* algorithm with both simulated and real data. The performance and quality of the method providing the trajectory at each MDC plane, time resolution, momentum resolution and velocity are shown.

The trajectory was reconstructed over each MDC plane while T_0 was calculated before and after the high magnetic field region in the second and third MDC plane. This parameter, however is not present in the real data, which were calibrated subtracting the left edge of the time spectra. In the real data analysis it is added a constant corresponding to the time of flight at speed of light following the shortest trajectory from the target to the MDC wire.

5.3.3.1 Simulation

The simulated data were generated using PLUTO and GEANT codes. The geometry of the emplacement of the detectors was the nominal and their responses close to ideal. Thus, this controlled environment is the best to investigate the performance and make corrections and fine tuning to the algorithm as trajectories and particle types can be accessed.

The main goal of the tracking system is to provide an accurate estimate of the bending in the magnetic field, in order to calculate the momentum of the particle. Moreover, an accurate reconstruction of the path is needed for a clean velocity reconstruction. In the Fig. 5.10 the resolutions in the X and Y axis are shown in the module reference system of the second MDC plane. The resolution was obtained by subtracting the reconstructed value from the generated parameter with GEANT.

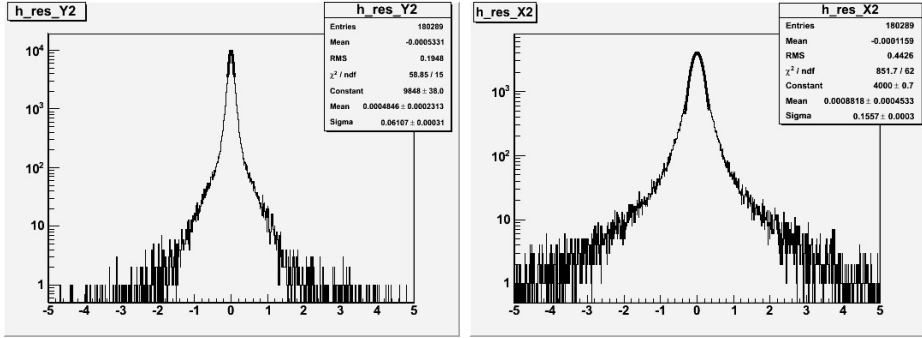


Figure 5.10: Spatial resolution provided by the TimTrack method in the second MDC plane. Left: X. Right: Y

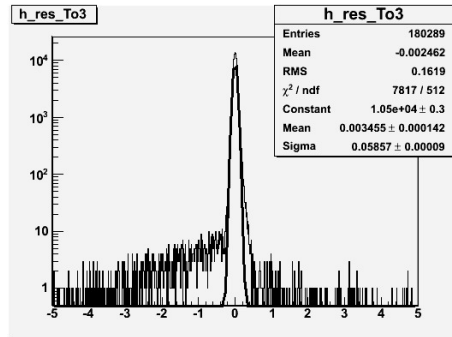


Figure 5.11: Time resolution provided by the TimTrack method in the second MDC plane.

The design of the chambers is optimised for measurements of the direction along the Y axis as is the main component of the deflected particle. From the diagonal of the K^{-1} matrix we also can extract the uncertainties. Depending on the number of fired cells we can find $46 \mu\text{m}$ and $100 \mu\text{m}$ for the Y and X respectively in the MDCs, with slopes of $6.0 \cdot 10^{-3}$ and $9.4 \cdot 10^{-3}$, which correspond to 0.34° and 0.54° . However, in the case only four layers had signal in the MDC, the resolution fall to $86\text{-}300 \mu\text{m}$ and $200 - 1000 \mu\text{m}$ for Y and X, and the slopes to $1 \cdot 10^{-2}$ and $3 \cdot 10^{-2}$ respectively.

These values from the K^{-1} matrix are in concordance with distributions obtained comparing reconstructed positions with GEANT. Timing resolution is around 79 ps, which is consistent with the error introduced in the W matrix of 80 ps. The $T_0 - T_{GEANT}$ distribution is shown in the Fig. 5.11, where the sigma from the Gaussian fit is 59 ps, a value 20 ps lower than in the K matrix. It can be explained by the non introduction in the W matrix of the improved resolution in the case where two cells are merged in one cluster in the RPC.

Regarding momentum resolution of the method, it was obtained for leptons and protons in three different regions: below 1 GeV, between 1 and 2 GeV and over 2 GeV. The Fig. 5.12 shows the resolution for leptons in these regions, being always below 2.5 %. Protons, have better resolution in general, being in the worst scenario ($P > 2$ GeV) around 2%.

The path length shows a good agreement between the standard fitting method (Runge-Kutta) and the TimTrack, as shown in the Fig. 5.13, being the rms of the distribution around 1.25 mm.

Finally, the χ^2 distribution as a function of the momentum of tracked particle is shown in the Fig.5.14. The presence of large χ^2 values at lower momenta is expected because of the multiple scattering and energy loss effects.

5.3.3.2 Real data

The test with real data can only reveal the validity of the method and used models. For that purpose, measurements from the November 2010 experiment were used to check the method. Unlike the simulated data, the exact motion parameters of the particles are not available and the results are compared to the standard tracking, i.e. Runge-Kutta.

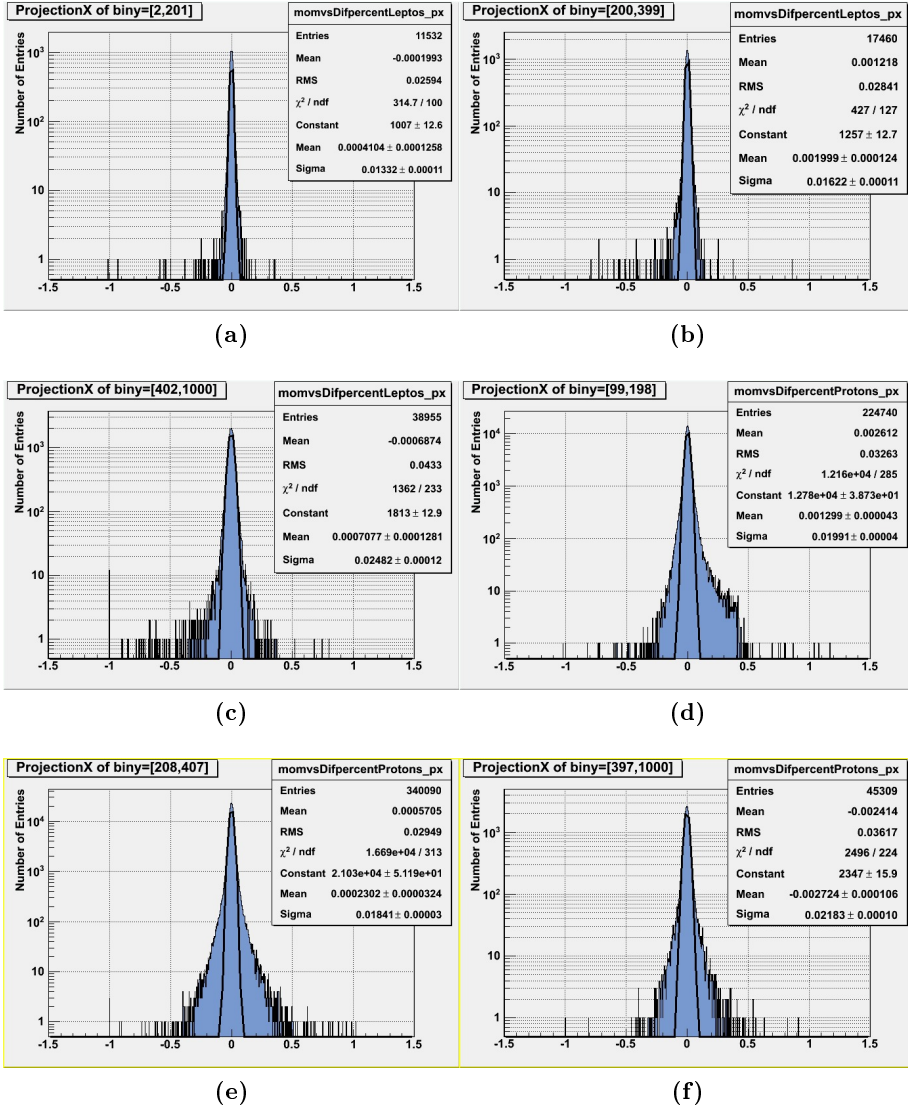


Figure 5.12: Momentum resolution for simulated leptons and protons. Leptons: (a) $P \leq 1$ GeV (b) $1 < P \leq 2$ GeV. (c) $P > 2$ GeV. Protons: (d) $P \leq 1$ GeV (e) $1 < P \leq 2$ GeV. (f) $P > 2$ GeV.

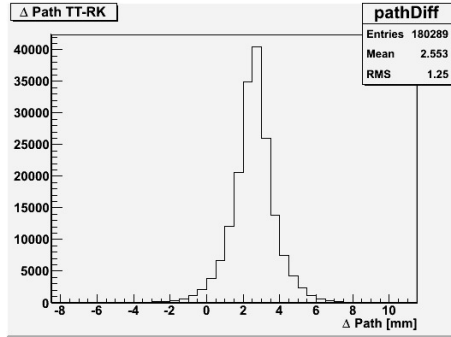


Figure 5.13: Difference of the TimTrack and Runge-Kutta particle's path.

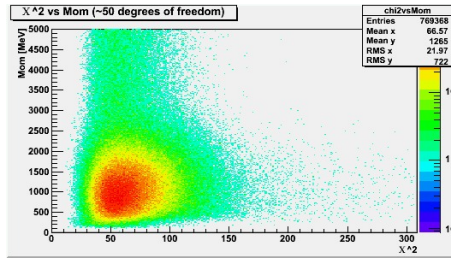


Figure 5.14: χ^2 vs momentum distribution for simulated data analysed with TimTrack method.

Observables coordinates can be estimated comparing the expected and measured times. In that sense, keeping in mind that the drift velocity in the MDC cells is about $30\text{-}40 \mu\text{m}/\text{ns}$ [52], from the $t_{meas} - t_{exp}$ (being t_{exp} defined in eq. 5.45) spectra shown in the Fig. 5.15 we can obtain the approximate position resolution. The number of wires participating in a cluster also is related with the position accuracy. Therefore the position uncertainty for a cluster with 6 layers would be $(40 \mu\text{m}/\text{ns} \cdot 4 \text{ ns})/\sqrt{6} = 65 \mu\text{m}$, taking the average rms from the Fig. 5.15. The different distributions showed in that figure is due to constraint equations between the RPC TOF and the T_0 in the modules 2 and 3. As the first and fourth chamber are also related to the same T_0 , a significant part of the mismatch is attributed to these chambers.

Other important parameters in order to measure the quality of the reconstructed trajectory are the path length and the difference in momentum,

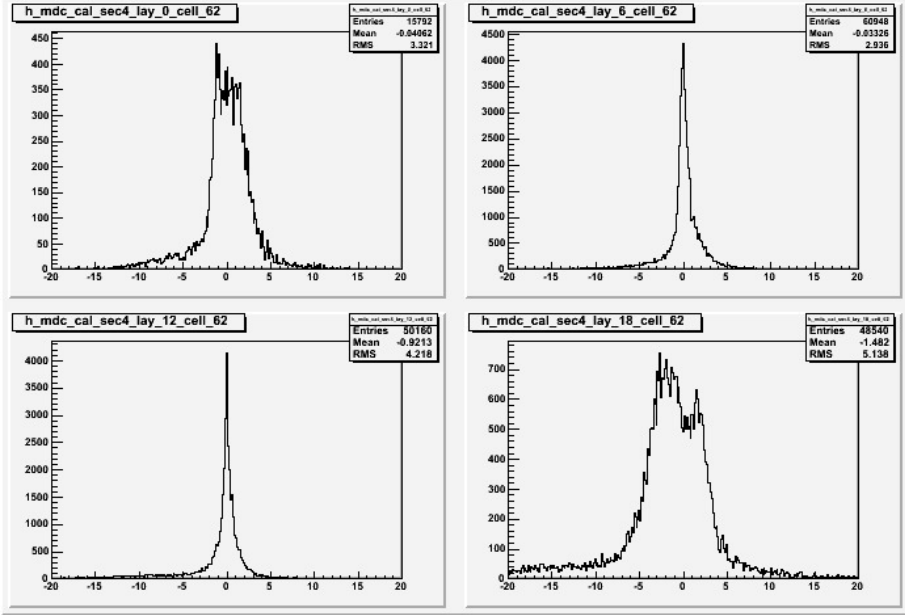


Figure 5.15: Distribution of measured-expected times in the four MDC planes. Starting from the top-left: MDC Plane I, top-right: MDC Plane II, bottom left: MDC Plane III and bottom right: MDC Plane IV.

both between the Runge-Kutta method and the TimTrack. These two distributions are shown in the Fig. 5.16. From the path difference we can obtain the impact on the reconstruction of the velocity of the particle. Taking into account that the mean path length in the HADES spectrometer is around 2100 mm, a 3rms deviation would have an impact of 0.6%, if the measured time of flight is ~ 9 ns. The distribution describing the momentum quality, $(P_{TT} - P_{RK})/P_{RK}$, shows a rms value around 5.8%, which is not as good as in the simulation analysis, where always resolutions below 3% were achieved. This origin of this discrepancy have its origin in the way the magnetic field is parametrised and the strong geometrical constraints on the position of the detectors. In the real data, these emplacements differs slightly from the ideal one and thus a deviation in the accuracy of the momentum reconstruction is expected. To overcome this issue for each experiment is needed a dedicated production of the parametrisation of the

field.

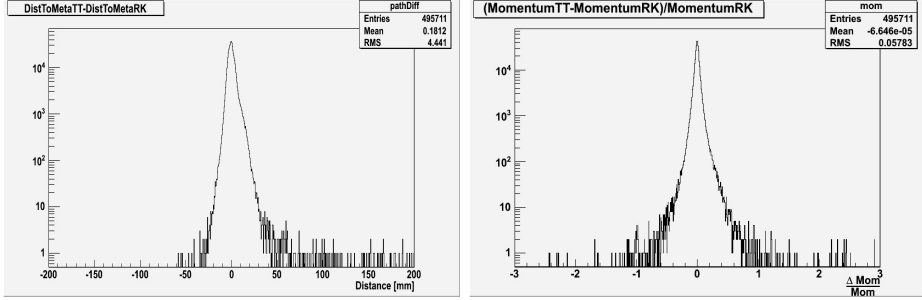


Figure 5.16: Differences in reconstruction between Runge-Kutta and TimTrack methods. Left: particle’s path from TimTrack - Runge-Kutta. Right: $(P_{TT} - P_{RK})/P_{RK}$ distribution.

Another parameter which includes both the momentum reconstruction and the velocity is the mass. The comparative results between Runge-Kutta and TimTrack are shown in the Fig. 5.17. This mass uncertainty is consistent with the previous obtained value of 5.8%.

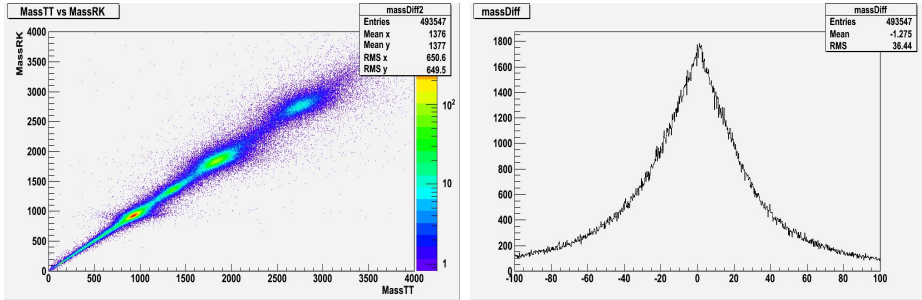


Figure 5.17: Differences between Runge-Kutta and TimTrack methods reconstructing the particles mass. Left: reconstructed mass from Runge-Kutta vs reconstructed mass from TimTrack. Right: Difference between the reconstruced masses using both methods.

Finally, the last plot of the comparison between both methods is qualitative: the β versus momentum distribution is shown in the Fig. 5.18.

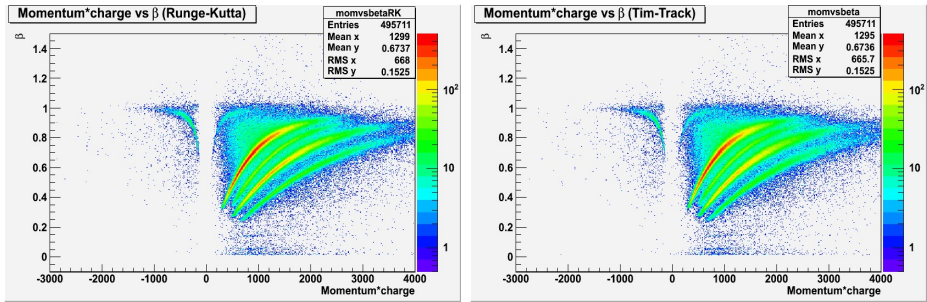


Figure 5.18: Comparative between distributions of β vs momentum for TimTrack and Runge-Kutta. Left: TimTrack. Right: Runge-Kutta

5.3.4 Performance

The TimTrack algorithm tested with HADES data is still a concept proof and many of the details of the code and the model are not fully optimised. The reduction of the parameters and selection of the most relevant constraints could be on the right direction in this regard. From the computational point of view the heaviest part of the algorithm are the matrix operations. The required time to perform these operations grows exponentially with matrix size being of the order of $5 \cdot 10^{-5}$ s for $n=20$ and of 10^{-5} s for $n=10$ respectively[106]. Taking into account that operations as inversion are performed at each iteration, around of 75% of all the computational time is spent in these operations.

The task runs at around ~ 400 tracks/s for the complete procedure, from the filling of the matrices of the simplified model in order to get a starting minimisation set of parameters until the method returns all the saeta's parameters and the quality of the fit. These values are computed for a set of 20 parameters, which were of special interest to investigate performance, resolution and minimisation, and can be reduced substantially in further versions of the code down to 10 with a consequent speed improvement.

5.4 Conclusions

The TimTrack algorithm was thought to be the tracking system of the TRASGO detector. Here we have shown how the same philosophy can be used in other systems such as the HADES spectrometer. Of course it is not

the optimal application case, because of the limited time resolution of the tracking detector. However such approach may be useful in high multiplicity environments where matching became a problem. Even time resolutions at the 1 ns scale of the tracking systems should be enough to suppress significantly ghosts and fakes, reducing thus candidates. Moreover, its understandable mathematical development makes the method suitable for implementation in other systems where timing detectors are involved.

TimTrack offers a very powerful paradigm for the reconstruction of particles in Particle Physics and Nuclear Physics experiments. As the algorithm includes all the parameters informing about the motion of a particle (coordinates, direction, time and velocity) it allows to include as a constraining any relationship between the parameters making the reconstruction more powerful and accurate. Also the calibration parameters can be included in the algorithm making easier to find the possible correlation between them and any of the fitted parameters.

As *TimTrack* includes all the parameters and calibration constraints in the algorithm, it is, in principle, more powerful than any other algorithm. The price to pay is working with more complicated formulae and in a higher dimension parameter space. By this reason finding the minimum may require to be closer to it or to develop, for each case, the specific tools. Of course, the approach is optimum when the time plays a relevant role and there are, in the experimental setup, detectors with very good time resolution. As consequence, a lot of work is in front of us to make the algorithm competitive with other algorithms like the ones used commonly in most of the experiments.

Another advantage inherent to the *TimTrack* algorithm is that, as it deals with all the parameters describing the movement of a particle, any constraint related with them can be included in the fitting model. For instance, the relationship analysed in the previous chapter that relates the charge of a signal with the mass of the particle and its velocity could be introduced in the fitting model and use the charge measurement to improve significantly the fit.

We showed one example about how to apply the method to a typical detector as a drift chamber. We show how our algorithm allowed to make a fit with a dramatic gain of degrees of freedom although this feature did not allowed to get very much better results. One reason is that the layout of the detector was not optimized to take advantage of our algorithm. In some

sense, we were applying it to a detector having a design appropriate to be use with the traditional methods. Another reason is that TimTracks, as it deals directly with times, need a very good synchronization; although we did it, perhaps more data would be necessary to get appropriate calibration times in all the channels.

Concerning the problem of inverting matrices, this drawback can be avoided using a recursive method, that is now under development.

6 RPC-ToF wall as a cosmic ray detector

The RPC technology is not new in the realm of Cosmic Ray physics. The first built Resistive Plate Chambers found their utility in measuring secondary particles showers fronts in experiments as GREX/COVER_PLASTEX at Haverah Park[107] or ARGO-YBJ [108], offering high performance at low price. This first detectors were designed in the eighties and allowed measure with enough accuracy the density and the arrival time with around 1 ns time resolution.

The modern RPC detectors improved the time accuracy of the first models and the resolution offered nowadays is usually ranging between 50 and 100 ps. Analogue and digital electronics progress together with new integrated acquisition boards as the TRB [21] made this detectors as one of the best choices for building time of flight walls in nuclear and high energy particle physics. This is corroborated by the spread of the technology already commented in the Section 3.2.2.

In this chapter, we present the results of the analysis of the data taken in 2009 during the commissioning of the HADES RPC wall carried out with cosmics [101]. The measurement of the cosmic rays with RPC detectors seem to show that a small volume detector, with good position granularity and a time resolution of the order of ~ 100 ps, would allow to estimate the rates of primary cosmic rays at different energy intervals and, as consequence, estimate the contribution of the different effects to the behaviour of this rate.

In the first part of this chapter we will overview some general concepts on cosmic rays physics, the influence of the atmosphere and a model which describes extended air showers as function of the energy of the primary, the density and the arriving time standard deviations. Then, some parameters as arrival angles or energy of the electrons and muons of the shower were studied using simulation techniques. Furthermore, is derived a method for the incident shower angle reconstruction using the direction information of particles.

The second part is devoted to the analysis of the acquired data with

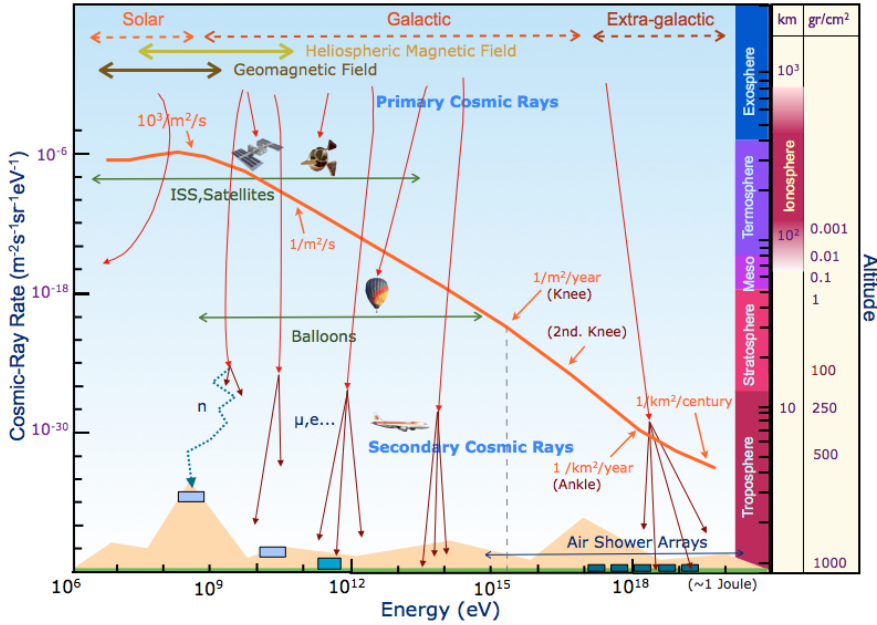


Figure 6.1: Cosmic ray energy spectrum

HADES RPC TOF wall in 2009. We show the methods used for calibration, synchronisation and event front reconstruction. A comparative study of the reconstruction following the usual methods in cosmic ray physics and the results derived from the particles direction is also shown. In addition, the particle fluxes during the data taking are presented. Finally, the parametrisation of the energy of the primary particle as a function of the time spread of the particles and the density is obtained from the data.

6.1 Introduction

Since the discovery of the cosmic rays one hundred years ago, there are still many significant questions and unknowns about them. Despite contributions made for the understanding of the nature of the matter and the phenomenology of the arriving cosmic radiation to Earth, the underlying mechanisms of the production and acceleration processes of those with the

highest energy is still unknown.

The main flux of cosmic rays impinging the Earth atmosphere consists of protons, light and heavy nuclei with energies up to 10^{20} eV. This primary particles produce the so called secondary cosmic rays when collide with the matter surrounding our planet and these particles may reach and been detected at the Earth surface. Depending on their energy, the cosmic rays are affected either by the solar wind, the planetary and terrestrial magnetic field or the atmosphere allowing the analysis of those effects.

Regarding the origin of these high energy particles, most of those which have energies below few GeV are produced mainly in the Sun and arrive to the Earth surface as a part of the solar wind. Sometimes, during massive ejection of matter from the Sun called Coronal Mass Ejection, protons can reach tens of GeV, or event ~ 100 GeV. For energies above 10^{10} GeV and up to 10^{17} - 10^{18} eV, the primary cosmic rays are produced in our galaxy. Taking into account the size and the galaxy's magnetic field we may assume that below these energies, cosmic rays are unable to leave and are confined in our galaxy. Above these energies, the origin can only be explained if it is extragalactic[109].

Fig. 6.1 shows the flux of cosmic rays arriving to the Earth surface as a function of their energy. Below few GeV, most of the cosmic rays are produced in the Sun and hence, the flux depends on the solar activity. At these energies and up to $\sim 10^{15}$ eV, cosmic rays are measured either using detectors placed in satellites or in balloons. Above that energy, the rate of primary particles became so scarce that for measuring it, ground based large arrays of detectors are needed.

The flux of particles arriving to Earth is not constant, and as the low energy particles flux which variates with Sun's activity, the more energetic cosmic rays up to 10^{17} eV are modulated by solar wind and are partially screened. This effect is enhanced during the Coronal Mass ejections which screens the galactic cosmic rays and a significant decrease is observed. This effect was first documented by S.E. Forbush [110] and is named after him as Forbush decrease.

Besides modulating effects of the cosmic radiation by the Sun or the magnetic fields, the radiation which reach Earth interact with all the time changing atmosphere. Temperature and density effects were reported for the first time at the thirties of the last century and were analysed by A. Duperier in [111], who documented the correlation between the intensity

and the temperature of the atmosphere and the seasonal variation. This correlation was also reported for the rate of muons measured deep underground, at ~ 1 km depth in the MACRO experiment [112].

In 2009 the correlation between atmosphere and muon flux underground was measured precisely by the MINOS experiment at the SOUDAN mine in Minnesota [113]. They have found that the effective temperature of the atmosphere, defined as a weighted average that takes into account the distribution of altitudes where the mesons which cause the measured muons occur, is closely correlated with the muon flux at 700 m underground. This depth sets a muon energy threshold of $E > 700$ MeV.

6.1.1 Influence of the atmosphere in cosmic rays

Most of the aforementioned effects can be easily understood looking at how the secondary cosmic rays are produced in the atmosphere. Primary cosmic rays with energies above several tens of GeV arrive to the Earth atmosphere and collide with the atoms producing mainly nucleons and light mesons, as pions and kaons. All these particles may later either interact with other nuclei or decay producing other secondaries like muons, electrons and photons. Depending on the energy of the primary particle and, as a consequence, of the number and energies of the produced secondaries, the process may be repeated several times giving rise to an extended air shower (EAS). On the way towards Earth surface, some of the particles are absorbed in the air and the remaining arrive to ground and can be detected.

The atmosphere dynamics may affect the interaction of cosmic rays in several ways. When the temperature in the high atmosphere (above the tropopause, at ~ 15 km height) increases, the density decreases and so does the interaction probability. Then, cosmic rays have a bigger probability to penetrate deeper into the atmosphere and hence the total number of secondary particles including muons arriving to the ground tends to be bigger. On the other hand, when that temperature decreases, two competitive processes related with the muon production and with the probability that a muon arrives to the ground appear: pions (or kaons) produced in the high atmosphere either decay, producing a muon, or collide with a nucleus producing new particles of lower energy. Then, a muon produced in any of these processes may decay into an electron and a couple of neutrinos,

or may arrive to the ground.

The contribution of these processes have been very well studied in the past and have been recently updated by A.N. Dmitrieva in [114]. According to these authors all those effects can be summarized in a single weighting function $W_T(E_{min}, X, h, \theta)$, or DTC (Differential Temperature Coefficient), that informs about how much a layer of the atmosphere at a height h contributes to the change of the flux of muons arriving with a zenith angle θ , with energy greater than E_{min} , at an observation level X . Fig. 6.2 shows the behaviour of the Differential Temperature Coefficients W_T as a function of the atmospheric heights, for muons of different energies at the sea level, arriving vertically.

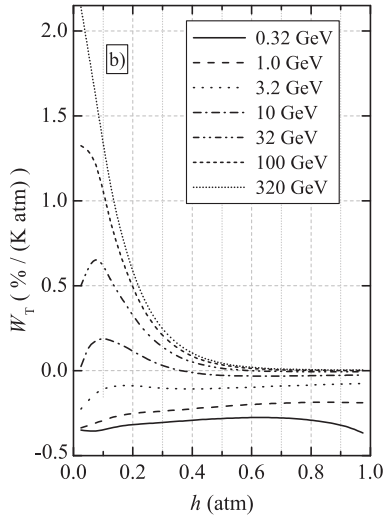


Figure 6.2: Differential Temperature Coefficients W_T as a function of the atmospheric height for muons arriving vertically to the sea level with different energies [114].

The behaviour of the coefficients show how the flux of the muons with the highest energies is very sensitive to the temperature of the stratosphere ($h < 0.2$ atm). Or, very small changes of the temperature of the stratosphere may affect very significantly the flux of high energy muons arriving to the ground. It means that, in principle, a detector being able to estimate the flux of the very high energy muons at the ground, together with an appropriate model of the temperatures profile on top of the detector (or

just the mean value of that profile measured previously) could be used to measure the changes of the temperature of the stratosphere. This is a very important challenge because it is well known how the dynamic of the low stratosphere affects dramatically the weather and the climate changes in the troposphere [115]. A good and a permanent watch of the variations of the temperature of the low stratosphere would allow to improve very significantly the mid and long term weather forecast.

6.1.2 The time and density microstructure of cosmic ray air showers

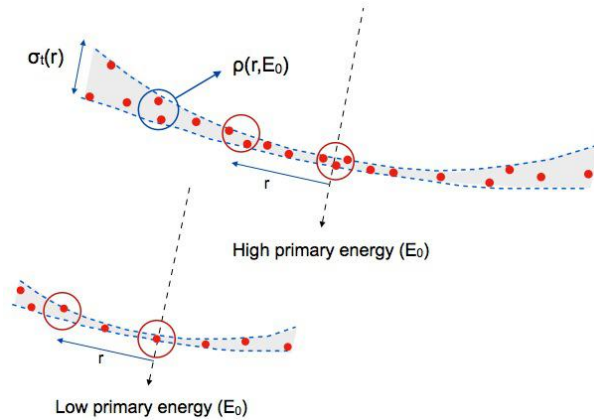


Figure 6.3: Comparison between time profile and density of two showers, one originated by a high energy primary cosmic ray and the second by a low energy one. The time width are function only of distance whereas density increases with the energy of the primary.

Shower transport along the atmosphere is also a well known process that has been well approximated using both accurate measurements and simulation programs.

The mean properties of the showers of secondary cosmic rays when they arrive to the Earth surface are well known. Some of the most representative are the following (see Fig. 6.3):

- The time width $\sigma_t(r)$ of a shower increases very significantly with the distance r to the axis of the shower (the core) and is quite inde-

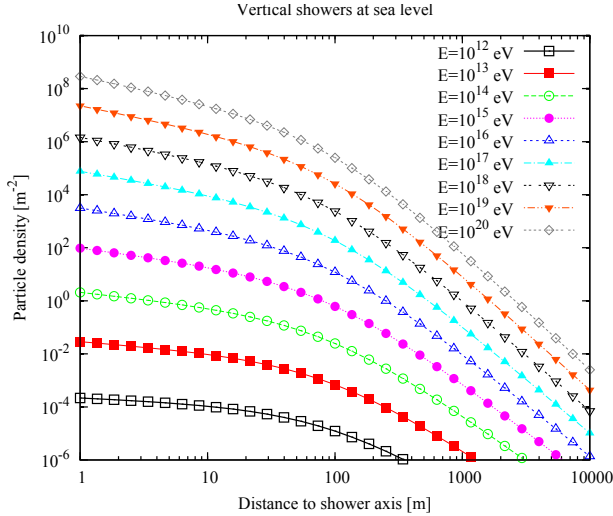


Figure 6.4: Lateral distributions of the particle density at the sea level according to the NKG parametrisation for energies ranging from 10^{12} up to 10^{20} . The picture has been taken from [116].

pendent of the energy of the primary cosmic particle. This behaviour was parameterised by J. Linsley [117] in the form:

$$\sigma_t(r) = \sigma_{t_0} \left(1 + \frac{r}{r_t}\right)^\beta, \quad (6.1)$$

where the parameters take the value: $\sigma_{t_0} = 2.6$ ns, $r_t = 30$ m and $\beta = 1.5$.

- The density of particles of a shower, at a given distance to the core, depends on the size N_0 (number of particles) of the shower and the distance in the form:

$$\rho(r, N_0) = \epsilon \cdot N_0 \cdot r^{-n}, \quad (6.2)$$

where both, ϵ and n , depend on the mass of the primary cosmic ray. For a proton, $\epsilon = 0.00053$ and $n = 1.5$. The lateral density distribution for energies ranging from 10^{12} to 10^{20} calculated using the Nashimura-Kamata-Greisen parametrisation [109] is shown in the Fig. 6.4.

- The energy of the primary cosmic ray is related to the size of the shower by:

$$E_0(N_0) = \alpha \cdot N_0^b \quad (6.3)$$

where, according to [118], for protons $\alpha = 2.217 \cdot 10^{11}$ and $b = 0.798$.

Using all these parameterisations it is possible to get the energy of the primary cosmic ray as a function of both the time width and the density of particles measured by a single detector. The final relationship is:

$$E_0 = \alpha \left[\frac{\rho}{\epsilon} \left(r_t \left[\left(\frac{\sigma_t}{b} \right)^{1/\beta} - 1 \right] \right)^n \right]^b. \quad (6.4)$$

6.2 Signatures from cosmic rays air showers from simulation

The signatures studied here from Monte-Carlo simulations have been targeted specifically at the capacity of a high granularity time of flight detector. To analyse the ability of these detectors to access parameters such as:

- track arrival direction of particles with an accuracy of 1° ,
- time resolution around 100 ps,
- capability of discern the energy lost in the detector,

can contribute to extend the known models and improve the data quality.

The showers were simulated using the AIRES code [119] by Dr. R. Vázquez. The secondary particles which reach the sea level are stored with their position respect to the center of the shower axis (x_i, y_i) , the incidence azimuthal and zenith angles (θ_i, φ_i) , the arrival time t , the energy E , the altitude at it was produced h and the type of particle $(\gamma, \mu^{+/-}, e^{+/-})$.

Fig. 6.5 shows some representative parameters for positive and negative muons and electrons. The top two figures represent the zenith arrival angle at the sea level as function of the distance to the shower axis of 100 vertical showers triggered by a proton of 10^{15} eV. Barely, most of muons arrive close to the shower axis in an interval of 5° whereas electrons arrive at larger angles. This behaviour is the expected as muons are produced

close to the core of the shower where the energy density is higher and can go through the atmosphere practically unscattered. On the other hand, the electromagnetic component of the shower undergo interactions $e - \gamma$ every ~ 100 m, due to the number of interactions before arriving to the ground, they lose the information from the primary interaction. Furthermore, the energy spectra for both muons and electrons reveals that 70% of electrons which reach ground, have an energy of less than 100 MeV. Below that energy, ionisation starts to dominate (Sec. 2.1), which is crucial to understand the charge spectra from the RPC shown in the Section 4.3. Finally, the last signature is the azimuthal arriving angle. As it was already mentioned, muons, keep the information of the primary which is also observed in the azimuthal angle distribution, where are compared the incidence φ_i angle and the angle φ_s referred to the shower axis. Here, the attentions must be focused on the electron distribution, that in mean points to the axis of the shower.

6.3 Performance of the HADES RPC-TOF wall as a CR detector

The HADES RPC wall was designed to optimize the performance of the HADES spectrometer in high multiplicity environments. Thus, the geometry and cell distribution in the detector was not thought to perform optimally and with high acceptance the measurement of cosmic rays showers.

During the cosmic test, pairs of two sectors were stacked horizontally at a distance of ~ 350 mm as it is shown in Fig.6.6. Detectors were operated indoors under a couple of light roofs offering less than one radiation length width to the incoming showers. The average time resolution for individual cells during the test was 77 ps σ [101].

6.3.1 Special calibration and synchronisation and arrival plane reconstruction methods

The main difference between beam data and the data acquired during the cosmic commissioning is the absence of an external trigger providing a start time to the RPCs and tracking detectors. The cosmic events were

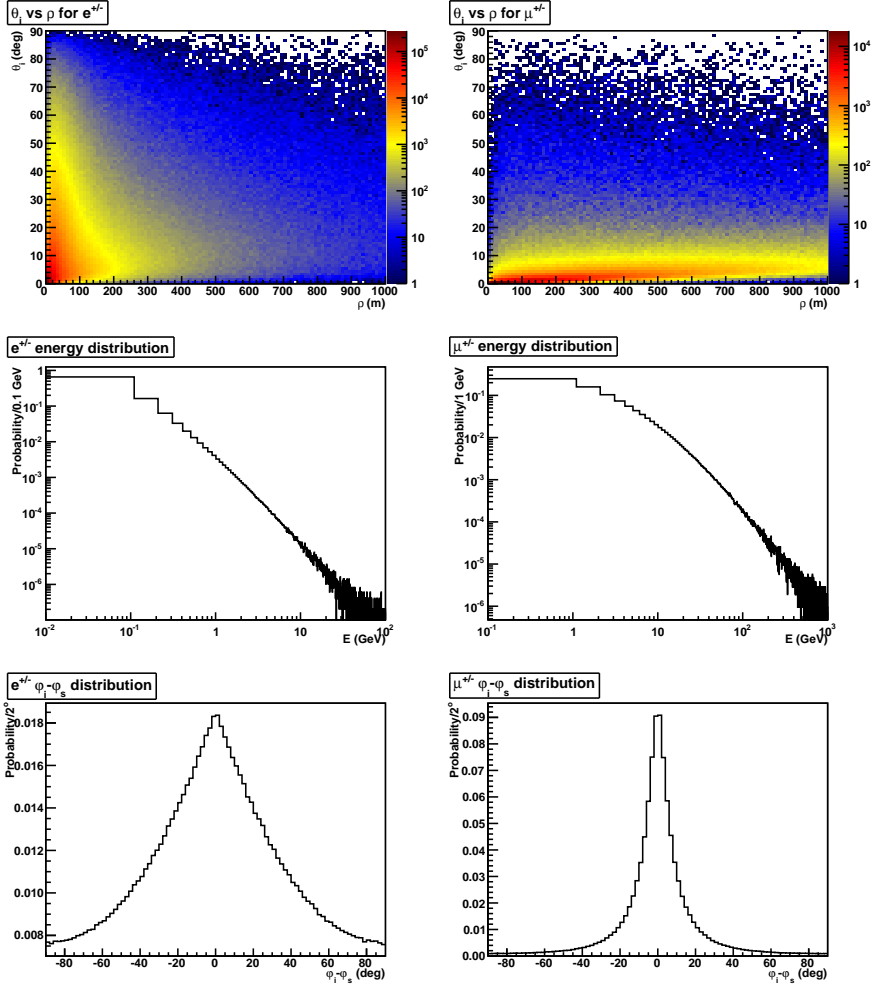


Figure 6.5: Characteristic signatures of secondary particles in a simulated cosmic ray shower caused by a proton of 10^{15} eV with normal incidence over the atmosphere.

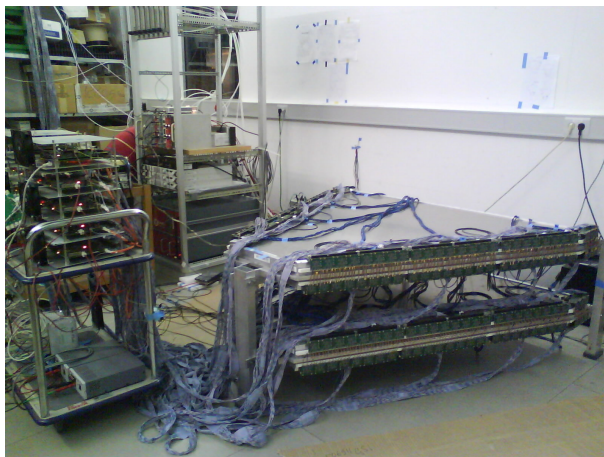


Figure 6.6: Two HADES RPC sectors taking cosmic ray data during the commissioning of the detectors.

acquired requiring a coincidence between the upper and lower planes, and the first registered time in the event (it does not mean the first arrived particle), plays the role of the reference time. Thus, the correct start time for each event should be found.

Charge and position calibration tasks were carried out using events with less than four fired cells in each sector in order to avoid contamination by multiple hits. Position and charge observables were calibrated by setting constant offsets in the measured values following the same routines as in the Section 4.1.

Events with one traceable particle crossing both sectors of the stack were required for synchronisation purposes. To enhance the probability of choosing a good particle candidate, the position difference between both hits belonging to overlapped layers was required to remain within 3σ .

The trigger was defined by the coincidence of the upper and the lower sectors. Each recorded event has its own time reference and only relative times between hits are available. Therefore, the full detector synchronisation was achieved using a recursive algorithm that minimises the time differences between the two sectors. Under the hypothesis that all particles

travel at the speed of light, c , time difference between hits should fulfil:

$$\Delta T = (t_{rpc-i} - \tau_i)|_{down} - (t_{rpc-j} - \tau_j)|_{up} - d_{ij}/c = 0, \quad (6.5)$$

where d_{ij} is the distance between hits of cell i and j and $\tau_{i,j}$ is the time offset of the respective cell. ΔT has been minimised iteratively and convergence was reached after 5 iterations over all cells. By characterising the ΔT distribution a criteria for selecting track candidates can be derived. The standard deviation σ_T was found to be ~ 176 ps. The distribution and the fit are shown in Fig.6.7. In the shower front analysis, ΔT between hits was required to be always within 3σ to define a track candidate. Each track is characterised by the arrival time, t_{rpc} and (x_{rpc}, y_{rpc}) coordinates in the upper plane and an unit vector $\mathbf{n}_i = (\alpha_i, \beta_i, \gamma_i)$ in the propagation direction. Fig.6.8 shows an example of a reconstructed high multiplicity event where the reconstructed track candidates are represented by arrows.

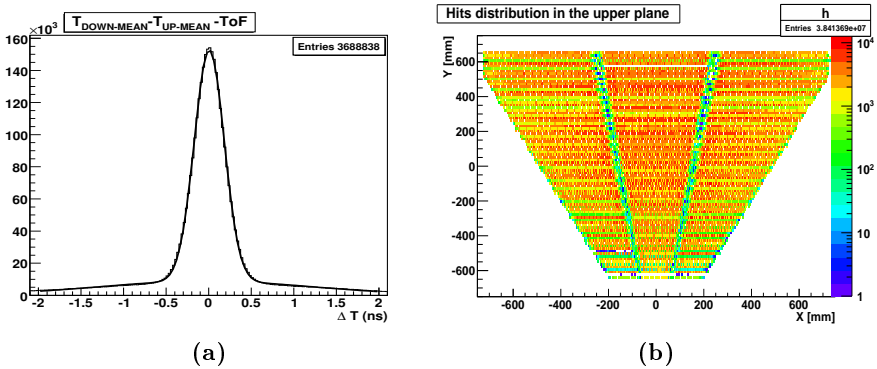


Figure 6.7: a) ΔT distribution between the upper and the lower sectors. Two gaussians have been fitted to interpret both signal and background. The rms of the signal is 176 ps. b) Hit distribution at the upper sector after the position calibration. The three-column structure of the detector and the different cells sizes are apparent.

6.3.1.1 Incidence angle reconstruction

The behaviour of particles shown in the 6.5 reveals that both electrons and muons keep information about the direction of the primary. Taking

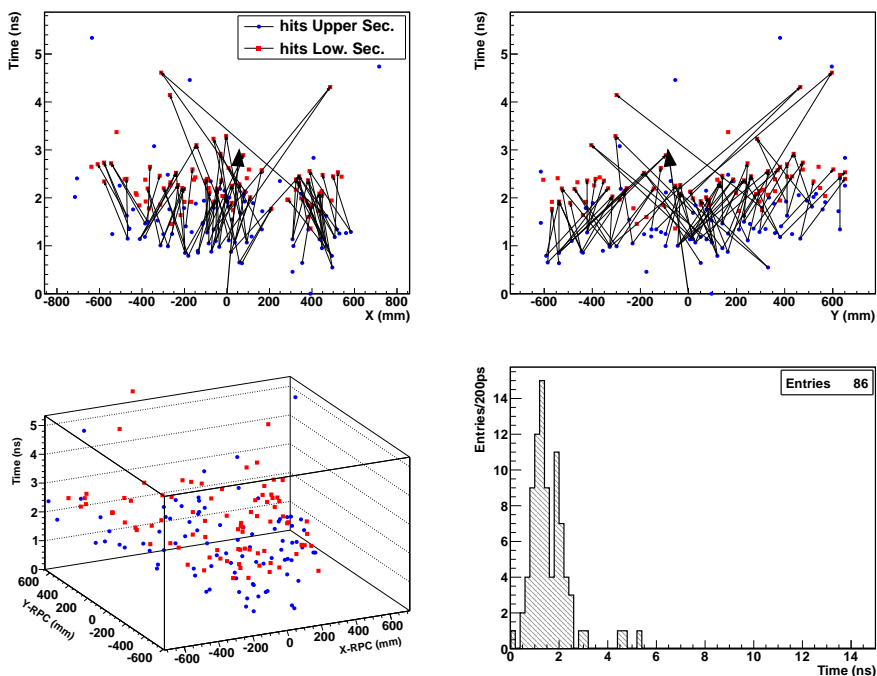


Figure 6.8: Example of the arrival profile of a high multiplicity shower after calibration and synchronisation. Blue and red markers refer to the top and bottom sectors respectively. A delay of around ~ 1 ns due to 350 mm separation between them is observable. Arrows represent the track and shower directions. Top left: t_{rpc} vs x_{rpc} -coordinate. Top right: t_{rpc} vs y_{rpc} -coordinate. Bottom left: 3D view of the measured particles. Bottom right: Profile of arrival time after performing the incidence angle correction.

this into account, after reconstructing tracks, we can define the shower's incidence angle $\mathbf{n}_s = (\alpha_s, \beta_s, \gamma_s)$ as:

$$\mathbf{n}_s = \frac{\sum_{i=1}^{N_{tracks}} \mathbf{n}_i \cdot w_i}{\left| \sum_{i=1}^{N_{tracks}} \mathbf{n}_i \cdot w_i \right|}, \quad (6.6)$$

where N_{tracks} is the number of track candidates and $w_i = \sigma_T / (\sigma_T + \Delta T_i)$ is a weight factor, being ΔT defined in the equation 6.5. The introduction of a weight factor is mandatory because, in high multiplicity events, the asymmetric acceptance of the detector may introduce systematic deviations in the incidence angle reconstruction. Once an estimate of the arrival direction of the shower has been calculated, the corrected arrival time is defined as:

$$t_{corr} = t_{rpc} - (\alpha_s \cdot x_{rpc} + \beta_s \cdot y_{rpc}) \cdot c^{-1}. \quad (6.7)$$

Fig. 6.8 shows an example of the reconstructed incidence direction and time profile after the aforementioned correction.

Another alternative for the plane reconstruction is to follow the standard plane fitting method. The functional which minimises the best fitting flat surface to the arrival distribution of particles as a function of time is:

$$t_i \cdot c = k + x_i \cdot p1 + y_i \cdot p2, \quad (6.8)$$

where k is an offset constant and $p1$ and $p2$ are the x and y slopes of the plane respectively and i is the sub-index of the i -particle in the measured shower.

6.4 Measured signatures for an advanced study of CR events

In this section results informing about the low scale structure of showers measured are presented[120]. Also, a comparison between the two plane reconstruction methods, the flux of the particles for different multiplicities and a row primary energy spectra are obtained. No correction related to geometry, efficiency, dead time, occupancy or acceptance has been performed, although any of these factors could affect significantly our qualitative results.

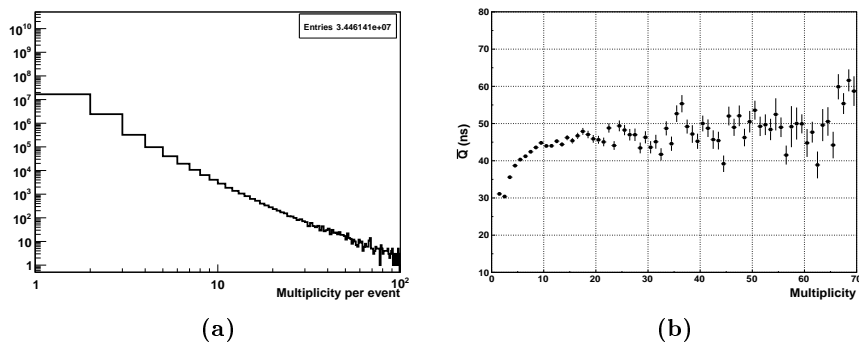


Figure 6.9: a) Measured multiplicity in the upper sector of all the triggered events over a continuous five day period. b) Mean measured charge as a function of multiplicity for all the events with at least one track candidate.

6.4.1 Front parameters

6.4.1.1 Particle multiplicity, mean charge and arrival time distribution

The distribution of the hit multiplicity of all the events in the sample is shown in Fig.6.9a. Fig.6.9b shows the mean charge of the hits in the upper sector as a function of the multiplicity of the showers. The observed increase of the mean charge with the multiplicity may be explained as being a consequence of the different mean composition of the shower for different multiplicities and the dependence of the mean charge on the mass of the particle and its energy (see Section 4.3), since in general cosmic electrons are more ionizing particles than cosmic muons. Therefore, it shows how low multiplicity events are mainly dominated by minimum ionising muons whereas the electron and high energy muon contents increase together with the multiplicity.

Fig.6.10a shows the number of events as a function of both the hit multiplicity and the time width of the front, defined as the standard deviation of corrected arrival time of the particles in the shower. Roughly, higher multiplicities correspond to higher energy primaries and larger time widths

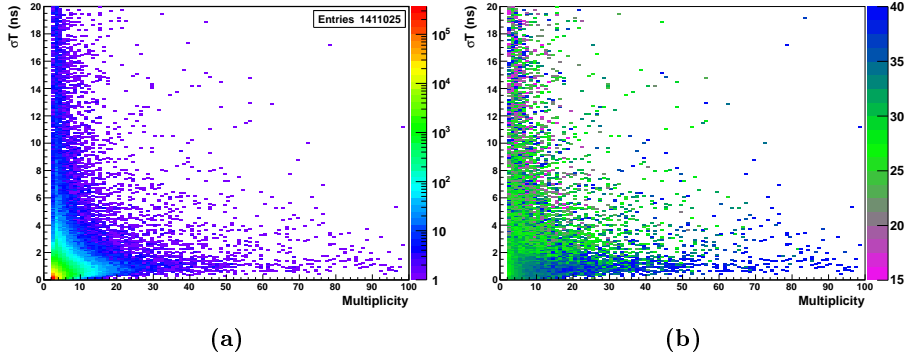


Figure 6.10: a) Scatter plot of multiplicity vs the standard deviation of arrival times within a shower. b) Same plot representing in the z-axis the mean measured charge.

correspond to higher distances between the detector and the core of the shower [121]. Then, low energy showers tend to occupy the bottom-left corner of the figure whereas very much less frequent high energy shower tend to occupy the upper-right corner. Fig.6.10b has the same x and y axes and shows in the z-axis the mean charge per event. Here the well known effect that for high multiplicity/energy showers, the electromagnetic component dominates near the core together with some high energy muons (bottom-right side), whereas the lower energy muon component dominates far away from the core (upper-left side), can be seen. Also, low energy showers seem to be mainly populated by low energy, minimum ionising muons.

Fig.6.11 shows the corrected time delay of the hits in the upper sector respect to the first arriving particle for several multiplicities of the event. Lower multiplicity distributions show several changes of slopes that would need further analysis. However, a few general conclusions can be extracted. Low multiplicity distributions are mainly dominated by low-energy showers, having particles arriving within very short time differences of $\sim 1-2$ ns. As the multiplicity increases the slope of the distributions decreases, showing the effect that high multiplicity events are increasingly dominated by showers of higher energies arriving far away from the detector. Large time

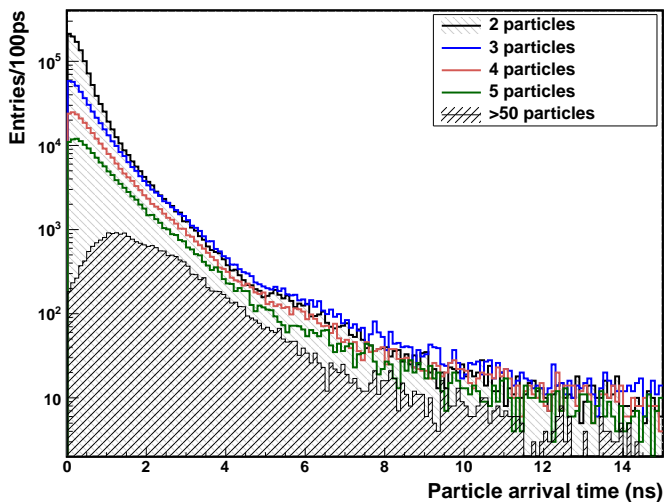


Figure 6.11: Arrival time of all the hits within a shower referred to the first measured time for several multiplicity selections. Neither geometry, efficiency, dead time nor acceptance corrections have been included.

differences correspond to particles of high energy showers having arrived very far away from the detector. The high multiplicity subsample shows the gamma-like distribution already observed in high energy showers [122].

Any of the multiplicities has the contribution of showers of many energies where, showers of each energy contribute with a particular distribution of time differences. It means that, if the time distribution is measured with enough accuracy and statistics, a single multiplicity distribution would allow to explore changes in the rate of the showers in a certain range of energies.

The arrival time pattern of the particles belonging to showers of a given energy, at a given distance and hence, with a given multiplicity, provide information about several aspects of the shower. Those times follow usually a gamma distribution, where the width informs about the distance to the core of the shower and the mean value allows a better estimation of the

arrival time of the shower to that detector. As a consequence, detectors with very good time resolution and an enough granularity wool allow a better estimation of the arrival direction of the primary cosmic ray.

6.4.1.2 Front incidence angle comparison with traditional plane fitting

In the Section 6.3.1.1 we have shown two methods to calculate the incidence angle of the avalanche and to perform the corresponding arrival time correction. The first method consisted in using the sum of the weighted vectors of the particles to calculate the incidence direction. This method has one important advantage over the traditional plane fitting that even in the cases when few particles are detected we may estimate its arrival direction. This is a very interesting feature because it allows to give an estimate about the local direction of the front of the shower. Also, together with other measured variables (like the azimuthal angles), as has been already pointed out as after the simulations commented in Section 6.2, it may allow to estimate the direction of the incoming primary. On the other hand, that estimate is independent of the arrival time as only the trajectories are used. In this sense the traditional plane fitting may fail if the arrival time spread is too high; more than a few ns for a $\sim 1\text{m}^2$ detector.

Plane fitting requires at least three particles to provide an analytical result and four particles are needed if we want to have at least one degree of freedom. The analysis done here required at least five particles in a 4 ns range around the median arrival time. This condition was set to minimise the impact of the delayed particles present in the tails.

The difference between the azimuthal angle calculated using both methods is shown in the Fig. 6.12. The φ_{pl} corresponds to the value obtained through plane fitting and φ_{tr} to the value obtained using the equation 6.6. The bands present in the top left and bottom right corners are caused by a π shift in the obtained angle value. It was found a very good agreement between both methods and the results show differences, in general smaller than 25° .

Regarding the zenith arrival angle, both methods behaves in the same way as in the azimuthal reconstruction case. The difference distribution of values obtained by between both methods shows a difference of about 10° .

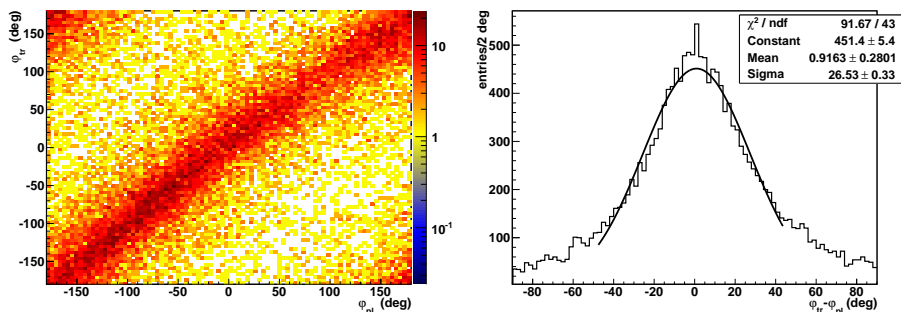


Figure 6.12: Azimuth difference analysis $\Delta\varphi$ between the plane fitting algorithm and the track direction method. Left: φ_{tr} vs φ_{pl} ; the structures on the top left and bottom right are caused by a shift in the phase. Right: Approximate fit to the distribution of $\Delta\varphi = \varphi_{tr} - \varphi_{pl}$.

The asymmetric structure enhanced at high angles (above 50 deg using the plane reconstruction method) may be caused by the shape and acceptance of the detector.

Agreements between both methods are quite good even taking into account that the analysis didn't went in depth on the matter. With such a small detector, uncertainties associated to the geometrical fit of a plane are too big to allow getting very much better results; bigger detectors would be needed to improve the analysis. Also data with a better resolution on the velocity of the particles, for instance with a larger distance between detectors, would be needed for a better rejection of combinatory background. In any case, as the track direction method requires a smaller number of particles per event for providing a direction estimate, even with a small surface detector, it may be very useful for complementing the information given by big arrays of detectors.

6.4.2 Flux of particles

The measurement of the rate of cosmic rays arriving to the Earth surface is very interesting because they may provide valuable information about many variables related, not only with their intrinsic properties but also with many variables related with the Earth's surroundings: Sun activity,

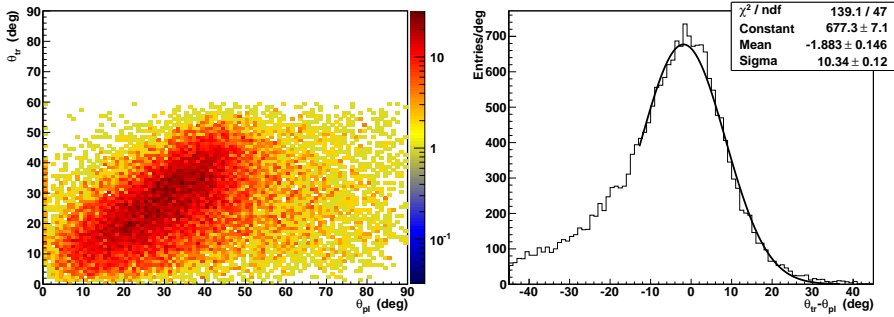


Figure 6.13: Zenith difference analysis $\Delta\theta$ between the plane fitting algorithm and the track direction method. Left: θ_{tr} vs θ_{pl} . Right: The distribution of $\theta_{tr} - \theta_{pl}$ shows a good agreement between both methods $\sim 10^\circ$. The asymmetrical distribution noticeable at zenith angles above 50° deg may be caused by the acceptance and shape of the detector.

interplanetary and Earth's magnetic field, etc. By these reason our planet is covered by a network of cosmic rays stations based mainly in neutron detectors, that can only measure integral flux, and muon detectors, that may provide also directional information. The permanent scanning of cosmic rays is also very useful to detect sudden asymmetries that may be precursory signatures of possible solar disturbances. Typical equipments used in that network are based in conventional techniques, as scintillator detectors or proportional counter tubes, and many of them have even limited directional capabilities. An RPC setup, like the one we are analysing, may offer a lot of advantages respect those methods.

Fig. 6.14 shows the evolution of the flux of one-particle and 2 and 3-particle events we measured along 120 hours, where neither efficiency, pressure, temperature or acceptance corrections have been done. The uncorrected mean rate of such subsample was about $\sim 90 \text{ Hz.m}^{-2}$ and, in both cases, the fluctuation between the maximum and the minimum is about $\sim 5\%$. Nevertheless that flux informs us about the resolution we could reach with an 1 m^2 detector if we measure variations in the rate. Thus, if we want to measure variations with 1% accuracy, the flux mea-

sured should fulfil:

$$\frac{\sqrt{\Delta\Phi}}{\Delta\Phi} > 0.01 \longrightarrow \Phi > 10000, \quad (6.9)$$

and taking into account that in 15 minutes slices we have maximum variations of 4000 particles, the hour variation would provide enough accuracy. However, as our detector may have a non-negligible capability of separating muons from high energy electrons and, even, making directional cuts (for instance: vertical, North, South, East or West) it could provide directional $\sim 1\%$ accurate changes in rate every few hours. Unfortunately our detector was significantly affected by the broad walls of concrete of the experimental area of HADES and such analysis is not possible with our sample of data.

The figure shows also the result of a frequency analysis performed on the flux variation. The main harmonics have a period of ~ 24 hours and components of higher indexes are less significant and may be mainly produced either by pressure or temperature effects. This daily effect is very well known and it is due to the different modulation the Sun produces to the high energy galactic cosmic rays depending on the relative position of the Earth during the day and the night. The maxima are located at around 13.3 hours in the one-particle distribution and at around 17.3 hours and in the two- or three-particles distribution. The first result is compatible with the well known effect that, due to the rotation of the Sun, there is a shift of the magnetic field direction followed by the solar wind respect to the solar time of about 6 hours [123]. The other measurement seems to show that that time shift tends to decrease with the increasing energy of the primary cosmic rays, as has been seen by other experiments [124]. In any case, a more precise conclusion would require to perform the necessary atmospheric pressure correction.

The flux of events having two or three particles is scarce compared to the flux of events with only one particle. However, they may give very important complementary information about the behaviour of the flux rates. Events, with either two, three, four, etc. particle events have progressively larger contributions of higher energy primaries and, as a consequence, would allow to separate their contributions to the measured rates.

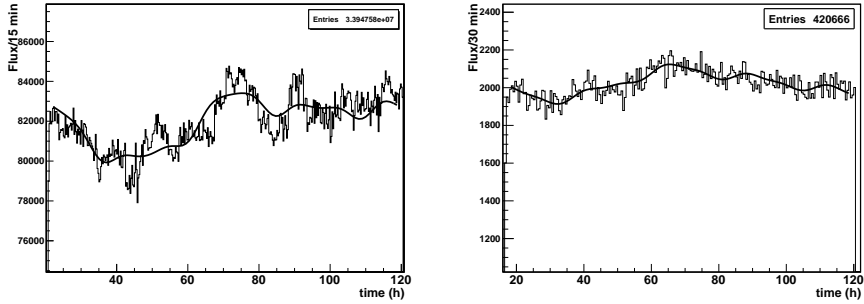


Figure 6.14: Flux of events with only one particle (left) and two and tree particles (right) along the five day period. The black line represent the frequency analysis performed on these data. For events with only one particle it was found a periodicity of 24.3 h, together with contribution of higher and lower orders harmonics. In the two and tre particles per event case it was found also a periodicity of 24.0 h.

6.4.3 Row measured primary energy flux

The energy of the primary cosmic ray can be deduced by using the particle density and the spread of arrival times using the parametrisations shown in Section 6.1.2. Even though this data has no corrections, the reconstruction of the energy of the primary provides a qualitative result.

In first place, the Fig. 6.15 shows the energy-density lines obtained from equations 6.1-6.3 super-imposed on the measured σ_t - density distribution. All the calculations implicitly suppose that all the primaries are protons and the incidence direction is almost vertical to the ground. The number of entries between the lines already give us the first qualitative result and how low and high energy primary cosmic rays behave.

Finally, if we also compute the time period and the surface that events with certain energy can reach from the NKG parametrisation shown in the Fig. 6.4 we can obtain the ROW spectra of energies, shown in the Fig. 6.16. Of course corrections must be performed, nevertheless the flux of the energy spectra matches with a decade accuracy with the known measurements. The behaviour at energies below $10^{14.5}$ eV should be interpreted very carefully as three contributions plays an important role:

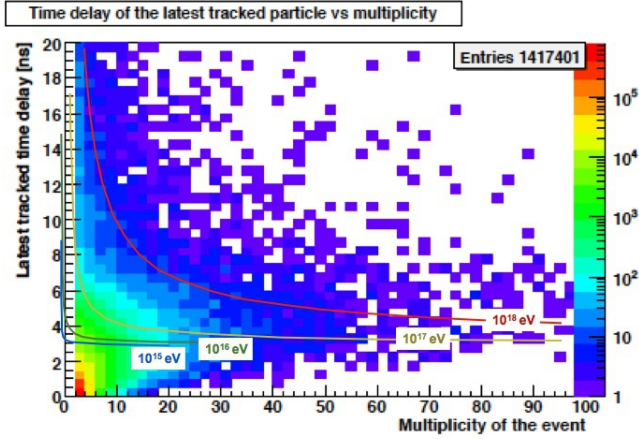


Figure 6.15: Isoenergetic primary cosmic ray regions super-imposed to the measured σ_t - density distribution

- The used parametrisations behave well at energies above $\sim 10^{16}$ eV.
- The probability of measuring two particles in a square meter for showers of energies below $E = 10^{14}$ eV is scarce.
- No correction to densities were performed, thus in the case of having only two particles, the corresponding errors can enhance an artificial decrease.

Regarding the enhancement observed in the 10^{17} eV region it is probably related with the measurement of the density of the particles together with the weight in the σ_t factor of the long tails, which cannot be measured accurately with a detector of ~ 1 m².

6.5 Conclusions

The previous results show that a detector composed by several planes of high granularity timing RPCs may provide access, at the same time, to a wide range of cosmic rays observables at an affordable price: particle density, arrival time distribution, charge distribution or local arrival direction.

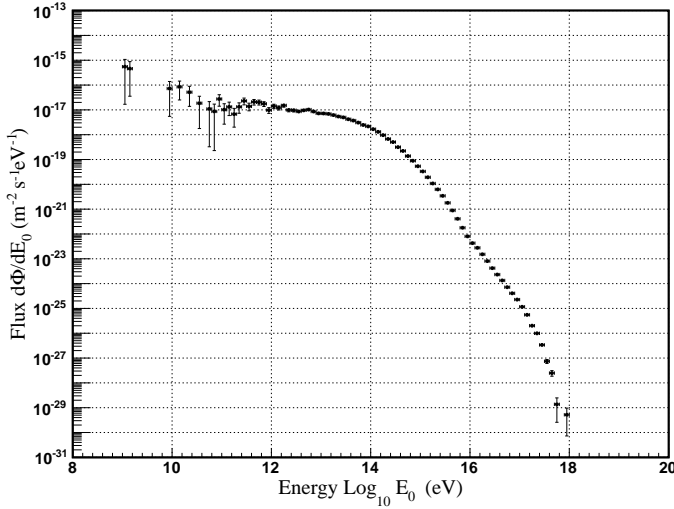


Figure 6.16: ROW flux of primary particles as a function of the energy of the primary particle.

All this variables may give faithful information about the properties of the parent primary cosmic ray.

Primary cosmic rays above an energy of about $E \sim 10^{15}$ eV are so scarce that their main properties (mass, energy and arrival direction) are usually estimated indirectly measuring a small sample of the billions of secondary particles produced when they interact with the atoms of the atmosphere. For this purpose secondary particles are gathered using big arrays of detectors placed at the Earth surface, with enough density to measure a representative sample of the whole swarm of particles. However, other alternatives have been proposed.

J.Linsley suggested in the eighties [117] to use the empirical relationships observed in the showers relating the time width with the distance to the core on one side and the particle density at this distance with both the size of the shower and the energy on the other. Using this features, a mini array of detectors able to measure the density and the arrival time distribution of particles could be used to measure the rarest and more energetic cosmic rays. A network of such small arrays, working independently of each other,

could be an alternative to the big arrays of detectors at a less cost per unit area.

The Linsley's approach has been used by different experiments as Akeno [125] [126], the GU mini-array [127] [128] and LAAS [129] [130] to analyze cosmic rays. All of them provided results that are in agreement with those provided by observatories using traditional techniques. More recent studies [121] show that electrons and muons behave very differently far away from the core, both in their arrival time and in their time distribution. A separate parametrization of these effects should allow to improve substantially the method.

Other initiative, the NEVOD-DECOR complex, has started to study extended air showers using a single big-volume (2000 m^3) detector based on the measurement of other observables as the local muon density and the energy of the muon bundles. This experiment show how a single experimental setup gives the possibility to study features of the spectrum and the composition of primary cosmic rays and characteristics of hadron interaction in a wide energy range [131].

In this regard, timing RPC-based detectors providing:

- a) a good granularity for the measurement of the particle density,
- b) a very good time resolution for the accurate measurement of the time profile and, together with a), providing an estimate of the energy of the shower,
- c) the tracking of all the charged particles and an estimate of the local direction of the shower, allowing the time distribution correction,
- d) an estimate of the electron/muon ratio and estimates of their respective arrival time distributions and densities,

together with all the correlations among them, could offer a new way to analyse cosmic ray showers as an alternative to other methods. Such kind of detectors could be also of interest for complementing traditional big-array observatories or big-volume facilities.

Results presented here are very encouraging. However more work should be necessary to analyse the possibility of improving the capability of RPCs to separate cosmic electrons and muons via either an appropriate tuning of the operational parameters or improving the charge sampling using more layers. Moreover, together with the results of the charge analysis, seen in the Section 4.3, arise the possibility of measuring the energy of muons. Also, more detailed and accurate studies about the relationship between

the micro-structure of the front region of a shower and the primary cosmic ray parameters provided by an external big observatory should be performed.

7 Conclusions and Main results

The present work examine several aspects related to the Resistive Plate Chamber TOF wall of the HADES experiment at the GSI. The project of using an innovative technology such as timing RPCs in HADES started as an alternative to the conventional use of scintillators and Photo Multipliers. The final detector develop was proposed by Prof. P. Fonte from LIP, Coimbra and Prof. J.A. Garzón from LabCAF, University of Santiago de Compostela and was build in collaboration with other groups of Germany, Poland and Spain. The collaborative effort made to accomplish all the tasks brought to life and light the detector finalising the prototyping, design, building and testing phases with the Gold on Gold beam data taken by HADES in 2011 and 2012.

The strict requirements set on the detector:

- efficiency above 95% for single hits,
- time resolution below 100 ps for MIPS,
- rate capability up to 1 kHz,
- hit loss probability below 20% for central collisions

where successfully fulfilled, and some of them have even surpassed. In this work we have contributed in reaching the following performances: the efficiency, for single hits is above 97%, the obtained time resolution, in the most unfavourable case is 72 ps sigma and the mean time resolution is below 65 ps sigma. Regarding rate the capability, the Au+Au central-most collisions at 1.24 AGeV does not show any worsening of the performance and the occupancy is kept always below 20%.

To achieve this time resolution the algorithms used for calibration and synchronisations of the RPC cells were revised and improved. It is noteworthy to mention the implementation of the position-time correction using information provided by the tracking system, adding a second spatial dimension and allowing to correct local gain deviations in the cells.

Moreover, a deep analysis of the charge was performed. A new technique to estimate the efficiency of the detector through the charge spectra was implemented showing a very good agreement with standard techniques. The strong point of this approach is that it is free of contamination by fake tracks, unfortunately always present from tracking. Then, the relation between the measured charge and resolution was analysed. The inverse behaviour of both was observed as expected. Furthermore, an unexpected mass scaling effect in the resolution and charge in disagreement with the Bethe-Bloch formula was observed, opening the door to new very interesting developments; further investigations will be required.

The TimTrack particle reconstruction algorithm has been extended to be used with non linear tracking models and to include analytical constraints between the fitted parameters. The fitting model has been developed for any layout of drift chambers having non parallel planes and non parallel drift wires. The algorithm has been applied to the tracking of particles using the drift chambers of Hades. The obtained position and momentum resolutions were close to the existing one, showing differences between both below around 6%. Despite we do not have extract all the possibilities of the method. Further improvements of the performance of the method should be obtained with the recursive TimTrack algorithm being now developed in our group.

We have analysed the cosmic rays data taken during the commissioning of the RPC wall sectors. As no other external detectors were available a dedicated method was developed for the calibration of the detector and the needed synchronization of the detectors. Then we started to analyse the microscopic properties of the cosmic rays air showers with a joint granularity and time resolution never used before in a detector placed on the Earth surface. We show how such a relative small detector could be used to measure the rate of cosmic ray air showers using the existing parametrisations for high energy primary cosmic rays. Further studies should be necessary to extend those parametrisations to lower energies. Such a detector provides also an estimation of the arrival direction of the showers allowing to perform selective analysis of their arriving direction and rejection of background events. As a consequence, this kind of detectors could be an alternative to other technologies for the continuous survey of cosmic rays as neutron monitors and standard muon detectors for the continuous survey of cosmic rays arriving to the Earth at a broad range of energies.

8 Resumen

La tesis titulada “New advances and developments on the RPC TOF wall of the HADES experiment at GSI” está dedicada al análisis de los datos tomados con el detector de tiempo de vuelo basado en tecnología de placas resistivas paralelas (RPC) instalado en el experimento HADES, en GSI, Alemania. Este detector fue diseñado y construido por una colaboración internacional con grupos procedentes de España, Portugal y Alemania entre los que figura el grupo LabCAF de la Universidad de Santiago de Compostela con una aportación importante en el diseño, puesta a punto y el necesario software de reconstrucción. En esta tesis se analizan los datos tomados por el detector durante el periodo 2009-2012.

El primer capítulo introduce el experimento HADES, sus objetivos y los diferentes detectores que conforman el espectrómetro. En el capítulo 2, se hace una introducción a la interacción radiación-materia, haciendo especial énfasis en la radiación ionizante y en detectores gaseosos. Finalmente en este capítulo se hace una introducción desde una perspectiva histórica a las cámaras de placas resistivas paralelas. En el tercer capítulo se introducen las características técnicas del muro de tiempo de vuelo de RPC instalado en HADES.

Entre los años 2011-2012, el experimento HADES realizó dos tomas de datos de colisiones de oro-oro a una energía de 1.25 GeV por nucleón. En el capítulo 4, se hace un resumen de las técnicas de calibración empleadas y se hace un análisis de los datos desde el punto de vista de la propia física subyacente del detector.

En el capítulo 5 se introduce un nuevo algoritmo para el cálculo de trayectorias de partículas cargadas, desarrollado por nuestro grupo llamado TimTrack. Éste es un método pensado para uso con detectores que ofrecen una buena medida de tiempo de vuelo y posición simultáneamente. El algoritmo es aplicado al espectrómetro y comparado con el método de cálculo de trayectorias Runge-Kutta.

Los datos del año 2009 se corresponden con la puesta a punto del detector realizada con radiación cósmica. Al análisis de estos datos arroja luz

sobre la utilización de los detectores basados en la tecnología RPC para la medida de la radiación cósmica ionizante.

8.1 Capítulo 1

El primer capítulo de esta Tesis esta dedicado a la introducción del experimento HADES [2], localizado en GSI, Alemania. Especial énfasis se hace tanto en la estructura del espectrómetro de dileptones, mostrado en la figura 8.1 como de las herramientas de análisis existentes para la completa reconstrucción de las colisiones producidas como el momento, las trayectorias o la identificación de partículas.

El fin científico del espectrómetro es la medida de precisión de la materia nuclear densa presente en las colisiones de núcleos pesados como el oro o la plata. Este estudio se hace a través de la medida de los productos de desintegración de los mesones vectoriales ligeros ρ , ω y ϕ . Especial relevancia en este sentido lo tienen los pares electrón-positrón producidos en las desintegraciones de los mesones ya que tienen la propiedad de poder atravesar la materia nuclear densa prácticamente sin sufrir alteraciones, por lo que son unos testigos de excepción de lo que ocurre en las colisiones.

8.2 Capítulo 2

El segundo capítulo sirve la base teórica necesaria para el análisis de los detectores de ionización gaseosa. Empieza introduciendo la interacción radiación materia, centrandó siempre el interés en la interacción de las partículas ionizantes con los gases. Cabe destacar la importancia de la pérdida de energía en los materiales expresada en la fórmula de Bethe-Bloch [42] y la importancia de tener en cuenta el espesor del detector apuntado por H. Bischel [45].

El último apartado del capítulo hace una introducción histórica a los detectores de placas resistivas paralelas. Ésta es una tecnología moderna, que ha tenido un gran desarrollo en los últimos años del siglo XX y principios del XXI debido a las prestaciones que son capaces de alcanzar a un precio moderado si es comparado con los detectores de estado sólido como los centelladores. Estos detectores se engloban en la familia de detectores de placas paralelas, siendo las cámaras de chispas sus directos antecesores.

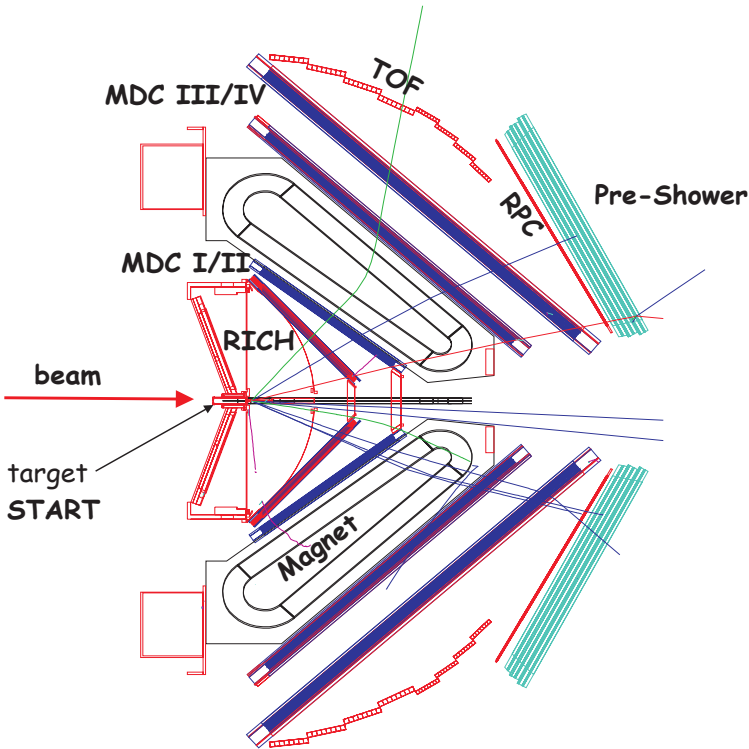


Figura 8.1: Esquema del espectrómetro HADES con todos los detectores que conforman el sistema. El detector empezando por la izquierda se compone de: un blanco de interacción localizado a la salida del haz, un detector de efecto cherenkov llamado RICH, cuatro planos de cámaras de deriva multihilos que junto con un sistema de seis imanes superconductores ILSE son los encargados de realizar la medida del momento de las partículas y su trayectoria, después nos encontramos con los detectores de tiempo de vuelo TOF y RPC, basados en tecnología de centelladores y cámaras resistentes paralelas (RPC), detrás del muro de tiempo de vuelo de RPCs esta colocado el Pre-Shower un detector para la separación hadrones-electrones a través de cascadas producidas en plomo. Finalmente, y no aparece en el esquema a varios metros de distancia está instalado un detector para medir las partículas que atraviesan a bajo ángulo el espectrómetro por el centro sin interactuar.

Los detectores de chispas han mostrado la capacidad de ofrecer resoluciones temporales por debajo de 25 ps sigma en las décadas 50 y 60 del siglo pasado. Sin embargo estaban limitados por una compleja construcción que incluía presiones de gas por encima de las 12 atm, anchuras del espacio que contiene el gas del orden de 100-200 μm y una adquisición basada en principios opto-electrónicos. Estaban limitados por el tamaño que podían alcanzar y la gran complejidad constructiva que presentaban. A principios de la década de los setenta, se introdujo un cambio sustancial en esos detectores que consistió en introducir una placa resistiva entre el gas y uno de los electrodos para limitar la propagación de las avalanchas. Este detector se llamó Contador de Pestov y puede considerarse como la primera RPC [55]. Sin embargo seguía manteniendo la complejidad constructiva de las cámaras de chispas de tiempo de vuelo, por lo que la primera RPC se considera la construida por R. Santonico y R. Cardarelli en la década de los ochenta [57] que simplificaba la construcción para que pudiese ser operado a presión atmosférica. El precio inicial a pagar fue la pérdida de resolución temporal, que era compensada de sobra por el precio del nuevo detector con el cual cubrir grandes superficies no era un problema por lo que rápidamente encontró un nicho de uso en grandes experimentos del CERN y de rayos cósmicos.

A principios de este siglo se introdujo una subclase de RPCs, llamadas de tiempo de vuelo, que recuperaban las prestaciones temporales mostradas por los detectores de chispas y el especial contador de Pestov. El diseño incluyó un avance de suma relevancia: la reducción del tamaño de la región de ionización-amplificación de gas por debajo del milímetro. Ésto, conjuntamente con el empleo de múltiples capas (una tecnología que ya había demostrado su eficiencia a la hora de mejorar la eficiencia y resolución temporal [58]) permitió obtener eficiencias prácticamente del 100 % y resoluciones temporales por debajo de los 100 ps sigma. Como ejemplo, se muestra la sección transversal de las celdas RPCs que forman el muro de tiempo de vuelo de HADES con los materiales que los conforman en la figura 8.2.

Además de la revisión de la evolución histórica, se hace una visión general del campo en el momento actual y las principales líneas de investigación asociadas como, las RPCs de alta tasa, su uso para la construcción de equipos como los PET o su uso como telescopios de muones.

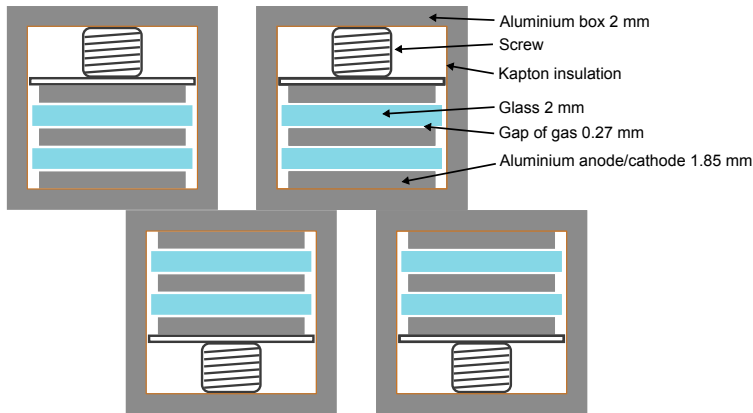


Figura 8.2: Sección transversal de las celdas que conforman el muro de tiempo de vuelo de RPCs de HADES. Están señalados los principales materiales y dimensiones del diseño.

8.3 Capítulo 3

El objetivo de las RPCs de HADES es cubrir la parte de bajo ángulo del espectrómetro para contribuir a la identificación de partículas en eventos de alta multiplicidad. El hecho que este detector fuese introducido en el experimento una vez que éste ya estaba funcionando supuso una fuerte ligadura a la hora de su diseño y construcción. Por las características del experimento, se exigió una eficiencia aproximadamente del 100 % y una resolución temporal por debajo de los 100 ps para que fuese posible la separación entre electrones, piones y kaones por tiempo de vuelo.

Para cumplir con los objetivos se diseñó un detector formado por 6 módulos iguales con geometría trapezoidal para cubrir todos los ángulos. Esta geometría viene dada por la construcción del propio espectrómetro, definida por los anillos superconductores generadores del campo magnético necesario para la medida del momento de las partículas y su identificación. Un esquema de la estructura interior de uno de los planos de RPC se encuentra en la figura 8.3, donde se puede apreciar la división del detector en pequeñas celdas de distinto tamaño.

Una vez descritas las características físicas del detector, se hace una revisión del campo de muros de tiempo de vuelo basados en RPCs. Destacan

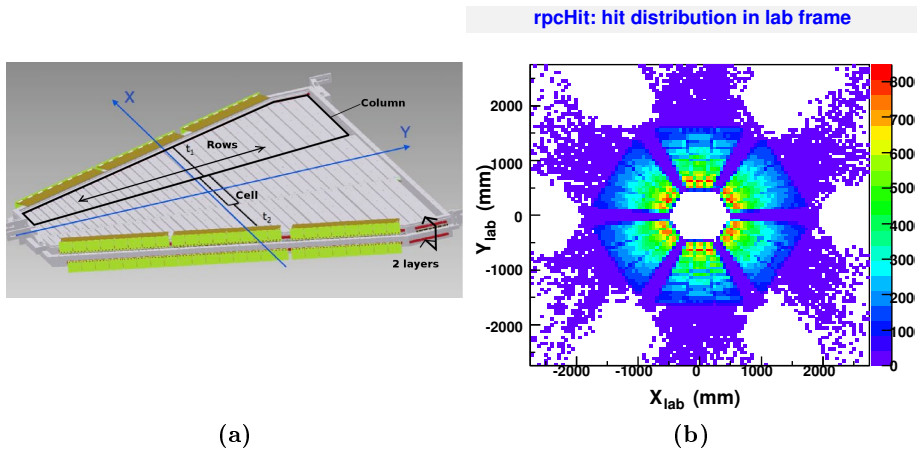


Figura 8.3: a) Estructura interna de un plano de RPC. La distribución en celdas, columnas y filas característica se debe a la necesidad de cumplir con los criterios de eficiencia y aceptación en el experimento. b) Ejemplo de distribución de impacto de partículas producidas con beam de oro.

sobre todo cuatro experimentos: ALICE, FOPI, HARP y STAR.

Finalmente, se introduce un código fenomenológico para la simulación de la respuesta del detector basado en sencillos principios físicos y en los conocimientos en la evolución de las avalanchas en gases. Cabe destacar la exactitud del método para la reproducción de algunos parámetros de la respuesta del detector como la carga, la resolución temporal y la eficiencia. Como ejemplo se presenta aquí una comparación entre un espectro de carga real y otro obtenido mediante la técnica de simulación en la figura

8.4 Capítulo 4

Las datos de colisiones oro sobre oro que tomó HADES en los años 2011 y 2012 requerían de una preparación de los mismos para que fuesen aptos para realizar los análisis experimentales y cumplir así con los propósitos del experimento. Para ello, los algoritmos de calibración existentes fueron mejorados tanto desde el punto de vista de los resultados obtenidos como de la estabilidad de los métodos. La estabilidad era un paso necesario

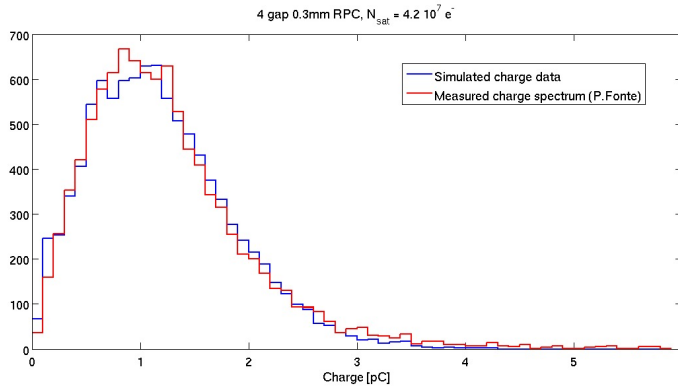


Figura 8.4: Comparación entre un espectro de carga medido y otro simulado para una RPC de 4 planos de 0.3 mm. El espectro medido ha sido tomado de [95]

debido al número de canales a calibrar y que todos los canales deben ser calibrados usando el mismo método para reducir errores.

Como resultado de la calibración se han obtenido resoluciones temporales de 64.3 ps para protones y 71.9 ps para piones. Estas resoluciones cumplen sobradamente el objetivo de una resolución por debajo de los 100 ps necesaria para una correcta separación entre las diferentes especies de partículas presentes en el cóctel.

Además de la calibración y comprobación de los datos, se ha realizado un estudio de la respuesta del detector en función del tipo de partícula incidente (en el cóctel entre otras hay electrones, positrones, piones positivos y negativos, protones, deuterio, tritio y helio), su energía, su ángulo y la dependencia de esos parámetros con la resolución temporal, diferentes parámetros referentes a la carga inducida y la probabilidad de aparición de descargas. Si bien este análisis se realizó para encontrar una dependencia entre la carga inducida medida y parámetros como la eficiencia y la resolución temporal, los resultados sorprendieron con un efecto inesperado: la aparición de una clara dependencia entre la carga inducida con la masa de la partícula, mostrado en la figura 8.5 que abre una nueva puerta a la identificación de partículas mediante la carga depositada por las mismas.

Por último en este capítulo se discute y muestran los resultados de un algoritmo para la recuperación de eventos en los que dos partículas conta-

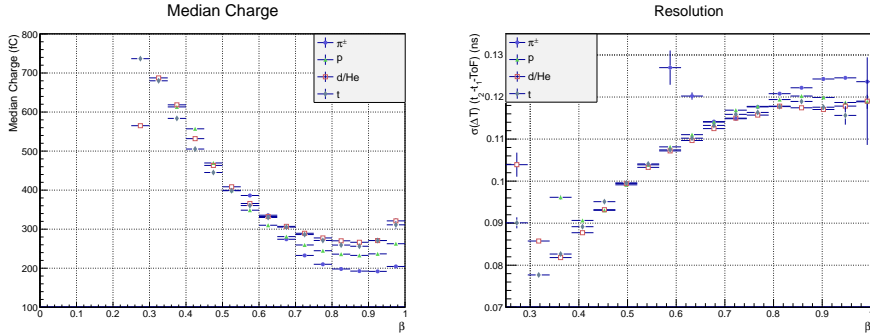


Figura 8.5: La mediana de la carga medida y la resolución temporal en función de β . Nótese la anticorrelación entre ambas medidas. Puesto que la resolución temporal está estrechamente ligada con las fluctuaciones de la señal inducida, a mayor carga (señales más grandes) esta fluctuación disminuye.

minaron la medida de tiempo y posición de una celda. Este método consiste en el empleo de la información proveniente del software de reconstrucción de trazas existente en HADES. El método sólo se empleó para tres hipótesis diferentes: que la partícula sea un electrón, un pión o bien un protón. El número de eventos reconstruidos satisfactoriamente aumentó entre 1 % y 2 % en función del régimen de multiplicidad del evento.

8.5 Capítulo 5

Las posibilidades que ofrecen los detectores de tiempo de vuelo como las RPCs no sólo se restringe al ámbito de una buena medida de los tiempos. Es un hecho que este tipo de detectores, tal como se ha demostrado [65] pueden ofrecer resoluciones espaciales del orden de $50 \mu\text{m}$. Por otro lado, sin llegar a competir en resolución espacial con otros métodos existentes hoy día, enmarcado en el proyecto TRASGO [66], de nuestro grupo, un nuevo método de tracking de partículas cargadas era necesario para aprovechar las posibilidades que nos ofrece una buena medida de tiempos.

Los algoritmos de tracking de partículas tradicionales en caso de combinar la información temporal de los detectores lo hacen en etapas posteriores y normalmente se hace una conversión tiempo-coordenada en la que par-

te de la información se pierde. Para solventar este problema y sacar el máximo rendimiento en tracking que pueden ofrecer detectores de tiempo de vuelo, hemos desarrollado un algoritmo basado en mínimos cuadrados caracterizado por los siguientes principios:

- La trayectoria de una partícula puede describirse unívocamente por un vector llamado saeta (SmAllEst seT of dAta) que incluye toda la información espacial y temporal de la partícula en un plano determinado. El vector está constituido por dos coordenadas, dos pendientes, el tiempo en un plano de referencia determinado y la velocidad de la partícula. Por comodidad y linealidad de las ecuaciones la velocidad es sustituida por la lentitud, siendo esta la inversa de la anterior. De esta forma se consigue introducir las relaciones existentes entre ellos desde el primer momento. Otros procesos y características de la dinámica de las partículas como la pérdida de la energía, el multiple scattering o dependencias geométricas como la condición de vértice pueden ser incluidas comodamente como ligaduras de las ecuaciones.
- El modelo a minimizar para obtener la saeta trabaja directamente sobre los datos proporcionados por los detectores sin la necesidad de hacer las transformaciones a coordenadas espaciales. Permite además incluir los parámetros de calibración directamente en el modelo.
- La formulación matemática está basada en el álgebra matricial, facilitando de esta forma la transición entre el modelo matemático que describe la respuesta de los detectores y su implementación en lenguaje de programación C++ dentro del entorno científico ROOT[30].

El método se aplicó a continuación al caso el experimento HADES para comprobar el funcionamiento del mismo. A destacar resulta el modelo general que describe la respuesta temporal de los detectores de posición (cámaras de deriva multihilos). La reconstrucción de otros parámetros como el momento de las partículas se realizó usando parametrizaciones de resultados del análisis de datos simulados mediante el entorno de generación de eventos PLUTO++[32] y GEANT3[31].

El comportamiento del algoritmo se comprobó con datos simulados y con datos de haz. Los resultados con los datos simulados presentaban resoluciones en momento por debajo del 2%. En el caso de los datos de haz,

la diferencia entre el método empleado en el experimento y el TimTrack fue menor que 6 %.

8.6 Capítulo 6

El detector de tiempo de vuelo antes de ser instalado en su ubicación definitiva fue puesto a punto y probado mediante la incidencia de radiación cósmica. Los datos correspondientes a los ensayos y puesta a punto se tomaron a lo largo del año 2009 y dieron origen a un estudio sobre la capacidad que tienen y ofrecen detectores que usan la tecnología de placas resistivas paralelas en experimentos de rayos cósmicos.

Dado que el montaje consistió en detectores apilados de dos en dos, tomando datos en coincidencias entre ellos, esto nos permitió tras realizar sendas calibraciones y sincronizaciones, acceder a variables como la densidad de partículas, su dispersión temporal de llegada y dirección tal como muestra la figura 8.6.

Los eventos reconstruidos han sido usados para hacer un estudio de las capacidades de los detectores de estas características a la hora de ser empleados en experimentos de rayos cósmicos. Tal como se introdujo en el segundo capítulo de esta tesis, las RPCs encontraron una de sus aplicaciones en este tipo de experimentos, sin embargo aquí se propone un uso que va más allá del conteo de partículas en una superficie para además introducir la reconstrucción de las trazas de las partículas que a su vez permiten medir la dirección de incidencia de una cascada de partículas secundarias producida por un rayo cósmico de alta energía. El método tradicional reconstruye el plano de incidencia a partir de los datos temporales tomados en una gran superficie, aquí mostramos que se pueden obtener valores similares con detectores sustancialmente más pequeños pero que midan con gran precisión la posición y el tiempo de llegada para posibilitar de esta forma la reconstrucción de las trazas y por consiguiente de los frentes.

Además usando modelos conocidos como el de Linsley[117], a partir de estas variables se ha podido estimar el flujo en función de su energía de los rayos cósmicos primarios para energías entre 10^{14} - 10^{18} eV mostrado en la figura 8.7.

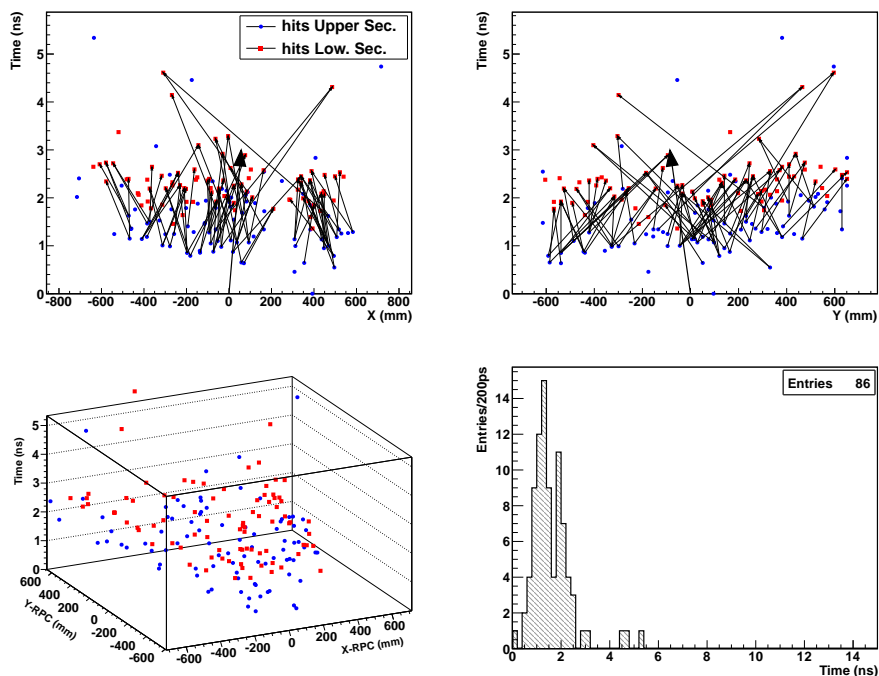


Figura 8.6: Reconstrucción de un evento de alta multiplicidad con dos sectores del muro de tiempo de vuelo de RPCs de HADES. Los vectores representan las trazas de partículas reconstruidas. El vector localizado en el 0 corresponde a la dirección de llegada del frente, obtenido a partir de los vectores de llegada de partículas. Arriba izda.: proyección de los tiempos de llegada en el evento respecto al eje X del detector. Arriba der.: proyección de los tiempos de llegada en el evento respecto al eje Y del detector. Abajo izda. : Vista tridimensional de los tiempos de llegada. Abajo der.: Tiempos de llegada de las partículas corregidas por el ángulo de incidencia de la avalancha.

8.7 Conclusiones

El presente trabajo examina diferentes aspectos relacionados con el muro de tiempo de vuelo basado en detectores de placas resistivas paralelas

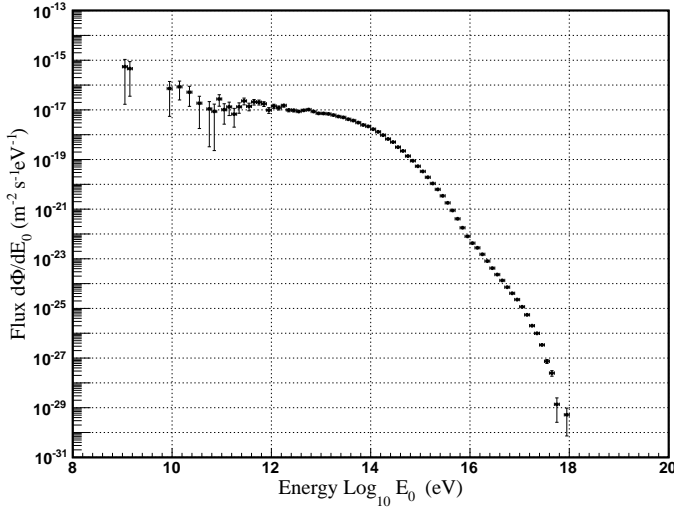


Figura 8.7: Espectro de flujo de energías de cósmicos primarios obtenido a partir del análisis de los datos tomados durante la puesta a punto con radiación cósmica en HADES. Para calcular el flujo se ha usado la parametrización propuesta por J. Linsley[117] y la distribución lateral de densidad de partículas conocida como NKG[42].

(RPCs) construidas para el experimento HADES. En primer lugar se analizó la respuesta del detector en un entorno de colisiones oro-oro con una gran muestra de datos de calidad. Los algoritmos empleados tanto para el análisis como para las calibraciones fueron revisados y actualizados para alcanzar los objetivos de diseño usando el entorno de software de HADES.

El algoritmo de reconstrucción de partículas TimTrack ha sido extendido para tener en cuenta modelos no lineales y la posibilidad de integrar las diferentes ligaduras que puedan presentar los parámetros ajustados. Se ha desarrollado un modelo que se adapta a cualquier geometría de cámaras de deriva multihilos. Además, el algoritmo se ha adaptado al caso del experimento HADES.

Por último, se han analizado los datos de rayos cósmicos tomados con los detectores de RPC durante su puesta a punto antes de la instalación definitiva en el espectrómetro. Puesto que no existía ningún detector externo

que proveyera una señal de comienzo de los eventos, algoritmos específicos para sincronización y calibración de las celdas tuvieron que desarrollarse. Una vez calibrado el detector, analizamos la microestructura de los rayos cósmicos con una resolución y granularidad que mejora previas experiencias de detectores colocados sobre la superficie terrestre. Con ello mostramos como un detector relativamente pequeño pero que es capaz de ofrecer unas prestaciones de resolución temporal y espacial puede medir las tasas de cascadas atmosféricas con la ayuda de las parametrizaciones existentes para altas energías. Más estudios deben de realizarse para extender estas parametrizaciones a energías más bajas. Además, puesto que el detector ofrece la posibilidad de reconstruir la dirección de llegada de los frentes de las cascadas, podría ser una buena alternativa a otras tecnologías de monitorización continua de la radiación cósmica como los detectores de neutrones o los detectores de muones estándar.

Bibliography

- [1] R. Rapp and J. Wambach. Chiral Symmetry Restoration and Dileptons in Relativistic Heavy-Ion Collisions. *Adv. Nucl. Phys.*, 25, 2000.
- [2] HADES Collaboration. The Hight-Acceptance Dielectron Spectrometer HADES. *e-Print: arXiv:0906.0091 [nucl-ex]*, 2009.
- [3] S. Afanasiev, et al. The NA49 large acceptance hadron detector. *Nucl. Instr. and Meth. A*, 430(2–3):210–244, 1999.
- [4] D. Adamová, et al. CERES/NA45 Collaboration. *Nuclear Physics A*, 774:939–, 2006.
- [5] Lee S. Schroeder. Dilepton (e+e-) production at Bevalac energies. *Nuclear Physics A*, 527:625–628, 1991.
- [6] Particle Data Group, pdg.lbl.gov, 2012.
- [7] T. Bretz. Magnetfeldeigenschaften des Spektrometers HADES. Master's thesis, 1999.
- [8] P. Salabura, et al. HADES- A Hight Acceptance DiElectron Spectrometer. *Nucl. Phys. B*, 44:701–707, 1995.
- [9] R. Schicker. Acceptance and resolution simulation studies for the dielectron spectrometer HADES at GSI. *Nucl. Instr. and Meth. A*, 380:586–596, 1996.
- [10] K. Zeitelhack, et al. The HADES RICH detector. *Nucl. Instr. and Meth. A*, 433:201–206, 1999.
- [11] R. Gernhäuser, et al. Photon detector performance and radiator scintillation in the HADES RICH. *Nucl. Instr. and Meth. A*, 371:300–304, 1996.

- [12] C. Agodi, et al. The Time of Flight Wall for the HADES Spectrometer. *IEEE Trans. on Nucl. Scien.*, 45(3):665–669, 1998.
- [13] C. Agodi, et al. The HADES time-of-flight wall. *Nucl. Instr. and Meth. A*, 492:14–25, 2002.
- [14] L. Lopes. Private communications.
- [15] D. Gonzalez-Diaz. *Research and developments on timing RPCs. Application to the ESTRELA detector of the HADES experiment at GSI*. PhD thesis, USC, 2006.
- [16] A. Balanda, et al. The HADES Pre-Shower detector. *Nucl. Instr. and Meth. A*, 531:445–459, 2004.
- [17] W. Czyzycki, et al. Electromagnetic Calorimeter for HADES. 2011. arXiv:1109.5550v2 [nucl-ex].
- [18] W. Koenig J. Pietraszko. Beam detectors in Au+Au run. Talk in the HADES Collaboration Meeting XXIV, Crakow, Poland., 2012.
- [19] J. Pietraszko, L. Fabietti, W. Koenig, M. Weber. Diamonds as timing detectors for minimum-ionizing particles: The HADES proton-beam monitor and START signal detectors for time of flight measurements. *Nucl. Instr. and Meth. A*, 618:121–123, 2010.
- [20] B. Kindler, B. Lommel, A. Hübner, W. Hartmann, J. Steiner. Targets for electron-positron pair spectrometer HADES. *Nucl. Instr. and Meth. A*, 655:95–99, 2011.
- [21] I. Fröhlich, et al. A General Purpose Trigger and Readout Board for HADES and FAIR-Experiments. *IEEE Trans. on Nucl. Scien.*, 55(1):59–66, 2008.
- [22] M. Palka, et al. The New Data Acquisition System for the HADES Experiment. *Proc. IEEE Nucl. Sci. Symp.*, pages 1398–1404, 2008.
- [23] J. Michel, et al. The HADES DAQ System: Trigger and Readout Board Network. *IEEE Trans. on Nucl. Scien.*, 58(4):1745–1750, 2011.

- [24] M. Traxler, et al. 128 channel high resolution TDC with integrated DAQ-system. *GSI Scientific Rep. 2005-1*, 2005.
- [25] M. Traxler, et al. A general purpose trigger and readout board for HADES and FAIR-experiments. *GSI Scientific Rep. 2007-1*, 2006.
- [26] M. Traxler, et al. A compact system for high precision time measurements (< 14 ps RMS) and integrated data acquisition for a large number of channels. *J. Instr.*, 2011.
- [27] A. Tarantola Piloni. *Dielectron analysis in p-p collisions at 3.5 GeV with the HADES spectrometer: ω -meson line shape and a new electronics readout for the Multi-wire Drift Chambers*. PhD thesis, Johann Wolfgang Goethe-Universität in Frankfurt am Main, 2010.
- [28] A. Tarantola, et al. The Upgrade of the Multiwire Drift Chamber Readout of the HADES Experiment at GSI. *IEEE Nucl. Scien. Symp. Conf. Rec.*, 100(N30):2146–2149, 2008.
- [29] M. Palka. *ϕ Meson Production in pp Reaction at 3.5 GeV with HADES Detector*. PhD thesis, Jagiellonian University, Cracow, 2011.
- [30] R. Brun and F. Rademakers. ROOT, an object-oriented data analysis framework. *Nucl. Instr. and Meth. A*, 389:81, 1997.
- [31] GEANT Detector Description and Simulation Tool. CERN Program Library Long Writeup W5013, 1993.
- [32] I. Fröhlich, et al. Pluto: A Monte Carlo Simulation Tool for Hadronic Physics. *PoS (ACAT)*, (076), 2007.
- [33] ROOT website. root.cern.ch.
- [34] M. Sánchez García. *Momentum Reconstruction and Pion Production Analysis in the HADES Spectrometer at GSI*. PhD thesis, USC, 2003.
- [35] T. Galatyuk. Private communications.
- [36] G.N. Agakichiev et al. Fast Method for Searching for Tracks in Multilayer Drift Chambers of HADES Spectrometer. *Particles and Nuclei, Letters*, 101(4):55–68, 2000.

- [37] A.Ierusalimov. New version of Dubna Track Fitter. HADES internal report, 2002.
- [38] A. Rustamov. An algorithm for momentum reconstruction for the hades experiment. HADES Internal Report, 2003.
- [39] A. Sadovsky. *Investigation of K^+ meson production in $C+C$ collisions at $2A$ GeV with HADES*. PhD thesis, Institut für Kern- und Teilchenphysik, Technische Universität Dresden, 2007.
- [40] E. Krebs and J. Markert. Application of a Kalman and Deterministic Annealing Filter in HADES. *GSI Report 2011*, 2011.
- [41] Glenn F. Knoll. *Radiation detection and measurement*. John Wiley & Sons, 2 edition, 1989.
- [42] J. Beringer et al. (PDG). Passage of particles through matter. *PR*, D86(010001), 2012. <http://pdg.lbl.org>.
- [43] <http://pdg.lbl.gov/AtomicNuclearProperties/>.
- [44] Y.S. Tsai. Pair production and bremsstrahlung of charged leptons. *Rev. Mod. Phys.*, 46:815, 1974.
- [45] H. Bichsel. A method to improve track and particle identification in TPCs and silicon detectors. *Nucl. Instr. and Meth. A*, 562:154–197, 2006.
- [46] C. D. Anderson. The Positive Electron. *Physical Review*, 43:491, 1933.
- [47] G. Charpak, R. Bouclier, T.Bressani, J. Favier and Č. Zuačič. The use of multiwire proportional counters to select and localize charged particles. *Nucl. Instr. and Meth.*, 62:262–268, 1968.
- [48] J. S. Townsend. *The theory of Ionization of Gases by Collision*. Constable & Company LTD, London, 1910.
- [49] A.J. Davies and C.J. Evans. The theory of ionization growth in gases under pulsed and static fields, 1973. CERN 73-10.

-
- [50] C. Lippmann and W. Riegler. Space charge effects in Resistive Plate Chambers. *Nucl. Instr. and Meth. A*, 517:54–76, 2004.
- [51] A. Blanco. *A Small animal pet prototype with sub-millimetre spatial resolution based on tRPCs*. PhD thesis, USC, 2011.
- [52] J. Markert. *Untersuchung zum Ansprechverhalten der Vieldraht-Driftkammern niedriger Massenbelegung des HADES Experimentes*. PhD thesis, Johann Wolfgang Goethe-Universität, Frankfurt am Main, 2005.
- [53] S. Ramo. Currents Induced by Electron Motion. *Proceedings of the I.R.E.*, 1939.
- [54] М.И. Дайон и Г.А. Лексин. Искровые детекторы заряженных частиц. *Успехи физических наук*, 2, 1963.
- [55] V.V. Parkhomchuck, Y. N. Pestov and N.V. Petrovikh. A spark counter with large area. *Nucl. Instr. and Meth.*, 93:269–270, 1971.
- [56] Yu. N. Pestov, H.R. Schmidt, B. Schreiber. Timing performance of spark counters and photon feedback. *Nucl. Instr. and Meth. A*, 456:11–15, 2000.
- [57] R. Santonico and R. Cardarelli. Development of resistive plate counters. *Nucl. Instr. and Meth.*, 187:377–380, 1981.
- [58] E. Cerron Zeballos et al. A new type of resistive plate chamber: The multigap RPC. *Nucl. Instr. and Meth. A*, 374:132–135, 1996.
- [59] E. Cerron Zeballos et al., A comparison of the wide gap and narrow gap resistive plate chamber. *Nucl. Instr. and Meth. A*, 373:35–42, 1996.
- [60] P. Fonte, A.S. Smirnitski and M.C.S. Williams. A new high-resolution TOF technology. *Nucl. Instr. and Meth. A*, 443:201–204, 2000.
- [61] P. Camarri, R. Cardarelli, A. Di Ciaccio and R. Santonico. Streamer suppression with SF₆ in RPCs operated in avalanche mode. *Nucl. Instr. and Meth. A*, 414:317–324, 1998.

- [62] S. An et al. A 20ps timing device- A Multigap Resistive Plate Chamber with 24 gas gaps. *Nucl. Instr. and Meth. A*, 594:39–43, 2008.
- [63] V. Ammosov. TESLA digital hadron calorimeter (requirements, status and plans for R&D). *Nucl. Instr. and Meth. A*, 494:355–361, 2002.
- [64] J. Repond. A digital hadron calorimeter with Resistive Plate Chambers. *Nucl. Instr. and Meth. A*, 533:126–129, 2004.
- [65] A. Blanco, et al. TOFtracker: combination of time-of-flight and high-accuracy bidimensional tracking in a single gaseous detector. Talk in RPC2012, XI Workshop on Resistive Plate Chambers and Related Detectors, Frascati, 2012.
- [66] D. Belver, et al. TRASGO: A proposal for a timing RPCs based detector for analyzing cosmic ray air showers. *Nucl. Instr. and Meth. A*, 661:s163–s167, 2012.
- [67] J. A. Garzón and P. Cabaelas. TimTrack: A matrix formalism for a fast time and track reconstruction with timing detectors. *Nucl. Instr. and Meth. A*, 661:s210–s213, 2012.
- [68] M. Morales et al. Conductivity and charge depletion aging of resistive electrodes for high rate RPCs. To be published in RPC2012 proceedings, 2012.
- [69] D. Belver. *The Front-End Electronics of the HADES timing RPCs wall: design, development and performances analysis*. PhD thesis, USC, 2009.
- [70] A. Gil. *Electronic developments for the HADES RPC Wall*. PhD thesis, Universidad de Valencia, 2010.
- [71] P. Cabanelas. *Software development and Performance Analysis of the HADES Resistive Plate Chamber Time-of-Flight Detector at GSI*. PhD thesis, USC, 2011.
- [72] A. Blanco, et al. A large area timing RPC. *Nucl. Instr. and Meth. A*, 485:328–342, 2002.

-
- [73] D. Belver, et al. The HADES RPC inner TOF wall. *Nucl. Instr. and Meth. A*, 602:687–690, 2009.
- [74] Ch. Finck, P. Fonte and A. Gobbi. Results concerning understanding and applications of timing GRPC. *Nucl. Instr. and Meth. A*, 508:63–69, 2003.
- [75] H. Alvarez Pol, et al. A large area timing RPC prototype for ion collisions in the HADES spectrometer. *Nucl. Instr. and Meth. A*, 535:277–282, 2004.
- [76] W. Riegler, C. Lippmann and R. Veenhof. Detector physics and simulation of resistive plate chambers. *Nucl. Instr. and Meth. A*, 500:144–162, 2003.
- [77] The LHC Study Group. The Large Hadron Collider Conceptual Design. CERN/AC/95-05 (LHC), 1995.
- [78] A. Akindinov, et al. A study of the multigap RPC at the gamma irradiation facility at CERN. *Nucl. Instr. and Meth. A*, 490:58–70, 2002.
- [79] A. Akindinov, et al. The MRPC detector for the ALICE Time Of Flight System: Final Design and Performances. *Nucl. Phys. B*, 158:60–65, 2006.
- [80] A. Alici For the ALICE Collaboration. The MRPC-based ALICE time of flight detector: Status and performance. *Nucl. Instr. and Meth. A*, 2012. In Press, Corrected Proof.
- [81] A. Akindinov, et al.,. The MRPC-based ALICE Time-Of-Flight detector: Commissioning and first performance. *Nucl. Instr. and Meth. A*, 661:s98–s101, 2012.
- [82] A. Schüttauf. Timing RPCs in FOPI. *Nucl. Instr. and Meth. A*, 533:65–68, 2004.
- [83] www.gsi.de.
- [84] A. Schüttauf, et al. Performance of the Multistrip-MRPCs for FOPI. *Nucl. Phys. B*, 158:52–55, 2006. Proc. Suppl.

- [85] M. Kiš, et al. A Multi-strip Multi-gap RPC Barrel for Time-of-Flight Measurements. *Nucl. Instr. and Meth. A*, 646:27–34, 2001.
- [86] V. Ammosov, et al. The HARP resistive plate chambers: Characteristics and physics performance. *Nucl. Instr. and Meth. A*, 602:639–643, 2009.
- [87] M. Bogomilov, et al. The HARP RPC time-of-flight system. *Nucl. Instr. and Meth. A*, 508:152–158, 2003.
- [88] B Bonner, et al. A multigap resistive plate chamber prototype for time-of-flight for the STAR experiment at RHIC. *Nucl. Instr. and Meth. A*, 478:176–179, 2002.
- [89] W.J. Llope for the STAR Collaboration. Multigap RPCs in the STAR experiment at RHIC. *Nucl. Instr. and Meth. A*, 661:s110–s113, 2012.
- [90] G. Kornakov. A General Purpose RPC simulator/digitizer. Internal HADES report, 2009.
- [91] W. Riegler and C. Lippmann. The physics of Resistive Plate Chambers. *Nucl. Instr. and Meth. A*, 518:86–90, 2004.
- [92] J. de Urquijo, A.M. Juárez, E. Basurto and J.L. Hernández-Ávila. Electron swarm coefficients in 1,1,1,2 tetrafluoroethane (R134a) and its mixtures with Ar. *Eur. Phys. J. D*, 51:241–246, 2009.
- [93] E. Basurto, J.L. Hernández-Ávila, A.M. Juárez and J. de Urquijo. Time-resolved measurement of electron swarm coefficients in tetrafluoroethane (R134a). *28th ICPIG, Prague*, page 157, 2007.
- [94] J. de Urquijo, E. Basurto and J.L. Hernández-Ávila. Effective ionization, electron and ion transport in SF₆-He mixtures. *J. Phys. D*, 34:2151–2159, 2001.
- [95] P. Fonte et al. High-resolution RPCs for large TOF systems. *Nucl. Instr. and Meth. A*, 449:295–301, 2000.
- [96] M. Abbrescia, et al. Resistive Plate Chambers in avalanche mode: a comparison between model predictions and experiment results. *Nucl. Instr. and Meth. A*, 409:1–5, 1998.

-
- [97] H. Raether. *Electron avalanches and breakdown in gases*. Butterworths, 1964.
- [98] D. Gonzalez-Diaz. Simulation of resistive plate chambers with multi-strip readout. *Nucl. Instr. and Meth. A*, 661:s172–s176, 2012.
- [99] A. Blanco, et al. In-beam measurements of the hades-tof rpc wall. *Nucl. Instr. and Meth. A*, 602:691–695, 2009.
- [100] D. Belver, et al. Performance of front-end electronics for the hades rpc tof wall on a 12c beam. *Nucl. Instr. and Meth. A*, 602:788–791, 2009.
- [101] A. Blanco, et al. Rpc hades-tof wall cosmic ray test performance. *Nucl. Instr. and Meth. A*, 661:S114–S117, 2012.
- [102] P. Cabanelas et al. Performances of 4-gap timing rpcs for relativistic ions in the range $z = 1-6$. *JINST (Journal of Instrumentation)*, 4-P11007, 2009.
- [103] D. Belver, et al. Performance of the low-jitter high-gain/bandwidth front-end electronics of the hades trpc wall. *IEEE Transactions on nuclear science*, 57(5):2848–2856, 2010.
- [104] V. Pechenov. Private communications.
- [105] A. Blanco, et al. Performance of the HADES-TOF RPC wall in a Au-Au beam. *Proc. of Science*, 2012. XI workshop on Resistive Plate Chambers and Related Detectors - RPC2012.
- [106] ROOT TMatrix performance: <ftp://root.cern.ch/root/doc/14LinearAlgebra.pdf>.
- [107] M. Ambrosio, et al. Interpretation of the time structure of the EAS disc measured by the GREX/COVER_PLASTEX experiment. *Astroparticle Physics*, 7:329–341, 1997.
- [108] G. Marsella, et al. Physics and astronomy results with the ARGO-YBJ experiment. *Nucl. Phys. B - Proc. Supp.*, 188:280–282, 2009.

- [109] J. Blümer, R. Engel and J.R. Hörndel. Cosmic rays from the knee to the highest energies. *Progress in Particle and Nuclear Physics*, 63:293–338, 2009.
- [110] Forbush, S. E. On the Effects in Cosmic-Ray Intensity Observed During the Recent Magnetic Storm. *Phys. Rev.*, 51:1108–1109, Jun 1937.
- [111] A. Duperier. The Seasonal Variations of Cosmic-Ray Intensity and Temperature of the Atmosphere. *Proc. R. Sco. Lond. A*, 177:204–216, 1941.
- [112] M. Ambrosio, et al. Seasonal variations in the underground muon intensity as seen by MACRO. *Astrop. Phys.*, 7:109–124, 1997.
- [113] S. Osprey, et al. Sudden stratospheric warmings seen in MINOS deep underground muon data. *Geoph. Res. Lett.*, 36, 2009.
- [114] A.N. Dmitrieva, et al. Corrections for temperature effect for ground based muon hodoscopes. *Astrop. Phys.*, 34:401–411, 2011.
- [115] M.P. Baldwin, et al. How will the stratosphere affect climate change? *Science*, 316:1576–1577, 2007.
- [116] J. Álvarez Muñiz. Private communications.
- [117] J. Linsley. Mini and super mini arrays for the study of highest energy cosmic rays. *19th Intern. Cosmic Ray Conf., La Jolla*, pages 434–437, 1985.
- [118] A. M. Hillas. Some recent development in cosmic rays. *Phys. Rep. C*, 20:79, 1975.
- [119] S.J. Sciutto. The AIRES system for air shower simulations. An update. *arXiv:astro-ph/0106044*, 2001.
- [120] D. Belver, et al. Analysis of the space-time microstructure of cosmic ray air showers using the HADES RPC TOF wall. *J. Instr.*, 2012. Accepted, to be published.

-
- [121] W.D. Apel et al. Time structure of the EAS electron and muon components measured by the KASCADE-Grande experiment. *Astropart. Phys.*, 29:317–330, 2008.
- [122] G. Agnetta et al. Time structure of the extensive air shower front. *Astropart. Phys.*, 6:301–312, 1997.
- [123] C.R.A. Augusto, et al. Simultaneous observation at sea level and at 5200 m.a.s.l. of high energy particles in the South Atlantic Anomaly. *Astroparticle Physics*, 34:40–47, 2010.
- [124] The Pierre Auger collaboration collaboration. The Pierre Auger Observatory scaler mode for the study of solar activity modulation of galactic cosmic rays. *Journal of Instrumentation*, 6(01):P01003, 2011.
- [125] M. Teshima et al. Properties of 10^9 - 10^{10} GeV extensive air showers at core distances between 100 and 3000 m. *J. Phys. G: Nucl. Part. Phys.*, 12:1097, 1986.
- [126] W.E. Hazen, H.Y. Dai and E.S. Hazen. Study of a mini-array for the Linsley effect in cosmic-ray air showers. *J. Phys. G: Nucl. Part. Phys.*, 15:113, 1989.
- [127] T. Bezboruah, K.Boruah, P.K. Boruah. A non conventional method of UHE cosmic ray detection. *Astropart. Phys.*, 11:395–402, 1999.
- [128] U.D. Goswami, K.Boruah and P.K. Boruah. New results from Gauhati University miniarray detector. *29th. Intern. Cosmic Ray Conf., Pune*, optional:159–162, 2005.
- [129] H. Matsumoto et al. Simulation studies and implementation of Linsley’s EAS time structure method for the primary cosmic ray spectrum. *Nucl. Instr. and Meth. A*, 614:475–482, 2010.
- [130] A. Iyono et al. Linsley’s EAS time structure method for the primary cosmic ray spectrum at LAAS. *Astrophys. Space Sci. Trans.*, 7:335, 2011.

- [131] I.I. Yashin et al. Investigation of primary cosmic ray spectrum shape by means of EAS muon density technique. *European Cosmic Ray Symposium, Kosice*, 2008.